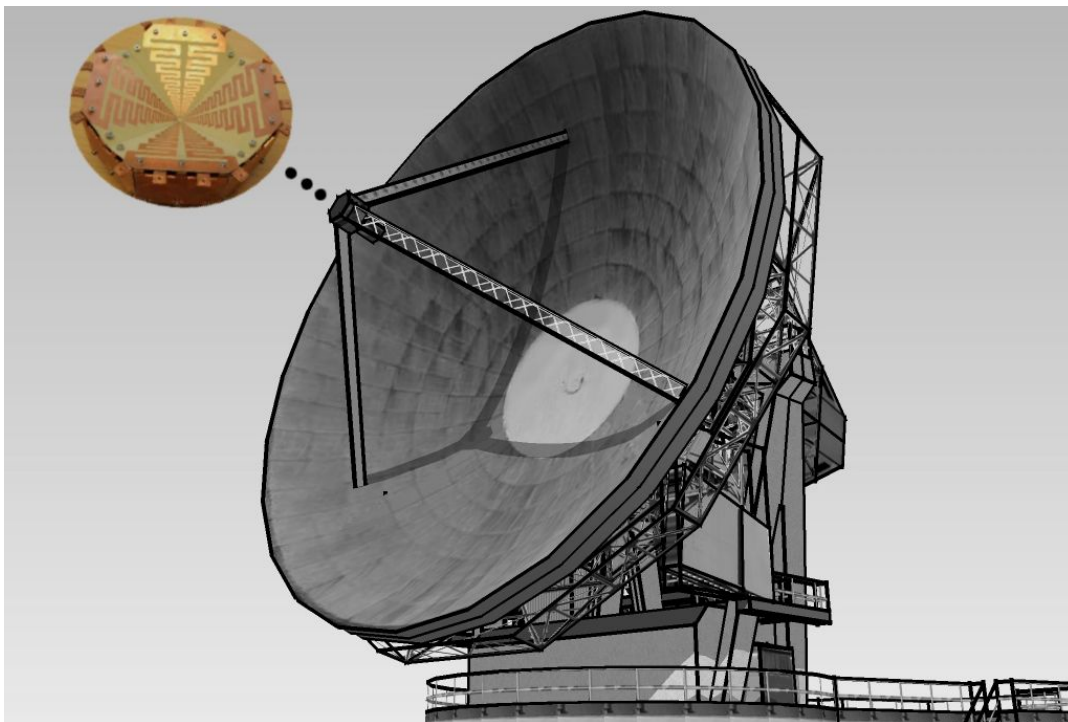


CHALMERS



Studies of the Eleven Antenna Feed in Axi-Symmetric Reflector Systems For the Next Generation Radio Telescope

Master of Science Thesis

WAN-CHUN LIAO

Department of Signals and Systems
Division of Signal Processing and Antennas
CHALMERS UNIVERSITY OF TECHNOLOGY
Gothenburg, Sweden, 2012

Studies of the Eleven Antenna Feed in
Axi-Symmetric Reflector Systems
For the Next Generation Radio Telescopes

WAN-CHUN LIAO

Department of Signals and Systems
CHALMERS UNIVERSITY OF TECHNOLOGY
Göteborg, Sweden 2012

Studies of the Eleven Antenna Feed in Axi-Symmetric Reflector Systems
For the Next Generation Radio Telescopes
WAN-CHUN LIAO

© WAN-CHUN LIAO, 2012

Department of Signals and Systems
Chalmers University of Technology
SE-412 96 Göteborg
Sweden
Tel. +46-(0)31 772 1000

Main supervisor: Dr. Marianna V. Ivashina
Co-supervisor: Oleg Iupikov
Examiner: Prof. Per-Simon Kildal

Cover: Axi-symmetric prime-focus reflector antenna system with the Eleven feed.

Printed by Reproservice
Göteborg, Sweden 2012

Always desire to learn something useful.

-Sophocles

Abstract

The international radio astronomy community is currently pursuing the development of a giant radio telescope known as the Square Kilometre Array (SKA). The SKA will consist of several antenna technologies, including reflector antennas fed with novel multi-beam Phased Array Feeds (PAFs) and/or Single Pixel Feeds (SPFs) that can operate approximately at frequencies from 1 to 10 GHz. The baseline of the SKA represents an array of several hundred to a few thousand reflector antennas of 15-m diameter that will realize sensitivity of $10,000 \text{ m}^2/\text{K}$. During the past years, different reflector and feed concepts have been proposed and examined, but only a small number of these design options (that have a sufficient level of maturity) will be built and tested during the SKA design verification phase. These tests are aimed to evaluate the overall system performance as well as construction and operational costs. The final choices of the dish and feeds used in the evaluation tests might include: (i) off-set Gregorian and axi-symmetric reflector antennas and; (ii) a collection of octave bandwidth horns or/and single-pixel wideband feeds, such as quad-ridged horn and the Eleven antenna. The aim of this work is to investigate the performance of the wideband Eleven antenna feed in combination with the axi-symmetric reflector antenna.

Keywords: the Eleven antenna feed, axi-symmetric reflector antenna, offset Gregorian reflector antenna system, strut and feed blockage effects, receiving sensitivity, spillover noise temperature.

Acknowledgements

Many people deserve my thanks for their help in completing this project and I can not accomplish it without their help and support. I would like to thank Onsala Space Observatory of the department of Earth and Space Science at Chalmers (in particularly Dr. Miroslav Pantaleev) for supporting this work.

Particularly, Dr. Jian Yang of Antenna Group at Chalmers provided the measured data of the Eleven feed, and Prof. Arnold van Ardenne from the department of Earth and Space Sciences at Chalmers made useful suggestions and contributions to my EuCAP conference paper that was written during this project .

I also would like to make a special acknowledgement to Oleg Iupikov for his invaluable help in computing the simulation data in Matlab and relevant research data. I am heartily grateful to my supervisor, Dr. Marianna Ivashina, whose encouragement, support, and supervision from the preliminary to the concluding level enabled me to develop an understanding of the subject; this thesis could not have been written without her. In addition, I would like to thank Prof. Per-Simon Kildal for examining this work.

Lastly, I offer my regards and blessings to all of those who supported me in any respect during the completion of the project. All acknowledgments give thanks and lives a positive vibe on the person being appreciated.

Wan-Chun Liao
Göteborg, Sweden

Contents

List of Acronyms	vii
1. Introduction	1
1.1. Aim and Outline of the Thesis	4
2. Parameters and Performance Figures of Merit of Radio Telescopes	5
2.1. Parameters of Reflector Antennas	5
2.1.1. Axi-Symmetric Prime-Focus Reflector Antennas	5
2.1.2. Offset Gregorian Dual Reflector Antennas	7
2.2. Performance Figures of Merit of Radio Telescopes	8
2.2.1. Aperture Effective Area	8
2.2.2. System Noise Temperature and Sensitivity	9
3. An Overview of the UWB Feed Developments for the SKA	11
3.1. The Allen Telescope Array Feed	12
3.2. The Lindgren Feed	13
3.3. The Non-Planar Quasi-Self-Complementary Feed	14
3.4. The Quad-Ridged Flared Horn	15
3.5. The Eleven Antenna Feed	16
3.6. Comparison of the Feeds	17
4. Methodology for the Analysis of Reflector Antennas	19
4.1. Numerical Methods	19
4.1.1. Physical Optics	19
4.1.2. Physical Theory of Diffraction	20
4.2. Models and Simulation Specifications of the Software Package GRASP	20
4.2.1. Reflector Antenna Models	21
4.2.2. Feed Models	21

4.2.3.	Strut Models	22
4.2.4.	Format of Input/Output Field Data	23
4.2.5.	Convergence of the Physical Optics Integral	23
4.3.	Antenna Aperture Efficiency Calculation Methods	24
4.3.1.	Description of the methods	24
4.3.2.	Numerical Comparison of the Methods	25
5.	Analysis of the Reflector Antenna Performance for Various F/D Ratios	29
5.1.	The Prime-Focus Reflector System with the Eleven Feed	29
5.1.1.	Far-Field Patterns	30
5.1.2.	The Half Power Beam Width and Polarization	30
5.1.3.	Aperture Efficiency and Side Lobe Level	35
5.1.4.	System Noise Temperature and Sensitivity	36
5.1.5.	Temporal Beam Stability	39
6.	Analysis of the Reflector Antenna System Including Strut and Feed Blockage Effects	43
6.1.	The Modeling Procedure and Simulation Methods of the Blockage Effects in GRASP	44
6.1.1.	Strut Blockage	46
6.1.2.	Central Blockage Effects due to the Feed	47
6.2.	Discretization of the Reflector Antenna Far-Field Pattern	49
6.3.	Determination of the Optimal Placement of Struts	54
6.3.1.	The Eleven Antenna Feed	54
6.3.2.	The Horn Feed	57
6.3.3.	Comparison between the Eleven Antenna and Horn Feeds	60
7.	Conclusions	69
	Appendices	73
	A. Matlab Code—Simpson’s Rule for Calculating of the Aperture Efficiency	73
	B. Command List in GRASP 9 for the Analysis of Reflector Antennas	75
	C. Additional Figures	77
	References	85

List of Acronyms

ALMA	The Atacama Large Millimeter/sub-millimeter Array
ATA	The Allen Telescope Array
BOR	Body of Revolution
CO	Co-Polarization
CST	Computer Simulation Technology
FOM	Figure of Merit
FOV	The Field of View
GAVRT	The Glodstone Apple Valley Radio Telescope
GO	Geometrical Optics
GRASP	Generalized Reflector Antenna farm analysis Software Package of TICRA
GTD	Geometrical Theory of Diffraction
HPBW	Half Power Beam Width
LNA	The Low Noise Amplifier
LP	Log-Periodic
Matlab	Matrix Laboratory, a numerical computing environment and fourth-generation programming language
MMIC	Monolithic Microwave Integrated Circuit

MoM	The Method of Moments
PO	Physical Optics
PTD	Physical Theory of Diffraction
QRFH	The Quad-Ridged Flared Horn
QSC	Quasi Self-Complementary
SKA	The Square Kilometre Array
SLL	Side Lobe Level
SWR	Standing Wave Ratio
TICRA	Name derived from Electromagnetic Radiation, a company in Copenhagen, Denmark specializing in antenna analysis and synthesis software
UWB	Ultra-WideBand
XP	Cross-Polarization
XPL	Cross-Polarization Level

Introduction

A brief introduction of the new technology developments for the next generation radio telescope — the Square Kilometre Array (SKA) is presented: The SKA will become a revolutionary instrument with an effective collecting area more than thirty times greater than the largest telescope ever built. The goal and outline of the thesis are described.

Radio astronomy of the 20th century has led to numerous discoveries about the universe and produced six Nobel Prize winners in physics [2]. The focus of interest of these discoveries have been innovated by the antenna and radio frequency technologies driving the observational frontiers of sensitivity and spatial resolution. One of the innovations is radio interferometry (Nobel Prize in 1974), the purpose of which is to achieve high-resolution observations using a cost-effective array of comparatively small telescopes rather than a single very expensive monolithic telescope. This is the current-state-of-art technology that has been realized with many radio telescopes, for example, the Westerbork Synthesis Radio Telescope (WSRT), which constitutes fourteen 25-meter diameter dish antennas [3]. Other enabling technology developments include high efficiency feeds for reflector antennas such as corrugated horns, low-noise (cooled) receiver, synthesis array image formation algorithms, stable clocks and recording systems for the Very Long Baseline Interferometry (VLBI) network.

The new generation radio telescope known as the Square Kilometre Array (SKA) will become operational by 2020 and carry on this innovating tradition [4]. The SKA will be a revolutionary instrument with an effective collecting area more than thirty times greater than the largest telescope ever built. It will operate from 300 MHz to 30 GHz and have a very large field-of-view

(FOV) coverage with a diameter of almost 20 degrees at low frequencies below 1 GHz and a diameter of more than 1 degree (about five full moons) at high frequencies. To realize these immense performance requirements at reasonable cost, the SKA will combine several novel RF antenna technologies and array beamforming techniques. The SKA reference design is based on three systems: (i) Single-Pixel Wide Band Feeds (SPWBFs) of reflector antennas* with enhanced mechanical beam-steering (at high frequencies), (ii) planar Aperture Phased-Arrays (AAs) with electronic (digital) beam-steering (at low frequencies) and (iii) Phased Array Feeds (PAFs)[†] of reflector antennas with both electronic and mechanical beam-steering capabilities at the intermediate frequencies (somewhere in the region of 750 MHz to 2 GHz). Combining the signals from all the antennas will create a telescope with a collecting area equivalent to a single dish with an area of about one square kilometer.

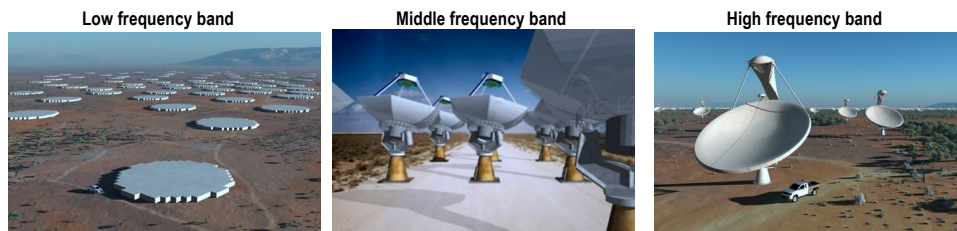


Figure 1.1.: An artist's impression of the SKA reference design consisting of the three novel antenna array technologies: aperture arrays (*left*); dishes with multi-pixel phased array feeds (*middle*); and dishes with single pixel feeds (*right*).

In order to meet the requirements for high sensitivity over a wide FOV coverage, a large amount of relatively small reflector antennas is needed. The trade-off between the minimal cost and the maximum survey speed, proportional to the sensitivity squared, the bandwidth, and the size of FOV [5], turned out to choose the dishes with 15-meter diameter. Approximately 1,200 dishes of 15-meter diameter are needed in combination with extremely low system noise receivers (with T_{sys} of about 35 K) in order to reach the required $A_{\text{eff}}/T_{\text{sys}}$ and imaging performance.

The SKA engineering team considers two options for the type of reflector antennas: the prime-focus axi-symmetric and offset Gregorian configurations. The comparison strategy can be generally grouped into two categories: scientific and financial. The scientific requirements for these systems are stringent and include low noise of the receivers, high efficiency of the antenna and feed, very low wide angle side lobes, accurate and stable mechanical pointing of the dishes, all at an affordable costs of the total system. Higher individual antenna performance can justify higher per antenna cost by reducing the total number of antennas in the array. Fewer anten-

*Reflector antennas are also named as dish antennas in the SKA community.

[†]Focal Plane Arrays (FPA) are also named as Phased Array Feeds.

nas reduce the cost of signal transport, computing, maintenance, and power consumption. The mechanical design of large prime-focus reflector systems is cost-effective, but the aperture efficiency has a theoretical limit (70–75% for the reflectors with F/D^\ddagger about 0.3–0.5), and the side lobe levels are relatively high. Another problem with the axi-symmetric reflector antenna is the deterioration effect of the feed blockage caused by the feed supporting structure. Also, the feed-reflector interaction results in standing waves, reducing the efficiency at some frequencies. On the contrary, the offset configuration usually does not have feed-blockage problem and allow reducing the standing wave effects significantly. Combined with low illumination at the edges of the two reflectors, this can lead to very low levels of the side lobes away from the main beam and its first few side lobes [6]. Furthermore, with offset dual reflector systems one can achieve higher antenna efficiency (since the equivalent F/D of these systems is larger). Nevertheless, the antenna design will be much more complicated, and the operational manufacturing costs are higher.

Another argument is that the offset Gregorian configuration will give rise to lower spillover loss toward the ground and hence reduce thermal noise pickup. The initial comparative analysis of the Gregorian systems with respect to the conventional prime-focus reflector antennas (that has been performed with the Gaussian beam feed models) has demonstrated that the expected increase of the antenna efficiency is about 10% and the reduction of the ground noise contribution is of factor two (from 20 K to 10 K for the elevation angle close to 90°). However, at lower elevation angles this improvement does not seem to be valid. Actually, relative increase of T_{sp} with respect to $El = 90^\circ$ can be up to 15 K (corresponding to $T_{sp} = 25$ K.) For axi-symmetric reflector systems, T_{sp} is highest at $El = 90^\circ$. As a result the sensitivity performance over the elevation angle range is comparable to that of the presently considered (and likely more expensive) offset Gregorian antenna designs [7].

From financial aspect, there is also no clear consensus yet in the SKA community as the resultant cost strongly depends on the technology used for manufacturing the dishes and realization of their mechanical steering mechanisms[§]. The comparative study of reflector antenna systems that has been done in the U.S. led to the surprising conclusion that there is no a large cost difference between the prime-focus and the offset configurations. These studies argue that (i) the SKA antenna will most likely be single-piece reflectors so once the required molds are made there is essentially no premium for asymmetric reflectors and (ii) given the modest increment in cost and a significant improvement in performance, the total system cost might be less with the offset antennas even though their unit cost is higher [9].

[‡] F/D is the reflector parameter, the focal length to diameter ratio, to characterize the shape of the reflector antenna, corresponding to the illumination angle of the reflector (see Chapter 2).

[§]These mechanisms determine the antenna pointing error, which in turn sets the limit on the imaging dynamic range of radio telescopes [8].

In contrast to these studies, the cost estimates made by the industrial companies in Europe such as *Airborne composites*, which has experience in designing large dish systems (e.g. ALMA), demonstrate that the costs for the axi-symmetric dishes made from composite materials will be at least 30–40% lower than that of the offset Gregorian antenna and its supporting structure [10].

The long-term goal of this study is to facilitate a detailed comparative analysis of the axial symmetric and offset reflector antennas with a more realistic choice of the antenna feed, and to demonstrate the pros and cons of each design option based on several performance merits including the system sensitivity and imaging dynamic range.

1.1. Aim and Outline of the Thesis

This aim of this thesis is to perform a comprehensive study of the performance of the Eleven antenna feed combined with axi-symmetric reflector systems for the next generation radio telescopes — the SKA. Chapter 2 describes the geometries of prime-focus and offset dual reflector antennas considered for the SKA, and introduces the performance figures of merit of radio telescopes, including the antenna aperture efficiency, system noise temperature and sensitivity. An overview of ultra-wideband (UWB) feed candidates for the SKA are presented in Chapter 3, including the comparative analysis of the performance. Chapter 4 describes the simulation methods utilized in the numerical study of the reflector antenna systems with the Eleven antenna feed. Chapter 5 and Chapter 6 present the results of the numeric study of the reflector antenna fed with the 2–13 GHz Eleven feed. The goal of this study is to determine the optimal geometry of the reflector (its F/D ratio and feed supporting structure) that will lead to the maximum overall system sensitivity. As the starting point of this analysis (see Chapter 5), we will model the system consisting of the reflector with the feed (as the source) only and will examine its performance over a wide range of F/D values to find $(F/D)_{\text{opt}}$. In Chapter 6, the reflector with the optimal F/D will be used as the baseline design and further analyzed, already in combination with the feed structure and its supporting struts. This study will include a careful treatment of the feed and strut blockage, as well as the analysis of its effect on the key performance parameters of radio telescopes, such as the aperture efficiency, spillover noise temperature, side-lobes and cross-polarization. We will show to which extent the above listed effects can be minimized by optimizing the position of the struts, both for the case of compact wideband Eleven antenna feed and conventional octave band horn.

Parameters and Performance Figures of Merit (FOM) of Radio Telescopes

THIS chapter describes the geometric parameters of prime-focus and offset dual reflector antennas and introduces the performance figures of merits of radio telescopes: The aperture efficiency, system noise temperature and sensitivity.

2.1. Parameters of Reflector Antennas

We describe two types of reflector antenna systems: Prime-focus and offset dual reflector systems, which are the considered design options for the SKA.

2.1.1. Axi-Symmetric Prime-Focus Reflector Antennas

The main design parameter of the prime-focus systems is the optics angle (illumination half-angle of the reflector as seen by the feed located at the focus). Typically, for radio telescopes this angle is in the range of $53\text{--}80^\circ$ and equivalent to F/D of $0.3\text{--}0.5$.

The geometry of the prime-focus parabolic reflector antenna is shown in Figure 2.1, described by parameters such as the focal length (F), the aperture diameter (D) of the reflector and the subtended half-angle (θ_o) defined as the maximum semi angle that is subtended by the reflector surface of the paraboloid.

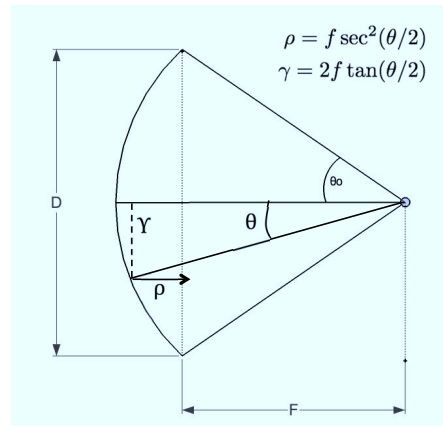


Figure 2.1.: The geometry of the prime-focus reflector antenna.

$$\theta_o = 2 \arctan \left(\frac{D}{4F} \right). \quad (2.1.1)$$

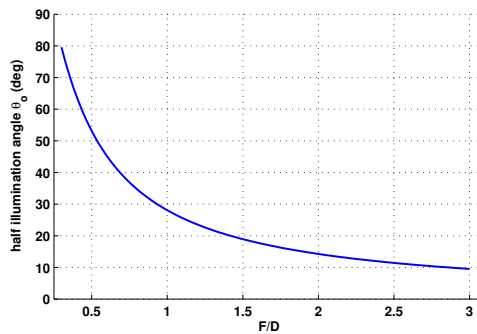


Figure 2.2.: The reflector illumination half-angle of the symmetric (equivalent) paraboloid versus F/D.

The ratio of the focal length to the diameter, the focal ratio (F/D), is commonly used in the mechanical design of reflector antennas and we will use the same name here as well as the names of the reflector subtended angle or optics illumination angle. Clearly, the beam pattern of the antenna feed should be matched to this angle to optimally use the available surface area. The present day radio telescopes have been designed such that the F/D is between 0.3 and 3, i.e. $80^\circ > \theta_o > 9^\circ$ (see Figure 2.2). The use of Cassegrain or Gregorian systems for which the equivalent focal length is longer than the actual focal length of the main reflector by the magnification factor $(e + 1)/(e - 1)$ with e the eccentricity of the subreflector can result in the F/D values by far exceeding one. The characteristic parameter of the Cassegrain or Gregorian systems is the illumination angle of the equivalent paraboloid with F/D.

The reflector antenna in the parametric study is a single reflector antenna with fixed diameter

(D) which complies with the definition above when the focal length is a variable.

2.1.2. Offset Gregorian Dual Reflector Antennas

A SKA reference design of the offset dual reflector systems is the Gregorian antenna (see Figure 2.3), the subtended half illumination angle of the subreflector of $45\text{--}65^\circ$. This geometry was chosen to satisfy the Mizusawa's condition [11] to realize low cross-polarization level in the beam axial direction. The exact value of the illumination angle for subreflector will depend upon the choice of the feed, but likely will be in the range of $55\text{--}65^\circ$ [9] to achieve the desired bandwidth.

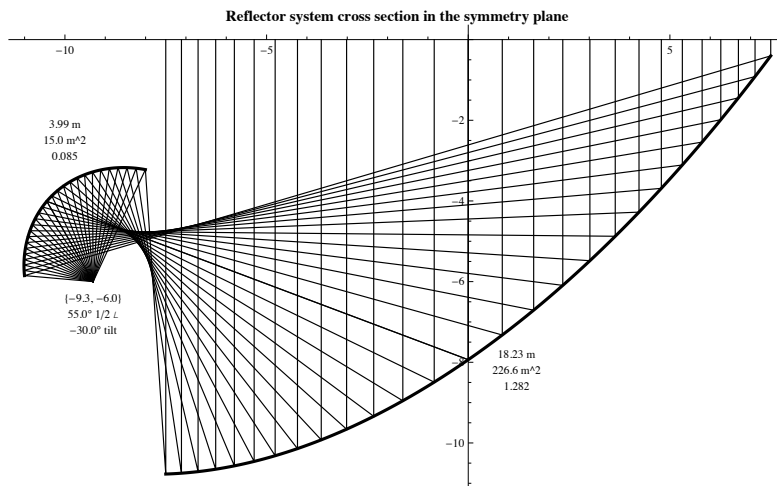


Figure 2.3.: The offset Gregorian reflector system cross section in the symmetric plane for the half illumination angle of 55° , the tilt angle of the boresight ray of -30° . The aperture diameter of sub-reflector is 4 meters, main reflector is 15 meters.

The parametric space of the considered Gregorian systems is very large, which includes the half illumination angle subtended by the edge of the subreflector, the locations of the focus and the feed, the tilt angle of the boresight ray [9], etc. Also, often the shaping can be used to control how the power from the feed is distributed across the aperture plane so as to increase the illumination efficiency and reduce the spillover loss. Since there is a large range of variable parameters of the Gregorian optics design, we perform a parametric study of the reflectors for prime-focus configurations only and then present the numerical results for one or two examples of the displaced axis dual reflector.

2.2. Performance Figures of Merit of Radio Telescopes

2.2.1. Aperture Effective Area

The key performance parameter of the radio telescope needs to be maximized is the sensitivity, defined as the ratio of the effective aperture (A_{eff}) to the system noise temperature (T_{sys}). A_{eff} is defined for the product of the physical area of the reflector aperture (A_{ph}) and the antenna aperture efficiency (η_{ap}) [12, Eq. 3.105, p. 71]:

$$A_{\text{eff}} = A_{\text{ph}} \eta_{\text{ap}}. \quad (2.2.1)$$

The aperture efficiency can be defined as [13, Eq. 22]:

$$\eta_{\text{ap}} = 2 \cot^2(\theta_o/2) \frac{|\int_0^{\theta_o} \text{CO}(\theta) \tan(\theta/2) d\theta|^2}{\int_0^\pi [|\text{CO}(\theta)|^2 + |\text{XP}(\theta)|^2] \sin \theta d\theta}, \quad (2.2.2)$$

where θ_o is the illumination half-angle of the paraboloid in the case of prime-focus paraboloid, and the illumination half-angle of the sub-reflector in the case of classical Cassegrain. Note: This definition is only valid to rotationally symmetric patterns.

The aperture efficiency can be further factorized by sub-efficiencies [12, Eq. 9.62, p. 365]:

$$\eta_{\text{ap}} = \eta_{\text{sp}} \eta_{\text{pol}} \eta_{\text{ill}} \eta_{\phi}. \quad (2.2.3)$$

The factorization improves the understanding of the separate contributions to the total efficiency. The key contributions are listed below. The spillover efficiency (η_{sp}) is the power within the illumination angle θ_o (i.e. the power hitting the reflector) relative to the total power radiated by the feed with the bodies of revolution (BOR) beam pattern

$$\eta_{\text{sp}} = \frac{\int_0^{\theta_o} [|\text{CO}(\theta)|^2 + |\text{XP}(\theta)|^2] \sin \theta d\theta}{\int_0^\pi [|\text{CO}(\theta)|^2 + |\text{XP}(\theta)|^2] \sin \theta d\theta}, \quad (2.2.4)$$

where CO is the co-polarization field and XP is the cross-polarization field. Co-polarization represents the polarization the antenna is intended to radiate while cross-polarization represents the polarization orthogonal to a specified polarization, which is usually the co-polarization. The relative spillover power ($1 - \eta_{\text{sp}}$) should be reduced as much as possible for the purpose of improving the efficiency. Moreover, it is a considerable contributor to the antenna noise temperature.

The polarization efficiency (η_{pol}) is caused by the polarization losses, which is defined by Collin [14] for linear polarization as the power of the co-polar field relative to the total power within θ_o . If we define the efficiency for circular polarization, it becomes

$$\eta_{\text{pol}} = \frac{\int_0^{\theta_o} |\text{CO}(\theta)|^2 \sin \theta d\theta}{\int_0^{\theta_o} [|\text{CO}(\theta)|^2 + |\text{XP}(\theta)|^2] \sin \theta d\theta}. \quad (2.2.5)$$

It is normally sufficient to apply (2.2.5) to both polarizations, and consider it as a measure of the reduction in efficiency due to phase and amplitude differences between the E- and H-plane far-field functions. The polarization efficiency is fairly high in most reflector antennas, which is better than -0.1 dB ($\sim 98\%$) typically. The illumination efficiency can be defined as

$$\eta_{\text{ill}} = 2 \cot^2(\theta_o/2) \frac{(\int_0^{\theta_o} |\text{CO}(\theta)| \tan(\theta/2) d\theta)^2}{\int_0^{\theta_o} |\text{CO}(\theta)|^2 \sin \theta d\theta}. \quad (2.2.6)$$

As one can see, the illumination becomes unity for a uniform aperture illumination, i.e., when $\text{CO}(\theta) = 1/\cos^2(\theta/2)$. The phase efficiency η_ϕ results from phase errors in the co-polar radiation field $\text{CO}(\theta)$, which can be obtained by

$$\eta_\phi = \frac{|\int_0^{\theta_o} \text{CO}(\theta) \tan(\theta/2) d\theta|^2}{(\int_0^{\theta_o} |\text{CO}(\theta)| \tan(\theta/2) d\theta)^2}. \quad (2.2.7)$$

This efficiency is the only sub-efficiency that depends on the location of the feed relative to the focal point of the reflector, provided the reflector is in the far field of the feed [13].

2.2.2. System Noise Temperature and Sensitivity

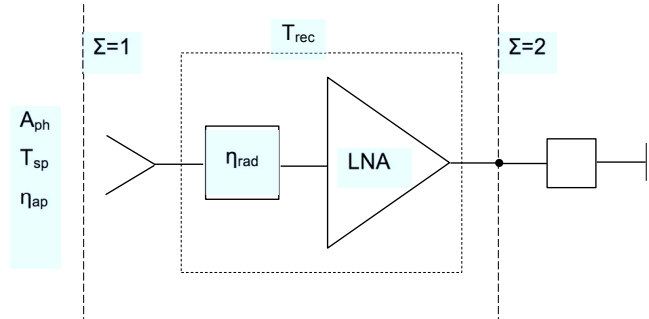


Figure 2.4.: An equivalent single-channel receiver model of the receiving array system.

The system noise temperature (T_{sys}) consists of several contributions due to both external and internal noise sources, such as the sky and the ground thermal noise, antenna conductor and dielectric material losses, and the low-noise amplifiers of the receiver [15, Eq. 22]. In our study, we will mainly focus on the components related to the antenna illumination and for this purpose will define T_{sys} in the following simplified manner:

$$T_{\text{sys}} = T_{\text{ext}} + T_{\text{rec}}, \quad (2.2.8)$$

where $T_{\text{ext}} = T_{\text{sp}}$ (spillover temperature), and T_{rec} comprises the contribution due to the antenna thermal noise (that can be calculated as $T_{\text{ant}} = (1 - \eta_{\text{rad}})T_{\text{amb}}$, where T_{amb} is the ambient noise temperature equal to about 300 K of non-cooled systems) and the noise temperature of the LNAs. In the numerical study presented here, we will assume T_{rec} is constant over frequency band and is equal to 10, 20 and 30 K. These values of the combined noise temperatures due to the antenna and LNAs are in the range of actual measured temperatures [16, Fig. 24, p. 14]. Therefore, the sensitivity in $\Sigma = 1$ (see Figure 2.4) can be defined as

$$\frac{A_{\text{eff}}}{T_{\text{sys}}} = \frac{A_{\text{ph}}\eta_{\text{ap}}}{T_{\text{sp}} + T_{\text{rec}}}. \quad (2.2.9)$$

As can be seen from equation (2.2.1), (2.2.3) and (2.2.8) the spillover loss of feed is a critical performance parameter that has to be minimized, since it reduces the aperture efficiency (via η_{sp}), and also increases the ground noise pick-up and hence the system noise temperature.

An Overview of the UWB Feed Developments for the SKA

AN overview of the UWB feed candidates for the SKA reflector antennas is presented in this chapter, including the pros and cons of the antenna performance, e.g. aperture efficiency and noise temperature, and their favored optics design. A summary table of these novel UWB feed concepts and designs is concluded.

During the last decade, a number of research groups across the world have been working towards the development of high efficiency feeds with wide bandwidth performance. There are several feed candidates for the SKA radio telescopes and other presently developed radio telescopes, e.g. the Allen Telescope Array (ATA) feed [17] employed in the ATA project [18], the quad-ridge horn from ETS-Lindgren [19], the quasi self-complementary (QSC) antenna with constant impedance that independent of frequency [20], the quad-ridged flared horn (QRFH) [21], an modified design of the previous ETS-Lindgren, and the Eleven feed [16], a low profile feed with a frequency invariant phase center location. Each candidate feed has different properties and unique traits, such as good input impedance, invariant phase center, or symmetric feed patterns. The optimal choice of the feed of radio telescopes depends on the combination of the feed and reflector antenna system designs. In this chapter, we give a brief description of the considered feed design options and discuss their potential for applications in the SKA-hi.

3.1. The Allen Telescope Array (ATA) Feed



Figure 3.1.: The Allen Telescope Array feed [18].

The ATA feed is an ultra wide band pyramidal log-periodic (LP) feed developed for the Allen Telescope Array. The motivation for the choice of this wideband feed was the development of very wideband low noise monolithic microwave integrated circuit (MMIC) receivers [22]. The dual polarization feed pattern is optimum for an offset Gregorian antenna with illumination of an equivalent focal length to antenna diameter (F/D) of 0.65, which provides a fairly large depth of focus on the telescope. This feed incorporates a novel central metallic “pyramid” that allows low-noise amplifiers (LNAs) to be housed in a small cryogenic dewar placed directly behind the antenna terminals at the small feed end (see Figure 3.1). Thus the cable losses are small which provides a low total effective receiver noise temperature [23]. Moreover, variation with frequency of phase center location along the antenna axis may require a mechanical actuator to move the feed into focus for good illumination efficiency of the telescope. It is also important to note that use of LP geometry does not guarantee frequency independence. Antenna shapes must be properly selected and tuned to ensure low standing wave ratio (SWR) and minimum variation of impedance and beamshape over a log-period of frequency [17]. The ATA feed has frequency coverage from 500 MHz to 10 GHz, with good match over the band. Input reflections of the feed itself are measured to be better than -14 dB over the operating band [23]. The following is the calculated performance. The feed directivity is about 12 dBi and the aperture efficiency for a half illumination angle of 60° is greater than 60% for most of the band, except at the low frequency end. The -10 dB half power beam width (HPBW) beam size is 42° in average, and has very little variation. The cross-polarization level is better than -10 dB and the noise temperature is below 25 K for most of the band [9]. The main problems with this feed are: (i) Significant losses due to phase center variation and (ii) large dimensions [24], therefore better feeds are desirable.

3.2. The Lindgren Feed



Figure 3.2.: The ETS-Lindgren horn 3164-05.

The Lindgren feed [19] is a commercial open boundary quad-ridged horn sold by ETS-Lindgren. It is a 2–18 GHz broadband antenna with dual polarization. This dual-polarized antenna can measure both orthogonal field components simultaneously. The novel part compared to traditional ridged horns is that the sides have been omitted (see Figure 3.2). Numerical analysis and measurements show that this open-sided or open-boundary horn provides a better and more stable pattern performance for the entire band of operation than the original design that had a cylindrical metal boundary around the ridges, as well as good directivity for its compact design. From measurements, it can be observed that the reflection coefficient is good for one polarization but not for the other one. The BOR_1 efficiency [25] of the horn is very good over the whole frequency band (> -1 dB) of 2–14 GHz. Moreover, different from the Eleven feed, the phase center of the ETS-Lindgren horn changes with the frequency. The main problems for the ETS-Lindgren horn are the input reflection coefficient, the variation of the beamwidth with the frequency. The latter reduces the aperture efficiency by few dBs at the higher frequencies [26]. In particular, the cross-polarization is very high, mostly above -10 dB, and as much as -6.7 dB in the high-end of the band, which is because the quad-ridge configuration of the Lindgren feed uses Vivaldi (exponentially taper) elements as radiator. The Glodstone Apple Valley Radio Telescope (GAVRT) program has adopted this feed to cover bandwidth from 4–14 GHz [9]. The computed aperture efficiency of the high frequency feed is greater than 40% over most of the band and greater than 55% from 6.0–13.5 GHz. The actual measured efficiency was slightly lower, which is approximately 40% over most of the band. These differences between simulations and measurements are due to some mirror misalignments and a worse than predicted main reflector surface root mean square (RMS). The measured zenith noise temperature contribution is below 35 K from 4.3–10.5 GHz. The beamwidth is 42° , which favors narrow angle optics.

3.3. The Non-Planar Quasi-Self-Complementary (QSC) Feed

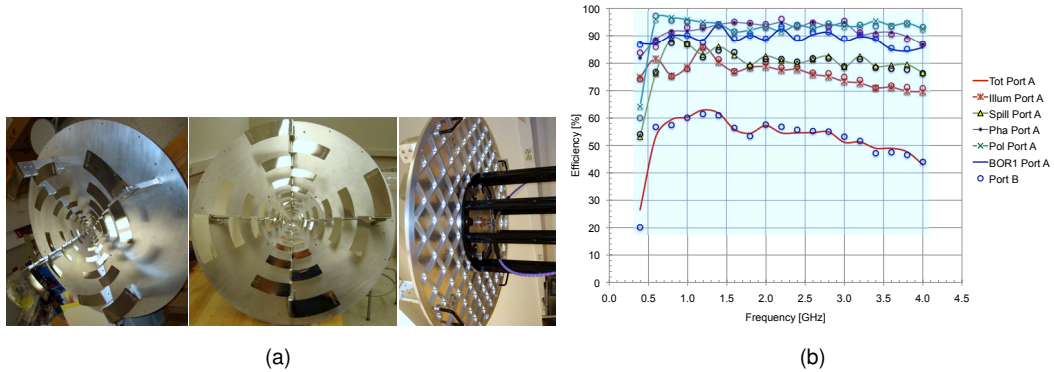


Figure 3.3.: (a) The QSC feed prototype. Perspective (*left*), front view (*center*), and back view (*right*); (b) prototype feed's efficiencies: Illumination, spillover, phase, polarization and total efficiency, calculated from measured patterns with an illumination angle of $\theta_o = 65^\circ$, and for both polarizations [20].

The QSC antenna is a novel dual-polarized ultra wide band feed that has been proposed in [27]. It is a non-planar tridimensional log-periodic structure in a QSC configuration, over a ground plane that exhibits frequency independent input impedance characteristics, over bandwidth in excess of 10 : 1. The QSC antenna has four-fold azimuth symmetry, i.e. its aspect remains invariant under 90° . It has four arms and is fed at the center of the structure, in a differential mode between two opposite arms, thus providing dual polarization. Each arm consists of a series of fingers placed radially in log-periodic fashion. The cross section of each finger varies from an elongated oval to flat, depending on the type of the QSC antenna. The QSC antenna has a low profile, i.e. its phase center location has a relatively small variation along its axis with frequency. The QSC antenna feed possesses these attributes that prove itself a qualified candidate for the SKA-hi feed, such as 10 dBi measured directivity, 65° average half beamwidth at -10 dB level oscillating between 60° and 70° , a almost fixed phase center location while frequency varies, and the input match is better than -10 dB over a decade-bandwidth [20], which is an essential trait. At this time, only measured antenna patterns of the QSC prototype that operates from 0.4–4.0 GHz are available. The measured patterns show that polarization efficiencies are about 90% and the spillover efficiency is at 80%, which are rather low for radio astronomy applications. The aperture efficiency of the QSC feed antenna is better than 50% up to 3.3 GHz (see Figure 3.3). The QSC feed antenna favors wide angle optics such displaced axis dual reflector optics..

3.4. The Quad-Ridged Flared Horn (QRFH)

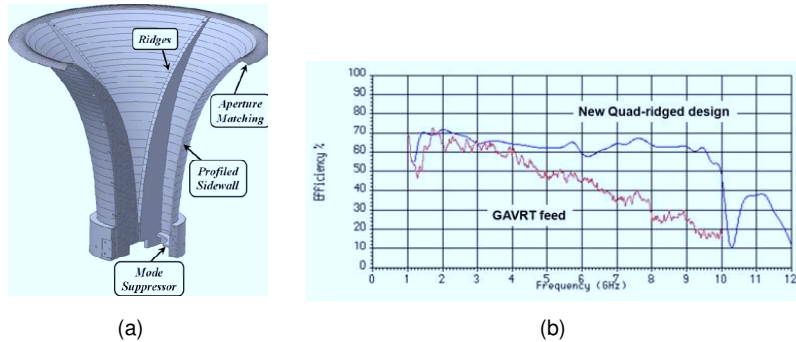


Figure 3.4.: (a) A wideband quad-ridged feed. (b) The efficiency of GAVRT and QRFH [9].

Wideband log-periodic type feeds that consist of wire type elements for the radiating structure, such as the ATA feed, the Eleven feed, and the QSC feed, have difficulty to cool for LNAs due to the thin wire connection. Also, they tend to have very delicate and small feed connection area. The open-boundary quad-ridged commercially available Lindgren feed [19] can easily be cooled and is very robust. However, the drawback of this feed is that it is not as wideband as the other candidate feeds. Improvements for optimizing a quad-ridged feed for wider bandwidth are in progress. The genesis of the design was the ETS-Lindgren 3164-05 commercially available horn, which is mentioned above. Key features are (see Figure 3.4a): Ridges, which provide for a lower cutoff of the dominant mode by as much as a factor of four, and the exponential ridge profile presents a smooth impedance transition from 50 to 377 ohms; profiled sidewall, which manipulates the phase over the aperture to maintain constant beamwidth and minimizes electromagnetic interaction with the surrounding environment; aperture matching, which minimizes edge diffraction from aperture edges and introduces curvature to high frequency wave fronts; mode suppressor, which attenuates higher order modes around the launch point.

A version of the QRFH was designed to work in the SKA-hi. The design frequencies are 1.4 to 10 GHz and the subreflector illumination angle is 55° . The efficiency improvement of the QRFH compared to that of the GAVRT Lindgren feed is quite apparent (see Figure 3.4b), where the QRFH uses computed primary patterns and measured primary feed data is used for the GAVRT feed. The efficiency is over 60% in most of the band. The QRFH is a unique feed that accommodates different optics and input impedance requirement [9].

3.5. The Eleven Antenna Feed

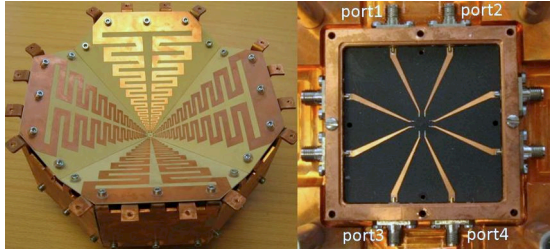


Figure 3.5.: The manufactured Eleven feed and the descrambling board at the rear side of the ground plane (amplified, not in scale) [16].

The Eleven antenna is a decade-bandwidth log-periodic dual-dipole array, and it has been developed at Chalmers University of Technology (Chalmers) since 2005. The design is based on the log-periodic version of the dual dipole feed in [28]. The feed is referred to as the Eleven antenna because its basic configuration is two parallel dipoles (| | shape) half-wavelength apart and because it can be used over more than a decade bandwidth with 11 dBi directivity [29]. This Eleven feed operates over the band of 2–13 GHz, which is a cryogenically cooled system that is integrated with cryogenic LNAs.

The large bandwidth of the Eleven antenna is obtained by cascading folded dipoles one after another with log-periodic scaling factor k within each petal (see Figure 3.5 (left)). The log-periodic array of the Eleven feed is excited at the center, and the first folded dipole pairs are approximately half-wavelength dipoles at a frequency which referred to as the highest geometrical frequency $f_{\text{geo,max}}$. The next dipole pair has a geometrical frequency $f_{\text{geo,max}}/k$, and so on. The last folded dipole pair has then the geometrical frequency $f_{\text{geo,max}}/k^N$, where N is the number of folded dipole pairs used in the array. The outermost folded dipole of each petal is short-circuited at its outer port for mechanical reasons and to achieve better thermal conduction. The compact central feeding region where the two opposing log-periodic dipole petals are combined, referred to as the center puck [30]. At the latest progress, a transition from dipoles to microstrip lines was designed to couple the four radiating dipole arrays on the front side of the ground plane to a descrambling board on the rear side that is integration with LNAs (see Figure 3.5 (right)) [16]. The Eleven antenna is a multi-port antenna, namely the total radiation patterns will be dependent on the patterns of each individual antenna channels, i.e. the pedals.

The Eleven antenna has almost no phase center variation and almost constant beamwidth over a decade bandwidth, which are two unique traits that has not been found in other UWB antennas. Also, due to its low profile and relatively compact geometry, the cooling solution (in terms of the power consumption and performance) is cost-effective. Therefore, the total aperture efficiency

is high for a large bandwidth, and for the case of the reflector with a half illumination angle of 60° , it is higher than -3 dB (50%) from 2 to 13 GHz. The agreement between the simulated and measured directivities is within only 1.5 dB between 2.3 and 14 GHz [16]. These properties demonstrate that the Eleven feed can be good candidate for the reflector antenna systems for the SKA-hi technology. The system noise temperature averaged over 2.7 to 10 GHz is 20.7 K in the measured case, and 20.5 K estimated by simulation. The current activities of the Eleven feed project include the development of more accurate noise model of the feed so as to explain the difference between the measurements and simulations at low frequencies and reducing the size of the feed. The increased system noise temperature below 2.7 GHz and above 10 GHz can be explained by reference to the BOR_1 efficiency and the spillover [16].

Normally, log-periodic antennas are not common as reflector feeds due to their phase centers vary strongly with frequency, e.g. the ATA feed. However, the Eleven antenna is a compact feed that overcomes the drawback with almost no phase center variation and constant beamwidth over a decade bandwidth. Its compact size also facilitates cryogenic cooling.

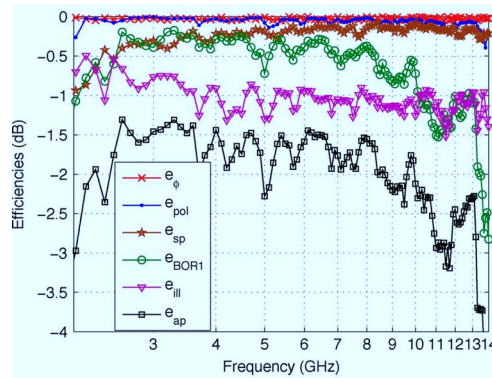


Figure 3.6.: The aperture efficiency and its sub-efficiencies as calculated from the measured patterns of the Eleven feed [16].

3.6. Comparison of the Feeds

Table 3.1 indicates the Eleven feed is a one of the best candidates so far for the SKA radio telescopes. The concepts of the QSC feed and the QRFH also have good potential, but require more in-depth study as well as experimental verification of the predicted efficiencies and the system noise temperature measurements. The performance study of the considered SKA designs fed with the Eleven feed is presented in Chapter 5.

Table 3.1.: A summary of the pros and cons of several novel UWB feed concepts and designs.

UWB Feeds	ATA Feed	Lindgren Feed	QRFH	Eleven Feed	QSC Feed
Directivity	12 dBi (exc. lower freq. end)	11.7–15.1 dBi	N/A	11 dBi	> 10 dBi (exc. lower edge)
Input Imp. Match	< -14 dB	< -4.5 dB	< -6 dB	< -10 dB	< -10 dB
Cross-Pol. Level	< -10 dB (mostly)	> -10 dB (mostly) < -6.7 dB (higher edge)	N/A	< -10 dB up to $f/f_0 = 5$ ^a	< -11 dB
Frequency Range	0.5–10 GHz	4–14 GHz	1.4–10 GHz	2–13 GHz	0.4–4 GHz
Bandwidth	> 15 : 1	3.5 : 1	6 : 1	7 : 1	10 : 1
10 dB Beamwidth	avg. 42° (very little var.)	30–46°	55°	50–56° (avg. 53°) ^a	60–70° (avg. 65°)
Optics Used	offset Gregorian F/D = 0.65 ($\theta_o = 42^\circ$)	offset Gregorian F/D = 0.6 ($\theta_o = 45^\circ$)	offset shaped Gregorian, F/D = 0.48 ($\theta_o = 55^\circ$)	prime-focus, F/D = 0.443 ($\theta_o = 60^\circ$)	offset Gregorian F/D = 0.4 ($\theta_o = 65^\circ$)
Aperture Eff. of Feed Pattern	avg. 60% (-2.2 dB)	~ 40% mostly	> 60% (-2.2 dB) ^b	> 50% (-3 dB)	> 50% (-3 dB) up to 3.3 GHz
Sys. Noise Temp.	< 25 K mostly	< 35 K at 4.3–10.5 GHz	< 25 K at 2–12 GHz	~ 20.7 K at 2.7–10 GHz	N/A
Pros	a low total receiver noise temp., good input match	high η_{BOR1} , low side lobes	smooth radiation pattern, good input match exc. high freq.	low profile, invariant phase center, constant beamwidth	good input match, symmetric pattern
Cons	a complex and delicate integration of the LNA with the feed, varied phase center	bad input match, varied beamwidth and phase center, low aperture eff., high XPL	large diameter	low $\eta_{BOR1} > 10$ GHz, increased noise temperature at < 2.7 GHz and > 10 GHz	polarization that squints with frequency, no hardware has been realized > 4 GHz

^aOnly have partial feed pattern data for the figures.

^bPredicted performance.

Methodology for the Analysis of Reflector Antennas

THIS chapter describes the simulation methods utilized in the numerical study of the reflector antenna systems with the Eleven antenna feed. The methodology and theory are introduced in Section 4.1. The specification details of simulations performed in TICRA's software GRASP 9 [31] are presented in Section 4.2.

4.1. Numerical Methods

There are a number of methods applied in antenna analysis, such as Physical Optics (PO), Physical Theory of Diffraction (PTD), as well as ray techniques Geometrical Optics (GO) and Geometrical Theory of Diffraction (GTD), etc. For our study we have employed a combined PO-PTD method.

4.1.1. Physical Optics (PO)

A general scattering problem can be formulated as a combination of a known incident field E_i and the field E_s from the scatterer with known geometry and electrical surface properties. Then, the total field E is computed as

$$E = E_i + E_s . \tag{4.1.1}$$

In GRASP 9 if the surface of the scatterer is made of a perfect conducting material, the scattered field is generated by the induced surface electric currents on the scatterer. For a non-perfect con-

ducting surface, a set of equivalent electric and magnetic surface currents is computed which produce the scattered field. In our study, we have modeled the former case. The simulation procedure can be divided into three steps:

STEP 1 Calculation of the induced surface currents on the reflector due to a specified source on transmit (see a sub-section 4.2.2 Tabulated feed). The exact solution of the surface currents can be obtained in GRASP 9 with the method of moments (MOM). However, for electrically large scatterers such as in our study, this method is computationally expensive and the PO approximation of the induced currents can be used.

STEP 2 Calculation of the field E_s produced by these currents and scattered towards the direction of observation. This step involves no further approximations since the radiation integral of the surface currents can be computed by numerical integration with high precision.

STEP 3 Addition of the incident field E_i and scattered field E_s to obtain the total field.

4.1.2. Physical Theory of Diffraction (PTD)

As explained in Section 4.1.1 the PO method gives an approximation to the scattered field

$$E_s \approx E_{PO} . \quad (4.1.2)$$

The PO currents approximate the induced currents on a scatterer derived from scattering by an infinite planar surface. Thus, the special behavior of the currents close to an edge of the scatterer is not modeled by PO. In the PTD the difference between the exact induced currents and PO currents is approximated by considering the induced currents on an infinite perfectly conducting half plane illuminated by a plane wave. These PTD currents are therefore a correction to the PO currents such that the radiated PTD field is a correction that must be added to the PO field for obtaining the scattered field

$$E_s \approx E_{PO} + E_{PTD} . \quad (4.1.3)$$

4.2. Models and Simulation Specifications of the Software Package GRASP

The software GRASP 9 is commercially available numerical tool for analyzing reflector antennas that has been developed by TICRA (Denmark). The simulation environment setup of the reflector and feed models in GRASP 9 is described below.

4.2.1. Reflector Antenna Models

A reflector is defined by means of a reflector surface and a reflector rim. Both of these two items are specified in the same coordinate system as illustrated in Figure 4.1.

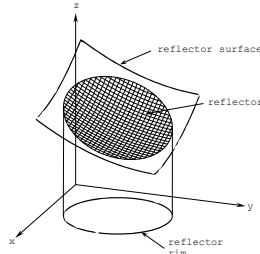


Figure 4.1.: A reflector model in GRASP 9 is defined by a reflector surface cut of a cylinder with the reflector rim as the cross section [32].

4.2.1.1. Reflector Surfaces

In GRASP 9, the surface is represented by a general function

$$z = F(x,y). \quad (4.2.1)$$

The shape of this surface must therefore be a well-defined function of the independent variables x and y within the region determined by the rim of the reflector. There are various surface options available such as ellipsoid, hyperboloid, paraboloid, pyramidal surface, etc. Reflector rims The rim of a reflector is defined as the intersection between the reflector surface (including possible distortions) and the cylinder in the z -axis direction with a cross section given in the xy -plane (see Figure 4.1). There are various built-in reflector rim objects such as circular, elliptical, rectangular, triangular rim, etc.

In our studies, we use the paraboloid surface and the circular rim in a prime-focus single reflector system, for which the aperture diameter of the main reflector is 12–15 meters and the focal length varied between 3.6–8.4 meters that correspond to the focal ratio of $F/D = 0.3$ – 0.7 .

4.2.2. Feed Models

The feed system is the radiating source of an antenna system that is defined in transmit situation. It may consist of one or more feed elements. A special type of feed, a plane wave illumination of the antenna system is also possible that represents receive situation. In our evaluation, we have only considered the transmit case and applied the following models of the feed:

- **Tabulated Feed Model for the Eleven Feed**

A general way to represent the radiation from a feed is through tabulated data from its radiation pattern, which may originate from measurements or calculations. The radiation pattern data includes two or three polarization components depending whether field is given in the far-field or in the near-field regions. The radiation pattern of the feed used in our analysis is the measured far-field pattern of the Eleven feed, which consist of radiated fields on phi- and theta-plane.

- **Cosine Feed Model for a Benchmark Case**

For performing validation tests, we have used a cosine feed pattern built by tabulated pattern, $\cos^n(\theta/2)$. This model was used as a reference rotationally symmetric pattern for which the analytic solution of the efficiency is known [13, Eq. 30].

4.2.3. Strut Models

Struts in single and dual reflector antennas are used to support the feed system and subreflector in rotationally symmetric systems. These struts may have a serious impact on the antenna performance. The efficiency and cross-polarization is degraded and the side lobe level is increased.

It is possible to analyze the scattering effects from strut elements having circular or polygonal cross section in GRASP. The struts having circular cross section are defined by the position of the end points and the radius. The struts having polygonal cross section are defined by the position of the end points and the shape of the polygonal cross section. The methods of modeling the struts will be described in Chapter 6.

4.2.3.1. Typical Strut Contributions

The three most important mechanisms by which the struts influences the antenna radiation are described below:

1. Plane Wave Strut Scattering

The first effect on the far-field due to the struts is illustrated in Figure 4.2a. After hitting the reflector the wave (very often plane but it is not a requirement) is scattered in the strut.

2. Spherical Wave Strut Scattering

Another field contribution due to strut scattering is illustrated in Figure 4.2a. The field (spherical wave) from the feed hits the strut and most of this scattered field hits the reflector and is partly reflected in the direction of the main beam.

3. Reflection in the main reflector of the scattered field from the struts, where the incident field on the strut comes from the main reflector.

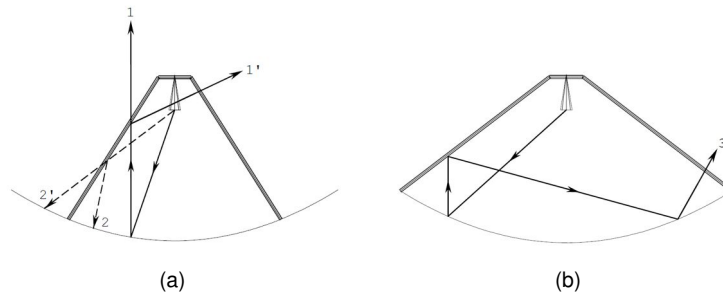


Figure 4.2.: Strut scattering of type (a) 1, 2 and (b) 3.

The degradation of the peak gain (efficiency) is mainly due to the effects (1) and (2) of which (2) is only important in a system where the struts are not supported by the outer edge of the main reflector as in Figure 4.2a. The side lobe will mainly be affected by the strut scattering (1') and (3) where (3) is only important in a configuration as shown in Figure 4.2b. Although these scattering effects are illustrated for a single reflector system, they will also be the dominant effects in a dual reflector system in which the feed is replaced by the subreflector. However, in our study we only considered the first two types of strut scattering as the third type was omitted.

4.2.4. Format of Input/Output Field Data

4.2.4.1. Spherical Cut

In GRASP 9, the class *Spherical Cut* defines field points in cuts on a sphere where the field shall be calculated. Polar as well as conical cuts can be specified, both in the near-field and in the far-field region. Under this class, one can use parameter *theta_range* to define the range of the polar angle θ and *phi_range* to define the range of the azimuthal angle ϕ , and the number of points for both values. The more the number of cuts is, the finer the result is; however, it is also more computationally expensive. We have performed a number of validation tests to determine the required number of cuts. The results are presented in terms of *discretization* parameter that is the radial distance between the adjacent cuts over ϕ and θ (see Figure 4.5–4.6 in Section 4.3.2).

4.2.5. Convergence of the Physical Optics Integral

The PO integration grid is specified by the two variables *po1* and *po2* in GRASP 9. The values of these variables can either be determined automatically by GRASP 9 or be set to suitable values manually. Too small values of *po1* and *po2* will result in inaccurate fields since the PO integral has not converged, and large values, on the other hand, will take more computation time than

necessary.

For some scatterer types it is possible to give simple rules for estimating po1 and po2. If the scatterer is a focused reflector with circular rim the PO integral will converge if

$$\text{po1} = \text{nint}(z/2.4), \quad \text{po2} = \text{nint}(z) \quad (4.2.2)$$

where

$$z = 1.09 \pi \frac{D}{\lambda \sin \theta_o} + 10. \quad (4.2.3)$$

The function nint gives the nearest integer to the argument, D is the reflector diameter, λ is the wavelength and θ_o is the half-illumination angle of the main reflector. If the aperture is defocused it may be necessary with up to two times these values. In general the physical integral is easiest to calculate for focused reflectors and close to the main lobe because the integrand in the PO integral is then a slowly varying function of the integration variables. As the observation point moves into the side-lobe region the integrand becomes increasingly oscillatory which requires a finer integration grid resulting in longer computation time.

The necessary values for po1 and po2 to obtain a convergent solution depend both on the current distribution on the reflector and on the location of the output points. In our simulations, we have used the automatic procedure in GRASP 9 which can assure a convergent result is achieved. One can change the value of *field accuracy* to define the required accuracy of the calculation. For instance, if the field accuracy is -80 dB this means that the field error due to convergence is at least 80 dB below the maximum value of the field at any of the field points. In the studies the field accuracy is set to -80 dB.

4.3. Antenna Aperture Efficiency Calculation Methods

4.3.1. Description of the methods

We have utilized two approaches to calculate the aperture efficiency η_{ap} :

Approach I Based on equation (2.2.1), computing the aperture efficiency via the antenna directivity, defined in a given direction of observation:

$$\eta_{\text{ap}} = \frac{A_{\text{eff}}}{A_{\text{ph}}} = \frac{D_{\text{max}} \lambda^2}{4\pi} \frac{1}{A_{\text{ph}}}, \quad (4.3.1)$$

where D_{max} is the simulated antenna directivity in GRASP 9.

Approach II Compute the aperture efficiency via the antenna radiation pattern [13, Eq. 22]

$$\eta_{\text{ap}} = 2 \cot^2\left(\frac{\theta_o}{2}\right) \frac{|\int_0^{\theta_o} \text{CO}(\theta) \tan(\theta/2) d\theta|^2}{\int_0^\pi [|\text{CO}(\theta)|^2 + |\text{XP}(\theta)|^2] \sin \theta d\theta}, \quad (2.2.2)$$

where θ_o is the illumination half-angle of the paraboloid for a prime-focus system; and the illumination half-angle of the subreflector for a classical Cassegrain.

Note that (2.2.2) is only valid to *rotationally symmetric patterns* (the limit of upper integration is $0-\theta_o$). However, antenna feed patterns are not symmetric in practice, so one should take into account the BOR_1 efficiency as defined in [25]. Alternatively, one can consider only half of the asymmetric radiation pattern cut on ϕ -plane while performing the integral of (2.2.2), and calculate the *mean* of aperture efficiency in the range of $0-360^\circ$ on ϕ -plane, see (4.3.2), which is integrated in MATLAB (see Appendix A).

$$\eta_{ap} = \frac{\sum_{n=0}^N \eta_{ap, \phi=n}}{N+1}, \quad (4.3.2)$$

4.3.2. Numerical Comparison of the Methods

The aperture efficiency of the standard cosine feed for a benchmark case and the Eleven feed is shown in Figure 4.3 and Figure 4.4a. The efficiency of the measured primary and the simulated secondary patterns are computed by equation (2.2.2) and (4.3.1) respectively for the Eleven feed. As can be seen in Figure 4.3, the differences between the efficiencies based on the simulated secondary and the primary patterns for the standard cosine feed are $\sim 0.1\%$ (-30 dB). The differences for the Eleven feed are in the same order. These validation tests are satisfactory and give us confidence in the numerical results adopting the above methodology.

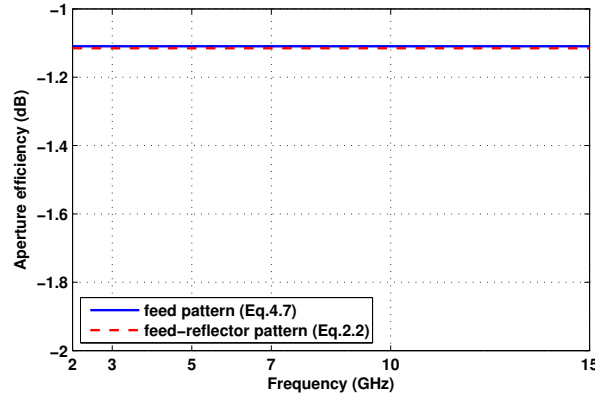


Figure 4.3.: The aperture efficiency of the standard cosine feed illumination the reflector antenna with $F/D = 0.43$, computed with the primary field patterns by equation (2.2.2) and the secondary field patterns by equation (4.3.1).

To determine the optimal number of cuts N_{cut} in ϕ -plane in *spherical cut* for our study, we have performed several simulations for different N_{cut} from 8–90, i.e. the discretization step $\Delta\phi$,

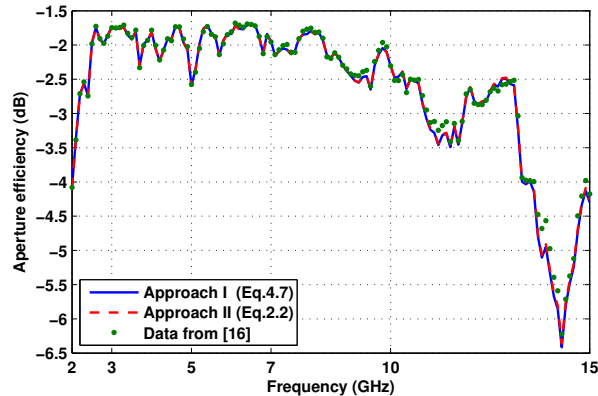


Figure 4.4.: The aperture efficiency of the Eleven feed illumination the reflector antenna with $F/D = 0.43$: Accounting for the BOR_1 efficiency [16], computed with the measured primary patterns by equation (2.2.2) and the simulated secondary patterns by equation (4.3.1).

the distance between each cut on ϕ -plane, is $4\text{--}45^\circ$. The aperture efficiency computed from the simulated antenna patterns for different discretization steps and its relative standard error as a function of azimuthal discretization step are shown in Figure 4.5. The side lobe and cross-polarization level at HPBW level (both in E-plane) are presented in Figure 4.6. The convergence of the aperture efficiency depends on frequency and can be achieved with a relatively large discretization ($\sim 45^\circ$) for frequencies below 6 GHz, but requires discretization smaller than 15° for higher frequencies. Nevertheless, one only needs discretization step of 20° to achieve quite accurate aperture efficiency, which is relatively time-efficient. The results of the side lobe level confirm the above observation that required discretization steps are frequency dependent, Hereby suggesting a fine discretization step of 15° to achieve a good convergence. Similar dependence was observed in the cross-polarization levels.

The azimuthal discretization step $\Delta\phi$ for the studies in Chapter 5 was set to 5° so as to provide accurate results. The discretization of polar angle $\Delta\theta$ was varied with respect to different case study, which was mostly set to 60 points within $\theta = 0\text{--}3^\circ$, i.e., the polar discretization step $\Delta\theta$ is 0.05° .

Conclusions

It is greatly essential to choose the appropriate numerical integration methods and sufficient fine discretization step $\Delta\phi$ for the accurately evaluation of the aperture efficiency. Numerical methods that fail to provide high accuracy will lead to inaccurate numerical results. Figure 4.7 demonstrates the aperture efficiency computed by applying different numerical integration methods on calculating equation (2.2.2): *Riemann left sum* [33], *midpoint rule* [34] and *Simp-*

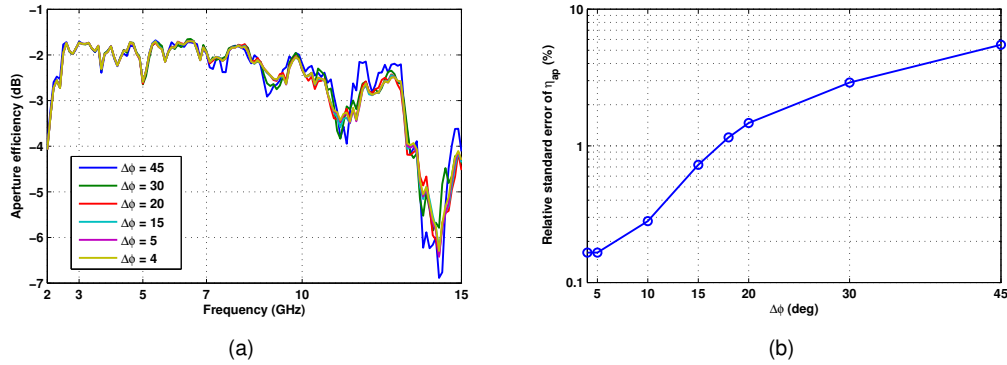


Figure 4.5.: (a) The aperture efficiencies of the Eleven feed as a function of frequency for varied azimuthal discretization steps. (b) The relative standard error of the computed aperture efficiency as a function of azimuthal discretization step.

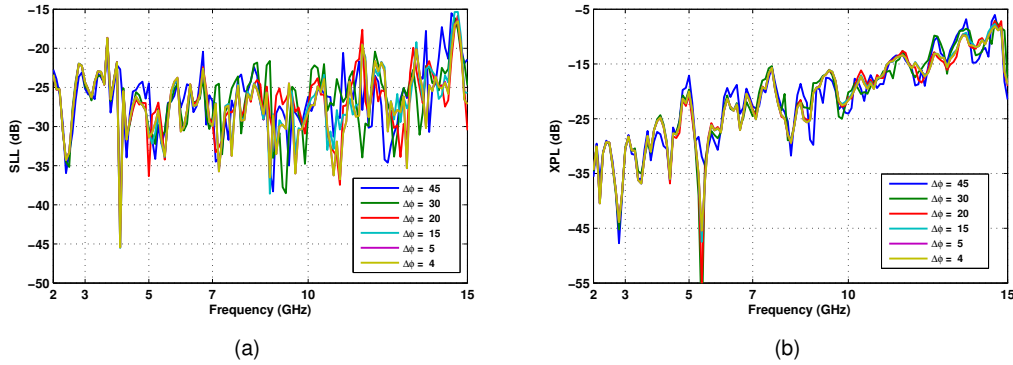


Figure 4.6.: (a) The first relative side lobe level and (b) the relative cross-polarization level as a function of frequency for varied azimuthal discretization steps.

son's rule (see Appendix A). Riemann left sum produces inaccurate results, which have notable disagreement with the two other methods. On the other hand, midpoint rule and Simpson's rule provide quite precise estimates that converge to certain values. We used Simpson's rule in our studies because its accuracy (see Table 4.1). The two approaches of computing aperture efficiency by equation (4.3.1) and (2.2.2) generate similar results.

In order to evaluate the antenna performances accurately, the discretization steps ($\Delta\phi$ and $\Delta\theta$) shall be chosen carefully. Generally, finer discretization step will provide more exact simulation results. However, it is also more computationally expensive. To maintain the balance between accuracy and time efficiency, we concluded the required discretization steps for satisfactory simulation results, i.e., $\Delta\phi = 15^\circ$. One can choose the discretization steps based on this conclusion, not only dose which provide relatively accurate results, but also saves computation time.

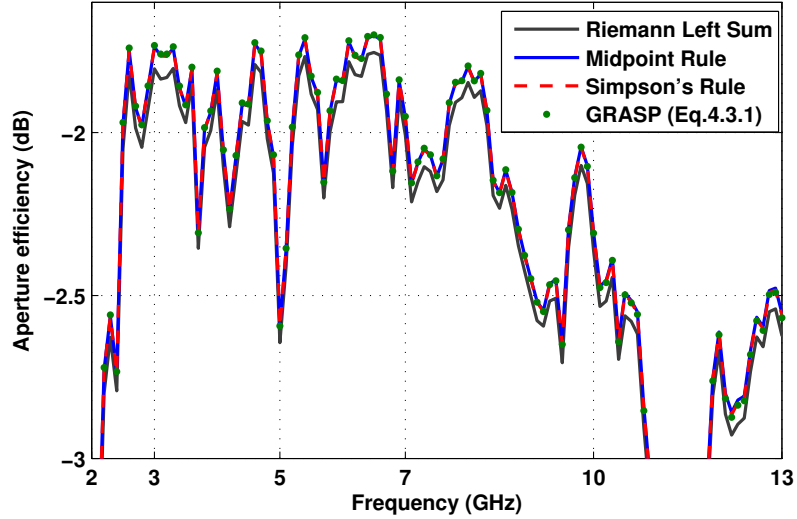


Figure 4.7.: The aperture efficiency of the Eleven antenna illumination the reflector antenna with $F/D = 0.43$, computed with the measured feed patterns by applying three different numerical integration methods (Riemann Left Sum, Midpoint Rule and Simpson's Rule) on equation (2.2.2) and the simulated secondary field patterns in GRASP 9 by equation (4.3.1).

Table 4.1.: The relative error of the computed aperture efficiencies based on the feed patterns in Figure 4.7, with respect to the reflector antenna simulations in GRASP.

	$ \Delta\eta_{ap} $ (dB)
Riemann left sum	-0.0019
Midpoint rule	-0.0656
Simpson's rule	-0.0754

Analysis of the Reflector Antenna Performance for Various F/D Ratios

THE objective of the present chapter is to perform a numerical study of the axi-symmetric reflector antenna system in combination with the 2–13 GHz Eleven feed, and to determine the optimal reflector geometry (F/D) that will lead to the maximum system sensitivity. As the starting point of this analysis the system consisting of the reflector with the feed (as a source) is modeled and its performance is evaluated over a wide range of F/D so as to find $(F/D)_{opt}$.

5.1. The Prime-Focus Reflector System with the Eleven Feed

Simulation results of the performance of the prime-focus reflector antenna system with the Eleven feed, carried out in GRASP 9, are presented. Note that the effects of the feed and strut blockage have not been considered here, but are studied in the next chapter. The purpose of this study is

- to understand the effect of the reflector geometry (namely the optics illumination angle) on the aperture efficiency, the maximum side lobe level and cross-polarization, and temporal beam stability due to gain drifts of the LNAs.
- to determine the range of the optimal F/D values that provide the best performance. The characteristic parameter *illumination half-angle* θ_o (see Figure 2.1) of the reflector is used as a variable.

The primary and secondary far-field patterns of the reflector antenna system are shown in Section 5.1.1. The primary patterns—the Eleven feed patterns—are measured results [16], and the secondary patterns were simulated in GRASP 9 by using the measured feed patterns (see Section 4.2). Section 5.1.2 and 5.1.3 present the aperture efficiency, the first side lobe and the relative cross-polarization levels, calculated from the simulated antenna patterns, over the frequency band from 3 to 12 GHz. Section 5.1.5 presents the analysis of temporal beam stability (in the direction of observation and at the HPBW level) which quantifies how the shape of the antenna pattern changes due to the gain drifts of the four-to-one power combining feeding network of the Eleven feed, which includes four LNAs. This characteristic parameter is one of the main limited factors of the imaging dynamic range of radio telescopes. In the study of temporal beam stability, we used the simulated Eleven feed patterns obtained in CST [35], defined directly at the four output terminals of the antenna.

5.1.1. Far-Field Patterns

Figure 5.1–5.4 show the normalized co- and cross-polarization far-field patterns of the Eleven feed of the total reflector antenna system with 60-degree half illumination angle and 12-m aperture diameter.

5.1.2. The Half Power Beam Width (HPBW) and Polarization

The Half power beam width is the angle between the half-power (-3 dB) points of the main lobe of the radiation pattern. Figure 5.5a shows how the HPBW varies with frequency for different reflector illumination angles in $\phi = 45^\circ$ plane, and the relative cross-polarization level at these HPBW directions are presented in Figure 5.5b. In the considered frequency range, the HPBW varies from 0.1° to 0.6° , in which the relative cross-polarization level is less than -10 dB for the entire frequency band. We chose to demonstrate the relative cross-polarization level in $\phi = 45^\circ$ plane because it presents the worst case (see Figure 5.6a).

Cross-polarization level (XPL) is defined by the relative cross-polarization level:

$$\text{XPL} = 10 \log\left(\frac{|E_{\text{xp}}|}{|E_{\text{co}}|}\right)^2 \quad (\text{dB}), \quad (5.1.1)$$

where E_{co} and E_{xp} are the co- and cross-polar components in electric fields.

The on-axis cross-polarization level of prime-focus reflector system with the Eleven feed was found to be smaller than -16 dB over the frequency band of 3–13 GHz. Figure 5.6b shows the relative XPL at HPBW as a function of half illumination angle for frequencies between 3 and 13 GHz, in which the minima occurred in the region of the half illumination angle of 55–

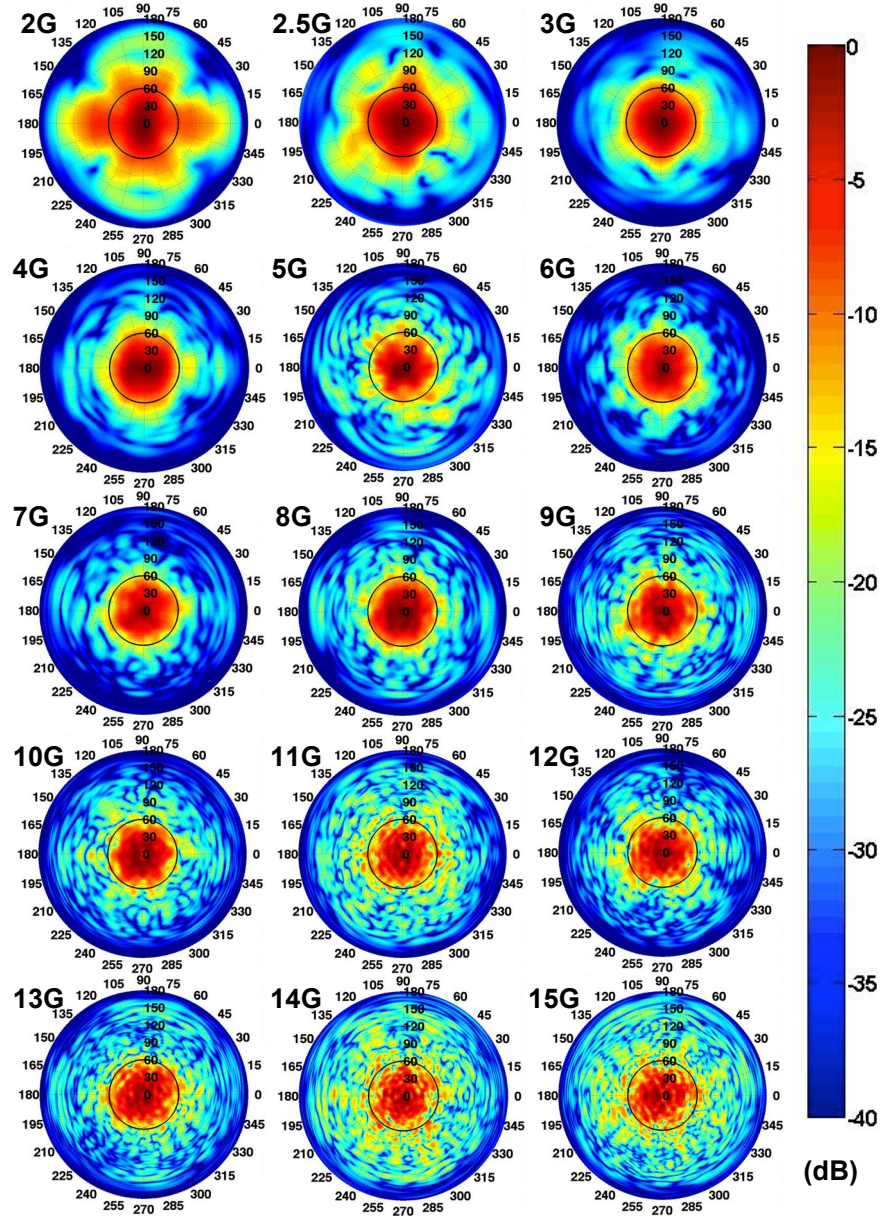


Figure 5.1.: The normalized measured co-polar far-field patterns of the Eleven feed (Ludwig 3 co-polarized component), the range of θ is $0-180^\circ$ and ϕ is $0-360^\circ$. The black line on the patterns indicates the directions towards the rim of the reflector corresponding to $\theta = 60^\circ$.

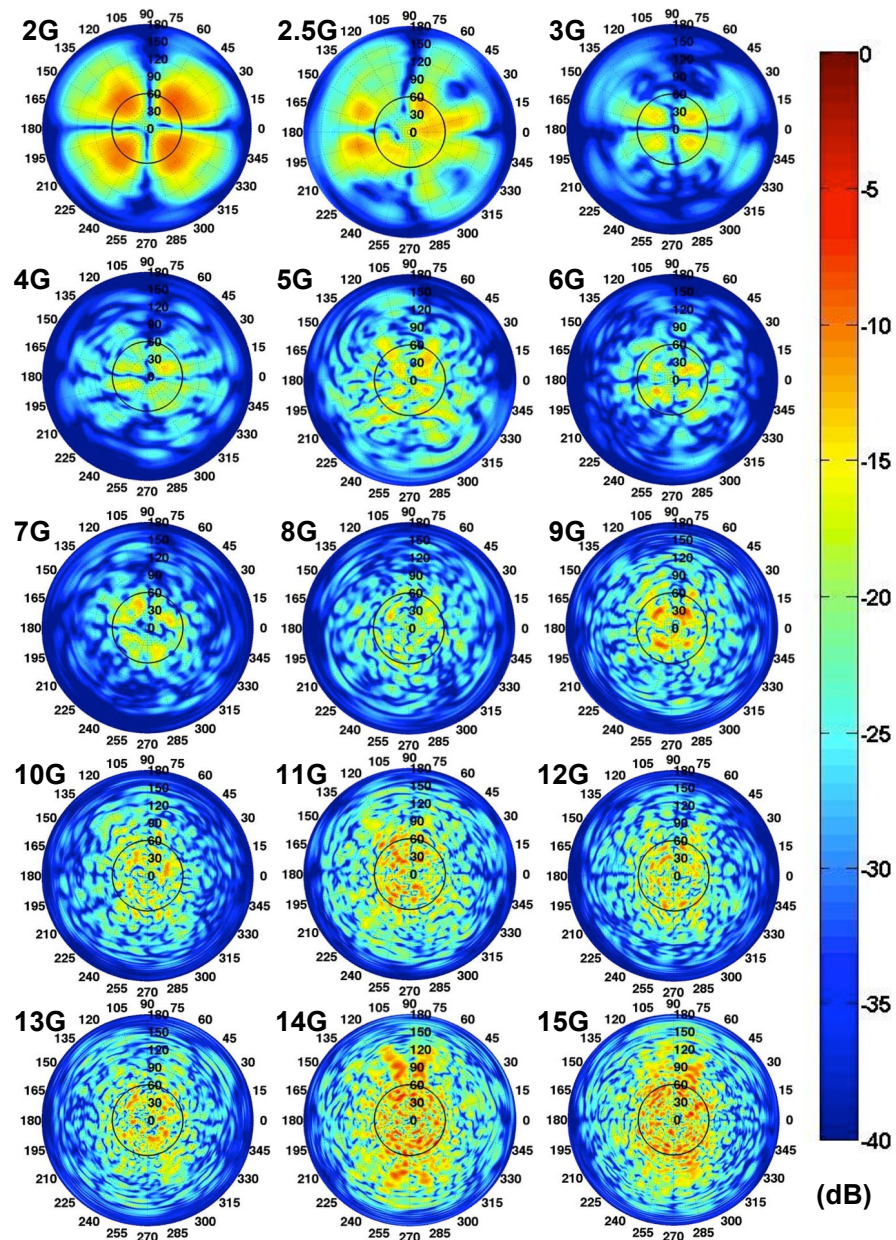


Figure 5.2.: The normalized measured cross-polar far-field patterns of the Eleven feed (Ludwig 3 cross-polarized component), the range of θ is $0-180^\circ$ and ϕ is $0-360^\circ$; the asymmetry is related to the difference between the gains of the power combiners used to feed the antenna during measurements. The black line on the patterns indicates the directions towards the rim of the reflector corresponding to $\theta = 60^\circ$.

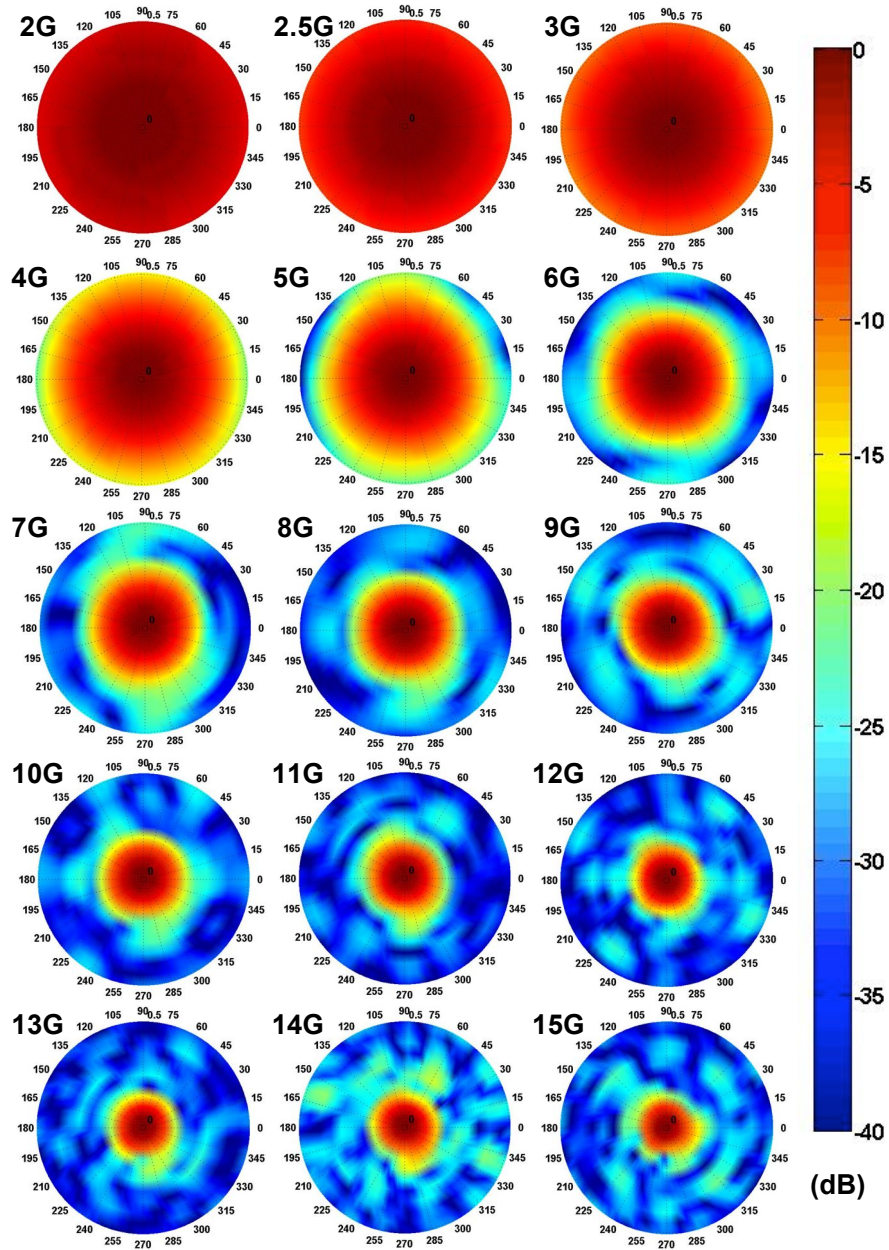


Figure 5.3.: The normalized co-polar far-field patterns of the total feed-reflector antenna system (Ludwig 3 co-polarized component), the range of θ is $0-0.5^\circ$ and ϕ is $0-360^\circ$.

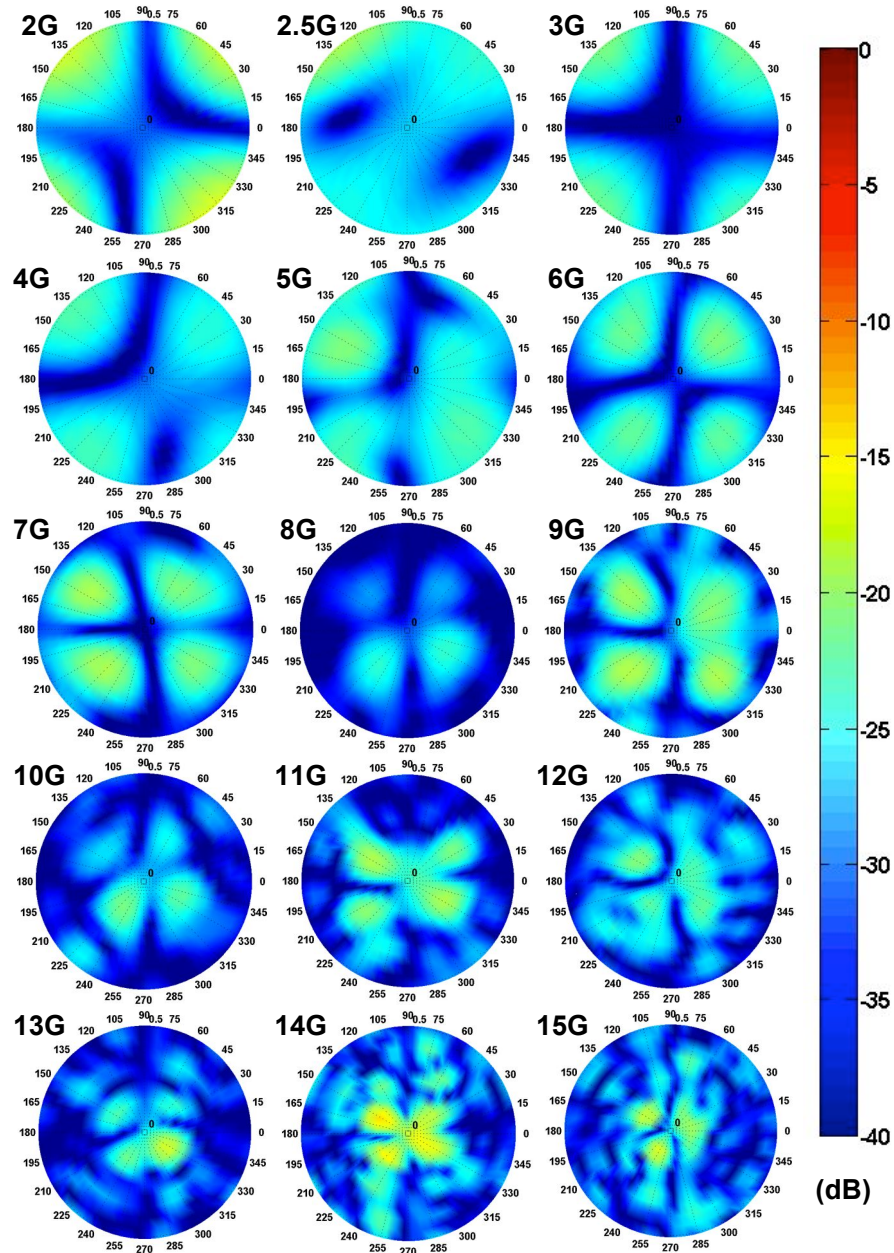


Figure 5.4.: The normalized cross-polar far-field patterns of the total feed-reflector antenna system (Ludwig 3 cross-polarized component), the range of θ is $0-0.5^\circ$ and ϕ is $0-360^\circ$; the asymmetry is related to the difference between the gains of the power combiners used to feed the antenna during measurements.

65° . The average XPL at HPBW over the frequency band of 2–15 GHz is about -20 dB for the illumination angles of $39\text{--}60^\circ$ (see Figure 5.8a).

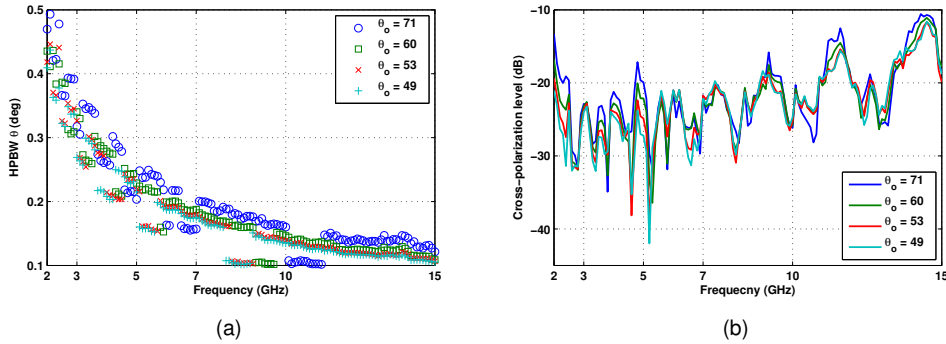


Figure 5.5.: (a) The half power beam width of the reflector antenna with the Eleven feed and (b) the relative cross-polarization level at HPBW levels as a function of frequency for various half illumination angles in $\phi = 45^\circ$ plane.

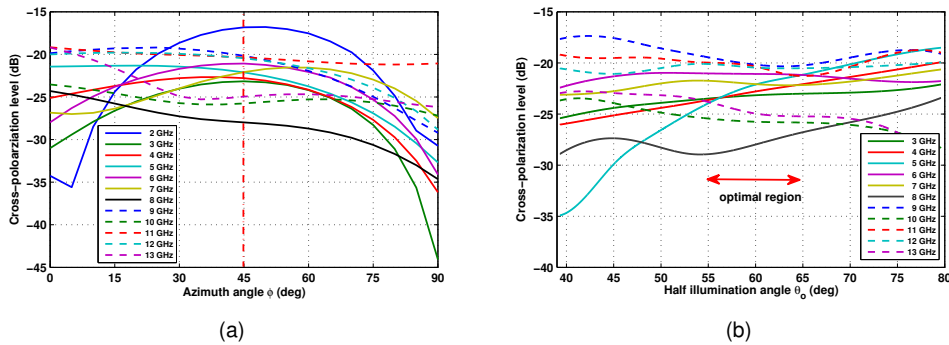


Figure 5.6.: The relative cross-polarization level at HPBW levels of the reflector antenna with the Eleven feed as (a) a function of the azimuth angle for half illumination angle of 60° ($F/D = 0.43$) and (b) a function of half illumination angle over frequency band of 2–12 GHz.

5.1.3. Aperture Efficiency and Side Lobe Level (SLL)

The definition of aperture efficiency is described in Section 2.2.

The side lobes of the far field radiation pattern represent unwanted radiation in undesired directions. The side lobe in the backward direction ($\theta = 180^\circ$) is referred to as *back lobe*. Side lobe level (SLL) is measured in decibels relative to the peak of main beam.

We applied equation (4.3.1) to compute the aperture efficiency from the directivity of simulated

far-field patterns and evaluated this parameter for a wide range of reflector illumination angles (40° – 80°), corresponding to $F/D = 0.3$ – 0.7 . To perform so, we altered the focal length of the reflector to adjust the illumination angle when the aperture diameter was unchanged.

As one can see in Figure 5.7b, the aperture efficiency is higher than -3 dB (50%) except for the frequencies below 2 GHz and around 11 GHz when the illumination angle is in the range of 39 – 63° . The first side lobe level is below -20 dB, especially over entire range of the illumination angles under consideration. The maxima of the aperture efficiency occur between 45° and 55° . In this range, the side lobe level is mostly below -25 dB for the frequency of 2–13 GHz except for 5 GHz (see Figure 5.7), i.e. F/D is 0.4–0.5. Figure 5.8 shows the average relative cross-polarization, first side lobe levels and aperture efficiency over the frequency band of 2–15 GHz as a function of half illumination angle in $\phi = 45^\circ$ plane. Table 5.1 summarized the antenna performance for the focal ratios $F/D = 0.43$ and 0.35 (half illumination angle is 60° and 71° .)

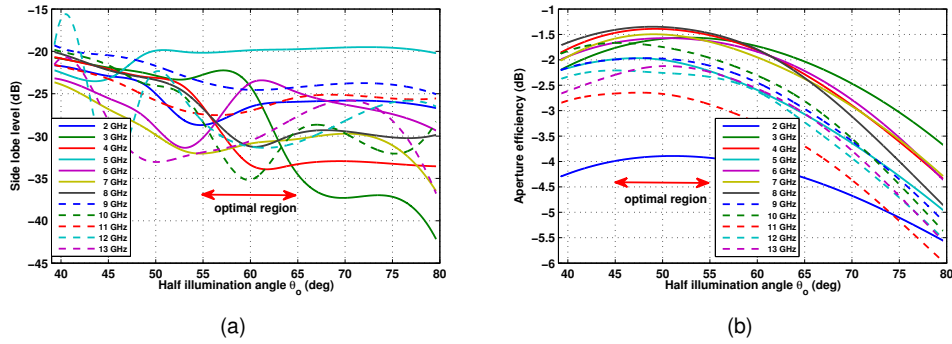


Figure 5.7.: (a) The first side lobe level in $\phi = 45^\circ$ plane and (b) the aperture efficiency as a function of half illumination angle of the reflector antenna fed with the Eleven feed for several frequencies.

5.1.4. System Noise Temperature and Sensitivity

Here, we present the results for the system noise temperature (and its contributions) and sensitivity (see definitions in Section 2.2). The noise temperature contribution due to the ground noise pick up T_{sp} was variable, and the receiver noise contribution T_{rec} due to lossy amplifier and antenna impedance mismatch was assumed to be constant and equals to 10 K, 20 K and 30 K. Note that the receiver noise temperature is relevant to cooled systems around 10–20 K [36], and to uncooled systems around 20–30 K or higher.

Figure 5.9 presents the simulation result for the prime-focus reflector system at 5.6 GHz, including the aperture efficiency and its spillover and illumination taper components, the system noise temperature ($T_{sys} = T_{sp} + T_{rec}$), the receiving sensitivity ($A_{eff}/T_{sys} = A_{ph}\eta_{ap}/(T_{rec} + T_{sp})$).

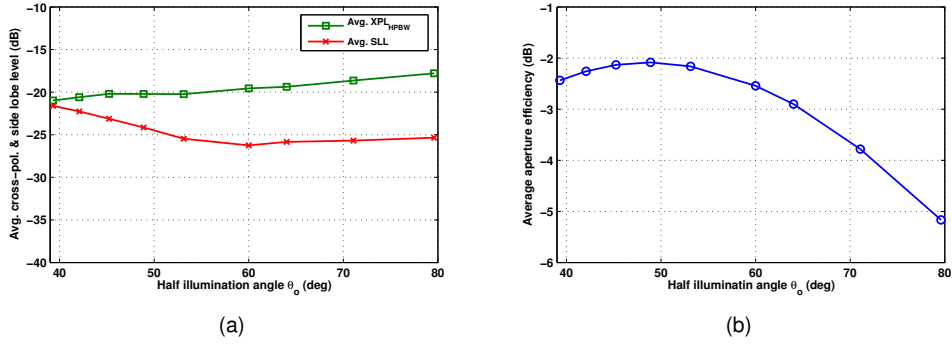


Figure 5.8.: The average (a) relative cross-polarization, first side lobe levels and (b) aperture efficiency of the reflector antenna with the Eleven feed over the frequency band of 2–15 GHz as a function of illumination half-angle in $\phi = 45^\circ$ plane.

Table 5.1.: The summary of the reflector antenna performance parameters in $\phi = 45^\circ$ plane for the focal ratio F/D of 0.43 and 0.35. (i.e., the half illumination angle is 60° and 71°).

F/D = 0.43	η_{ap} (dB)	HPBW (deg)	SLL _{1st} (dB)	XPL _{on-axis} (dB)	XPL _{HPBW} (dB)
3.0 GHz	-1.73	0.3404	-24.16	-19.22	-23.17
5.6 GHz	-1.88	0.2148	-30.44	-18.81	-22.57
9.0 GHz	-2.42	0.1044	-24.55	-18.33	-20.17
12.0 GHz	-2.62	0.1236	-31.25	-20.18	-20.46
F/D = 0.35	η_{ap} (dB)	HPBW (deg)	SLL _{1st} (dB)	XPL _{on-axis} (dB)	XPL _{HPBW} (dB)
3.0 GHz	-2.58	0.3174	-37.21	-19.49	-22.87
5.6 GHz	-3.06	0.2412	-42.28	-19.02	-21.42
9.0 GHz	-3.75	0.1690	-23.76	-18.42	-19.29
12.0 GHz	-4.09	0.1397	-27.62	-19.46	-20.38

The calculated sensitivity is based on the assumed constant receiver noise temperature T_{rec} of 10, 20 and 30 K with $F/D = 0.34$ – 0.5 . These results indicate the optimal F/D ratio of prime-focus reflector antenna that maximizes the system sensitivity is close to 0.4 for $T_{rec} = 20$ – 30 K and becomes smaller for lower temperature receivers. This is the result of the interplay between the spillover and receiver noise temperature contributions.

The noise temperature was evaluated for different antenna pointing evaluation angles, while the azimuth angle was set to a constant value of 0° . The elevation angle (El) is defined as the pointing angle up from the ground (horizon). $El = 90^\circ$ is the *zenith* pointing angle. Often in the reflector antenna and feed designs, the elevation angle is assumed to be constant and equal to 90° . However, it is critical to take into account the total range of angles El when operating the system.

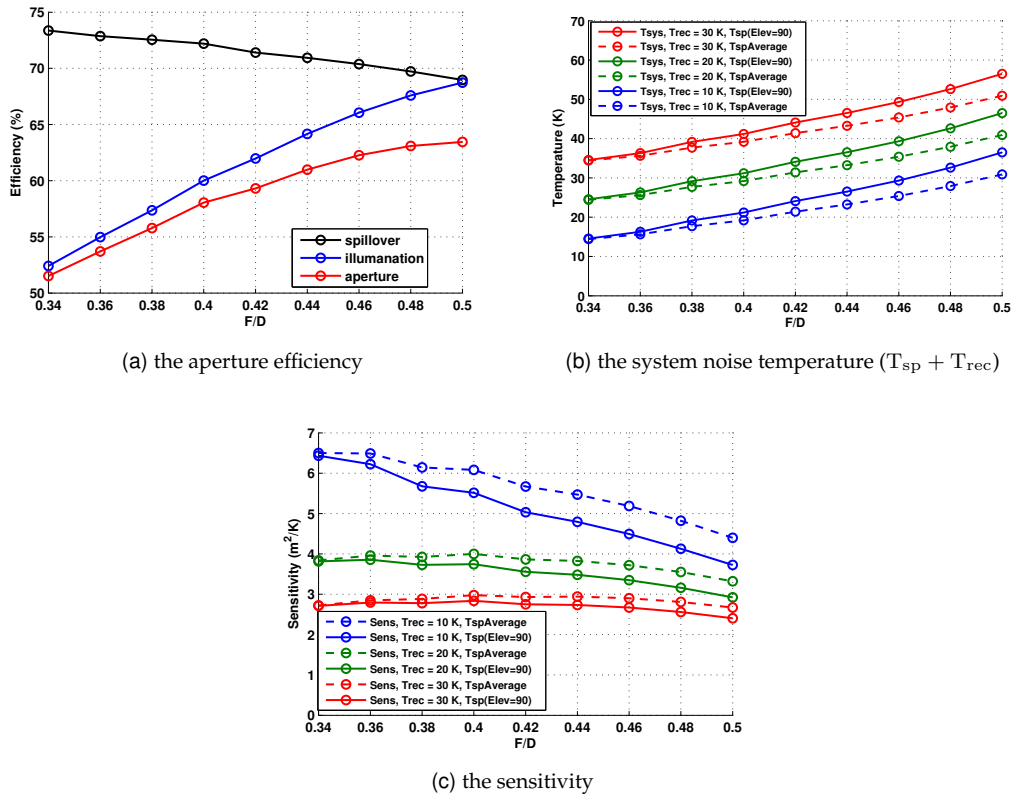


Figure 5.9.: The aperture efficiency, system noise temperature and sensitivity of the prime-focus reflector antenna as a function of F/D for $T_{rec} = 10, 20$ and 30 K at 5.6 GHz. The solid lines show the results obtained for elevation angles 90° , and the dotted lines are the averaged values of $T_{sys}/$ sensitivity over $El = 20$ – 170° .

5.1.5. Temporal Beam Stability

For high quality radio astronomical images the beam pattern of telescope must be stable over the duration of observation (typical twelve hours). However, it is in practice more difficult to achieve with multi-port antenna feeds such as the Eleven feed and phased array feeds [37, 38], as compared to conventional narrow band horns (that are in general single-port antennas). This complication originates from the fact that the beam of the multi-port antenna feed is formed by adding several signals received at individual antenna ports. For the case of the Eleven feed, this addition is realized by feeding combining network, which sums four signals received at the antenna ports; for the case of phased array feeds, it is done by active beamforming network, which realises the array element weighting. On the contrary, in one-horn-per-beam systems the beam shape is determined exclusively by the antenna geometry. In this way, possible gain variations due to the low noise amplifier connected to the antenna ports only change the directivity level, but not the beam shape [37, 38]. The beam shape of multi-port antenna feeds, in contrast, changes when the electronic gains of multiple amplifiers or the beamformer weighting coefficients vary in time. Therefore, these variations need to be accurately determined by calibration during observations and compensated for in the image construction process.

5.1.5.1. Analysis approach

Herein, we have analyzed the temporal beam stability of the Eleven feed due to gain variations of the four-to-one feeding combining network. Generally, the Eleven feed has eight output ports, but only four of them are used for a beam of each polarization. The beam port of the Eleven antenna is defined at the output of the feeding combining network (see reference plane $\Sigma 3$ in Figure 5.10). We defined the pattern F_{tot} as the combination of individual beams (F_n where $n = 1, \dots, 4$) formed at the four antenna ports (see reference plane $\Sigma 1$ in Figure 5.10):

$$F_{\text{tot}} = w_1 F_1 - w_2 F_2 + w_3 F_3 - w_4 F_4, \quad (5.1.2)$$

where w_1, w_2, w_3 and w_4 are weighting variables representing the gain variations of combiner channels. For an ideal four-to-one combiner with no gain drifts, $w_1 = w_2 = w_3 = w_4$, which implies the S-parameters of the combiner S_{51}, S_{52}, S_{53} and S_{54} are identical ($S_{51} = 1/\sqrt{4}$). In our study, we replaced the four-to-one combiner to the two sets of two-to-one identical combiners (see Figure 5.10(right)), where $S_{31} = S_{32}$. This reduced the original number of the variables to two (w_1, w_2). For the reduced system model,

$$F_{\text{tot}} = w_1 (F_1 - F_2) + w_2 (F_3 - F_4), \quad (5.1.3)$$

where F_{tot} is defined in reference plane $\Sigma 2$. We assumed $w_1 = 1$ (the $1/\sqrt{2}$ factor is omitted due to power combination). Therefore, w_2 is the only variable, a complex variable. We observed how

the radiated field changed when varying the amplitude or the phase of weighting coefficient w_2 ($w_2 = 1$ for ideal cases).

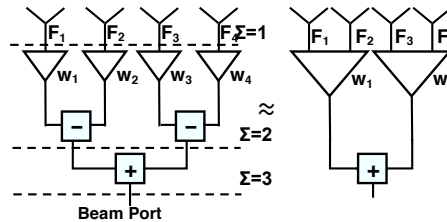


Figure 5.10.: The feeding network of the Eleven antenna with four single terminals per polarization and its equivalent simplified case with two differential terminals (two petals).

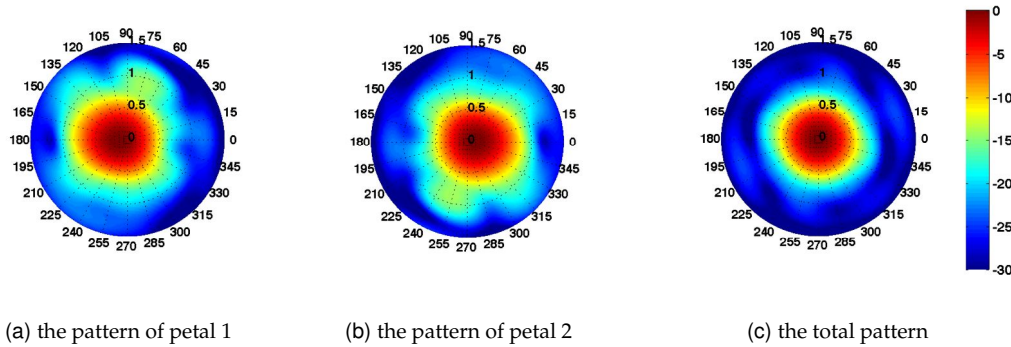
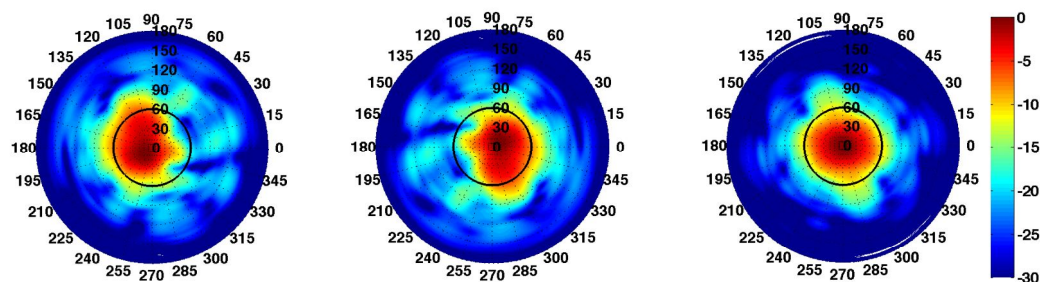


Figure 5.11.: The normalized power patterns of the reflector system at 3 GHz, as defined in reference plane $\Sigma 2$ after combining the signals received at (a) port 1 and port 2, (b) port 3 and port 4; and in reference plane $\Sigma 3$ (c) at the beam port (see Figure 5.10) based on the simulated pattern. The range of θ is $0-1.5^\circ$.

The total antenna pattern is the combination of the patterns at the ports of antenna pedals (see reference plane $\Sigma 2$)—two ports of the Eleven feed.

Results

Figures 5.11a–b show the patterns defined in reference plane $\Sigma 2$, combining the signals received at port 1, port 2 and port 3, port 4. Note that these patterns are the secondary field patterns of the reflector systems, based on the simulated Eleven feed patterns. Figure 5.11c shows the result of the addition of the two asymmetric patterns, which forms the required shape of the reflector illumination pattern. These patterns were computed for the case of no gain variation ($w_1 = w_2$). The normalized primary field power patterns (Eleven feed patterns) in reference plane $\Sigma 2$ and $\Sigma 3$ are shown in Figure 5.12.



(a) the pattern of petal 1 (b) the pattern of petal 2 (c) the total pattern

Figure 5.12.: The normalized feed power patterns at 3 GHz, as defined in the reference plane Σ_2 after combining the signals received at (a) port 1 and port 2, (b) port 3 and port 4; and in reference plane Σ_3 (c) at the beam port (see Figure 5.10), based on the simulated pattern. The range of θ is $0-180^\circ$.

The above results represent the reference ideal case ($w_2 = 1$). Herein, we changed the amplitude or/and the phase of w (see Figure 5.10(right)) to evaluate the variation of the aperture efficiency, on-axis beam directivity and directivity at half power beam width. The calculation of directivity and beam shape variation of the normalized feed patterns was done as as the following:

$$\frac{D_0(\theta = 0, |\Delta w| = var.)}{D_0(\theta = 0, |\Delta w| = 0)} \quad (5.1.4)$$

$$\frac{D_0(\theta = 0, \Delta\phi = var.)}{D_0(\theta = 0, \Delta\phi = 0)}, \quad (5.1.5)$$

$$\frac{D_{HPBW}(\theta = HPBW, |\Delta w| = var.)}{D_{HPBW}(\theta = HPBW, |\Delta w| = 0)}, \quad (5.1.6)$$

$$\frac{D_{HPBW}(\theta = HPBW, \Delta\phi = var.)}{D_{HPBW}(\theta = HPBW, \Delta\phi = 0)}. \quad (5.1.7)$$

The evaluation range is $|\Delta w| \leq 0.5$ dB and $\Delta\phi \leq 10^\circ$. The results in Figure 5.13 show that the phase drift is the dominant factor of the beam variation, while the variation in amplitude has a smaller effect on the shape of the pattern. When changing both the amplitude and phase of the gains of the feeding combining network, the effect of these variations is almost identical to that of solely changing the phase factor (see Figure 5.14). We evaluated the effect of the gain variations on the axis and at HPBW level of the main lobe as a function of frequency. This was done by changing the amplitude or/and the phase of the gains of feeding combiner, in which the variations in amplitude and phase were $|\Delta w| = 0.5$ dB and $\angle\Delta w = 10^\circ$.

One can observe in Figure 5.13 that the directivity of the total (combined) pattern at the beam port varies (decreases) when altering the weighting coefficients (in amplitude or in phase) of the combining network. This variation is more significant in the directions of the beam HPBW, rather than on-axis. Nonetheless, the relative change with respect to the reference beam, formed

by the ideal combiner, is rather small and does not exceed 0.5%. when $|\Delta w| < 0.5$ dB and $\angle\Delta w < 10^\circ$. These are typical values for the state-of-art microwave component of the considered frequencies from 2 to 8 GHz (see Figure 5.14).

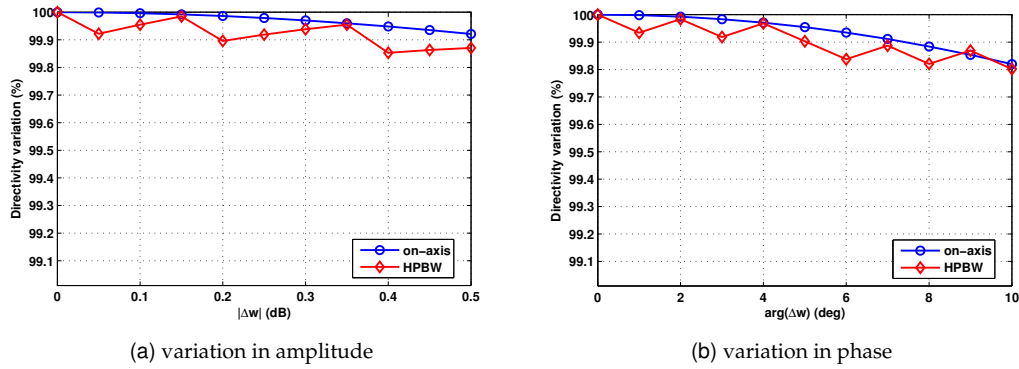


Figure 5.13.: The directivity variation on axis and in the direction of the beam HPBW of the reflector antenna fed with the Eleven feed as a function variation (a) in amplitude $|\Delta w|$ and (b) in phase $\angle\Delta w$ of the weighting coefficients (see Figure 5.10) at 3.8 GHz.

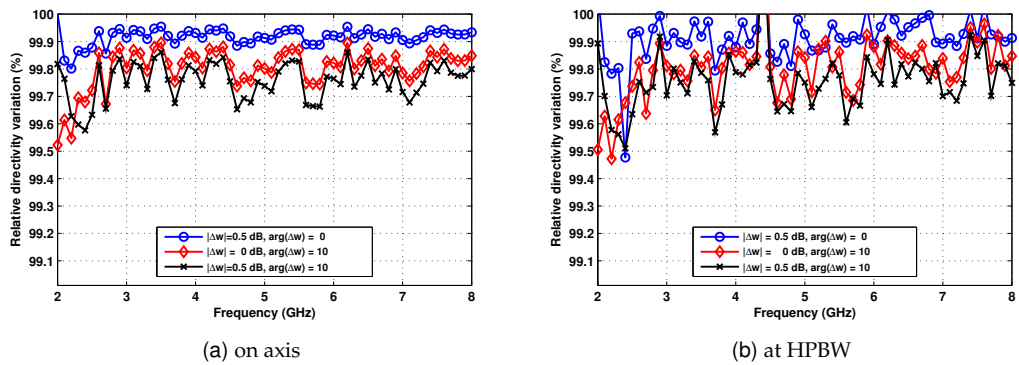


Figure 5.14.: The directivity variation (a) on axis and (b) at beam HPBW of the reflector antenna fed with the Eleven feed as a function of frequency.

Analysis of the Reflector Antenna System Including Strut and Feed Blockage Effects

THE aim of this chapter is to investigate the performance of the reflector antenna system fed with the Eleven antenna feed, including the effects of the feed supporting structure (the feed cabin and struts), and to compare this performance to that of the system with the octave horn feed.

The blockage effects caused by the structures in axi-symmetric reflector systems are known to reduce the antenna efficiency and significantly increase the spillover noise as well as the side lobe and cross-polarization levels [39]. In turn, these effects will cause the loss of the sensitivity of telescopes and increase the complexity of beam calibration on the sky; the latter is mainly due to struts, which cause characteristic high side lobes rotating in the sky as the Earth rotates during observations.

Herein, a detailed numerical study of the blockage effects in axi-symmetric reflector antennas such as being proposed for the SKA dish design in [7] is presented. This study argues that for such systems supporting multiple receivers will not be as difficult as for conventional telescopes owing to more advanced technologies of strut design (available now) and optimal choice of wideband feeds. When a set of a few 2–3-octave feeds is used instead of a collection of multiple single-octave horn feeds system, the overall size of the feed cabin will not be very large. The

numerical results will be shown for the antenna with the ultra wideband Eleven feed [16] operating from 500 MHz to 8 GHz. (We assume that his system consists of two 4:1 bandwidth feeds, covering 0.5–2 GHz and 2–8 GHz bands.) This feed system represents a compact structure with the aperture area of 660 mm × 660 mm × 210 mm (as determined by the lowest frequency) that can be supported with relatively thin struts. The evaluation of the antenna with four circular struts has been performed by using the canonical PO approach realized in TICRA's GRASP software [31, p.195].

The performance parameters have been evaluated for different strut positions. The position of the strut was defined by the start and end points connecting it to the feed box and reflector (see Figure 6.1). The start point was fixed and the end point was varied. This variation - measured by the distance from the reflector axis D_o - was used here as the strut position parameter. We have considered D_o values ranging from 3–8 meters, where D_o of 7.5 meters corresponds to the end point is attached to the rim of the reflector. The diameter of struts' cross-section was set to 80 mm [40]. Such thin struts can be manufactured using advanced materials which can be stiff and compact at the same time [7].

Reflector System: The evaluated reflector system is a axi-symmetric single reflector system fed with the Eleven antenna located at the focal point of the paraboloid, of which the aperture diameter is 15 meter and the focal ratio F/D is 0.42. For observation purpose, the simulations are based on the measured far-field pattern of the Eleven antenna at 5.6 GHz of the reflector antenna. The feed pattern was left unchanged during the simulations over the frequency band in order to separate the frequency dependent effects associated with the reflector and its blocking structure from the effects attributed to specific feed design.

Struts: The feed is supported by four cylindrical struts which are defined by the position of the end points in rectangular coordinate system and the radius. Figure 6.1 shows the strut geometry and position. Table 6.1 shows the examples of strut positions. The radii in this study are 40 mm or 80 mm.

6.1. The Modeling Procedure and Simulation Methods of the Blockage Effects in GRASP

The performance of reflector antenna system including the feed supporting structure is analyzed here as a combined effect of *strut blockage* and *central blockage* due to feed itself. The strut blockage is modeled by considering the scattering of spherical and plane waves: the first phe-

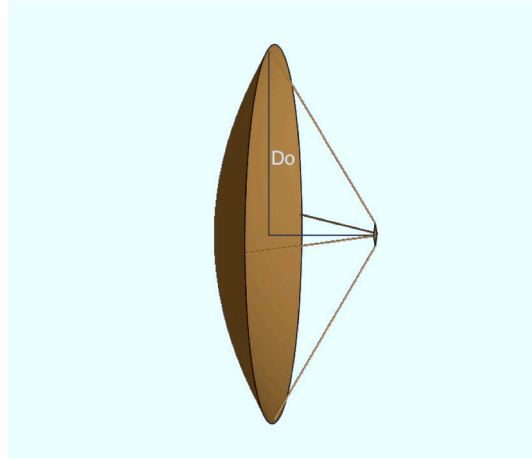


Figure 6.1.: The geometry of the axi-symmetric reflector antenna with four circular struts, showing the strut position as defined by parameter D_o that was used as the variable in the present study. Table 6.1 shows the relation between the values of D_o and the coordinates of the end and start points of struts, used to specify their positions in GRASP 9.

Table 6.1.: Examples of circular struts' positions as defined in the GRASP software. The coordinates of the end and start points of struts are used to specify the strut position, which can be directly related to the design parameter D_o (see Figure 6.1.) The coordinates are shown for one strut only, since the other three struts are located symmetrically with respect to the reflector axis.

Strut position (x,y,z) [m,m,m]	D_o [m]
(0.33,0.33.0) → (3.8,3.8,5.1)	5.37
(0.33,0.33.0) → (4.2,4.2,4.8)	5.94
(0.33,0.33.0) → (4.4,4.4,4.7)	6.22
(0.33,0.33.0) → (4.6,4.6,4.6)	6.51
(0.33,0.33.0) → (4.8,4.8,4.4)	6.79
(0.33,0.33.0) → (5.2,5.2,4.1)	7.35
(0.33,0.33.0) → (6.0,6.0,4.5)	8.49

nomena occurs when the struts are illuminated by the primary incident field of the feed; and the second is when the plane wave scattered from the reflector illuminates the struts.

6.1.1. Strut Blockage

The effect of strut blockage is computed by *spherical-wave blockage* and *plane-wave blockage* (see Figure 4.2 and refer to Section 4.2.3). The strut will block the field coming from the feed, an effect often referred to as the spherical-wave strut scattering since the field from the feed is approximately a spherical wave. To analyze this effect we will need to calculate induced currents on the struts by using the feed as source. This step is followed by calculating the currents on the main dish with the strut currents as source.

The other strut scattering mechanism is often referred to as the plane-wave scattering component of the strut blockage since it blocks the predominant field coming from the reflector. The induced current on the reflector are first calculated and then used to generate currents on the strut.

Two types of analysis methods for circular struts are realized in GRASP 9:

1. a *simple PO approach* which is commonly used for struts which are thick relative to the wavelength
2. a *canonical solution* for struts with diameters in the order of the wavelength.

An accurate prediction of the effects of the struts both on the main lobe and on the side lobes can be achieved by taking the current distribution along the circumference of the strut into account. This is relatively simple for a circular strut because the canonical problem (plane wave incidence on an infinite circular cylinder) has a simple solution in series form. For thick struts the current distribution can alternatively be found by the simple PO approximation. The accuracy of the simple PO solution increases with increasing diameter of struts because the amplitude of the generated current on the shadow side is decreasing. The strut is illuminated by both a dipole and a plane wave, and the scattered fields are calculated with the simple PO as well as the canonical solution. The results are presented on Figure 6.2.

The result on Figure 6.2 indicates that for struts thicker than 3 wavelengths the simple PO approach is sufficient for most practical applications, both for plane wave and spherical wave incidence.

In this study the struts' diameter (80 mm) are in the order of the wavelength (40–600 mm as frequency ranges from 500 MHz to 8 GHz), in which the diameter is in the range of 0.1 – 2.0λ , therefore canonical solution is required in order to obtain sufficiently accurate results.

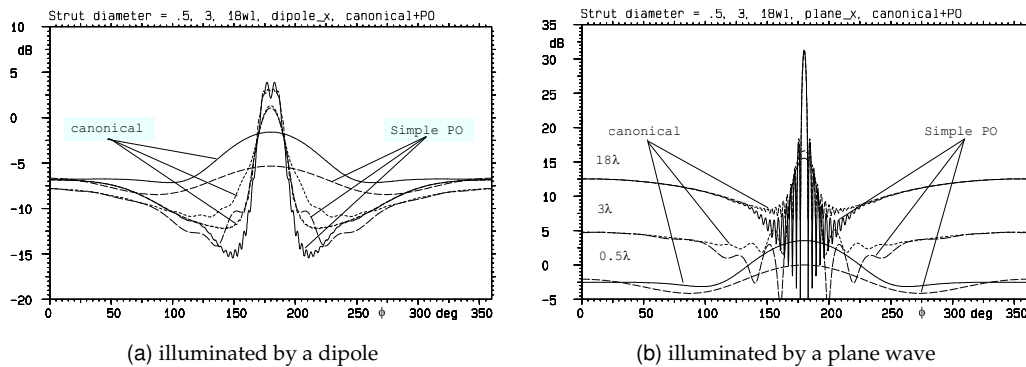


Figure 6.2.: Far fields from circular strut, $D = 0.5\lambda, 3\lambda, 18\lambda$, illuminated by a dipole (*left*) and a plane wave (*right*) and calculated by the canonical and the simple PO solution [31, p.202–203].

6.1.2. Central Blockage Effects due to the Feed

In a prime-focus reflector system, the feed will obstruct the scattered field from the main reflector and reduce the gain of the antenna in the direction of the main lobe, as well as increase the levels of the side lobes. There are two approaches in GRASP 9 to model this effect:

1. The first approach is based on the so-called *null-field assumption* and consists on nulling out those current on the main reflector which are inside the optical shadow of the sub on the main when seen from the boresight direction. This approach provides a very good estimate of the gain reduction, but it is less accurate when it comes to the effect of the blockage on the side lobes.
2. The other method is much more rigorous, called *Rigorous Solution* in this study, and attempts to model the actual scattering from the blocking object. This object is in general of a cubic form (the shape of the feed box), but for the case of the boresight incidence it can be reduced to the equivalent conducting plate having a physical area which equals to the blockage area). The induced currents on the main reflector are used to illuminate the conducting square plate, which has the same area as the area of feed aperture, and generate a new set of induced currents on the reflector. By adding the fields from these currents to the field which was calculated in the previous paragraph one account for the blockage as well as the scattering into the side-lobe region.

Figure 6.3 illustrates how the rays propagate when considering the two approaches of modeling central blockage due to feed itself. Note in Figure 6.3(a) how the rays actually proceed through the central hole when drawn in GRASP 9. Figure 6.4 shows a comparison between the two methods: the null-field assumption and the rigorous solution. The simulated antenna pattern is shown when the blockage is neglected and when it is taken into account by the considered

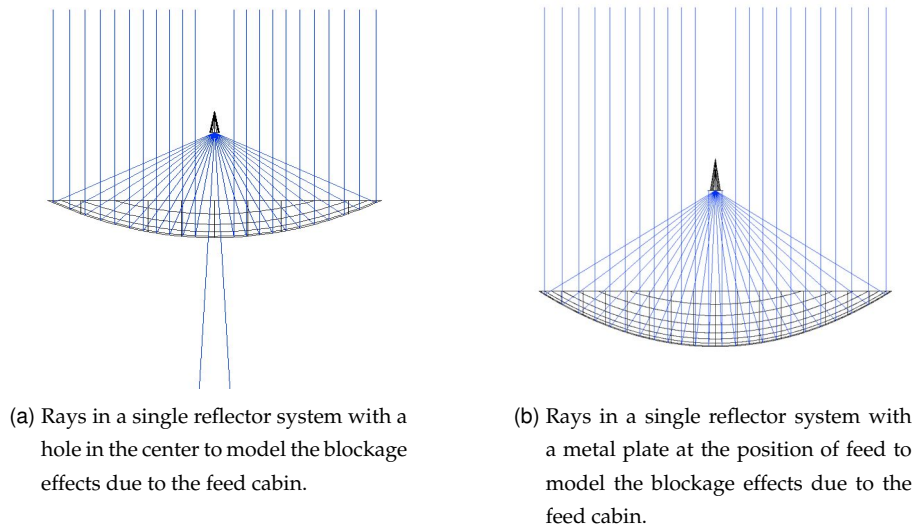


Figure 6.3.: The diagram of two approaches of modeling the central feed blockage: (a) the null-field assumption and (b) the canonical PO (rigorous) solution.

methods. It is seen that these patterns agree very well on the region of the main lobe and first side lobe. Consequently, if this is the only region of interest, then the null-field approach should be selected, since this is by far the computationally most efficient method. On the other hand, in case the precise structure of the outer side lobes or/and an accurate evaluation of the spillover noise contribution are of interest then one is confined to the rigorous method which will give a more accurate prediction of the scattered field in these directions.

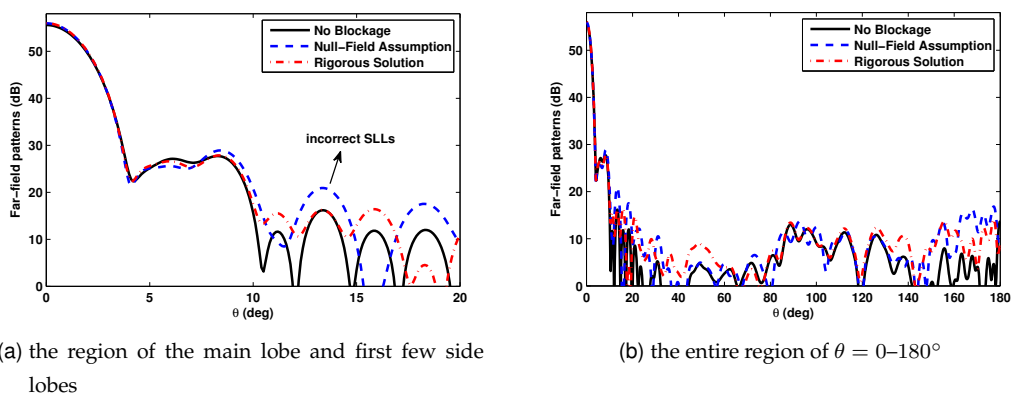


Figure 6.4.: Far-field pattern cuts ($\phi = 0^\circ$) of the axi-symmetric antenna fed with the Eleven feed at 500 MHz. The patterns have been computed for the case of unblocked and feed-blocked apertures, as obtained with the two methods, as implemented in GRASP 9.

The far field of the axi-symmetric reflector of the 15-m aperture diameter fed with the Eleven antenna is modeled first and used as the reference case representing the unblocked aperture. In order to observe the effect associated to the supporting structure of struts, the scattered fields are calculated, simulated by considering both plane-wave and spherical-wave scattering, and then added to the far field for the reflector with the unblocked aperture. Then the rigorous solution for the analysis of the central blockage is used to compute the field of the antenna blocked by the feed structure. This field is added to the field of the reflector+struts system to obtain the combined solution. The simulation procedure of GRASP command list is in Appendix B.

6.2. Discretization of the Reflector Antenna Far-Field Pattern

The sampling (or discretization) of antenna far field in angular directions represents an important factor affecting the accuracy of the evaluated antenna parameters. High accuracy requires very fine discretization (a large number of sampling points) and consequently a long computing time. Therefore, the first step in the analysis of blockage effect is to find out the optimal sampling factor (in theta and phi directions) that will lead to accurate values of the key performance parameter, including the side-lobe and cross-polarization levels, and the ground noise pick up, with acceptable simulation time.

The study of required sampling discretization step is carried out for both θ and ϕ directions to determine the optimal values of $\Delta\theta$ and $\Delta\phi$. The discretization steps have been varied in the range of $0.025^\circ < \Delta\theta < 1^\circ$ and $1^\circ < \Delta\phi < 10^\circ$, and the values of considered antenna parameters have been computed for various combination of $\Delta\theta$ and $\Delta\phi$.

Discretization in ϕ -plane: Figure 6.5 shows the far-field pattern of the reflector antenna with the aperture diameter of 15 meter which is fed with the Eleven antenna for various discretization steps $\Delta\theta$. These patterns are calculated by accounting for both blockage effects due to struts and feed itself. The discretization step $\Delta\phi$ varies from 1–10° while $\Delta\theta$ is constant and equals to 0.05°. This result indicates that the pattern computed for $\Delta\phi > 2.5^\circ$ is much coarser than that of the finer discretization. Since the far field function does not rapidly change in ϕ direction, the key performance parameters have almost identical values over the considered range of $\Delta\phi$. This rather constant behavior can be observed in Figure 6.6, presenting the ground noise pick-up, sidelobe levels, and cross-polarization levels at 1 GHz. Note that the values of the antenna performance for the considered discretization almost remain constants. Nonetheless, the evaluation of antenna performance becomes less accurate when the polar discretization step $\Delta\theta$ is too large.

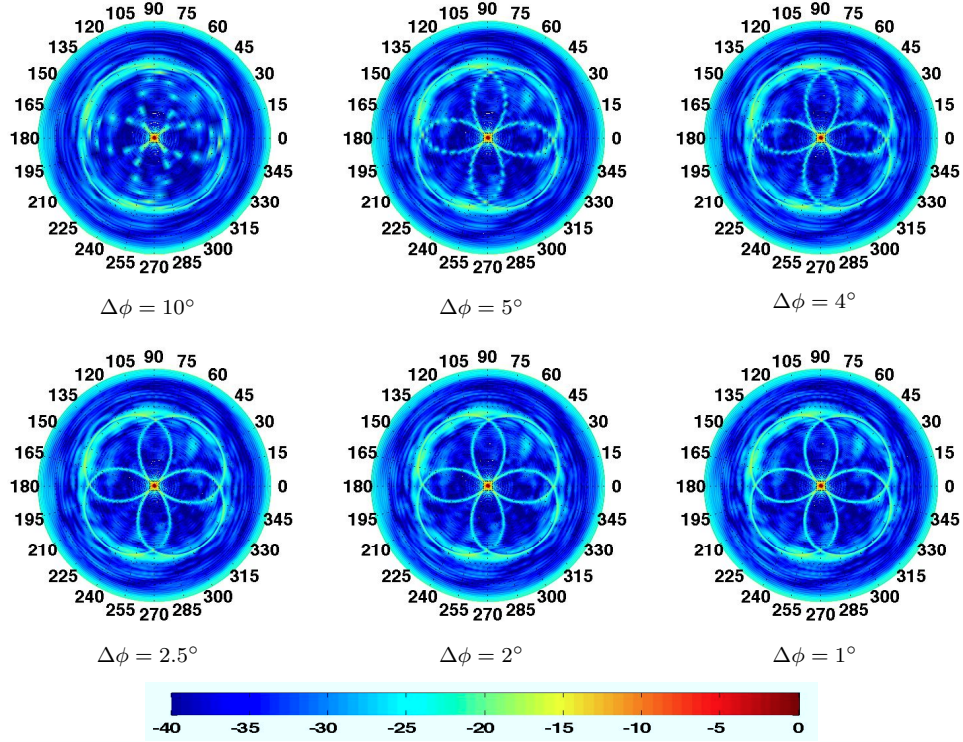


Figure 6.5.: Normalized co-polar far-field patterns of the reflector antenna system with the Eleven feed (for the strut placement parameter $D_o = 6.5$ m and $w_{st} = 80$ mm) for different discretization $\Delta\phi$ as $\Delta\theta = 0.05^\circ$ at 1 GHz ($\theta = 0-180^\circ$).

Discretization in θ -plane: The far-field patterns of the same reflector system for the discretization step of $\Delta\theta$ varying from $0.05-1^\circ$ and $\Delta\phi = 2^\circ$ at 1 GHz are shown in Figure 6.7. This result clearly demonstrates that the far-field patterns depend on $\Delta\theta$ and particularly the side and back lobes can be sampled finer by reducing $\Delta\theta$, and the shape of patterns virtually does not change as $\Delta\theta < 0.2^\circ$.

Since the side lobe beamwidth and the far-field patterns depend on the frequency, the required discretization step $\Delta\theta$ should be smaller and smaller as frequency increases. The following study aims to find out the required discretization step for different frequencies and observe the effect of varying $\Delta\theta$ on performance parameters such as ground noise pick-up, side-lobe level, and cross-polarization level, shown in Figure 6.8. As expected, the simulations at high frequency needs finer discretization step $\Delta\theta$ than that at low frequency. Table 6.2 summarizes the values of the narrowest side-lobe beamwidth and the required discretization step $\Delta\theta$ for the key performance parameters at different frequencies. As one can see, the discretization step must be about four times smaller than side-lobe beamwidth, defined as the distance between the nulls, so as to obtain a good accuracy.

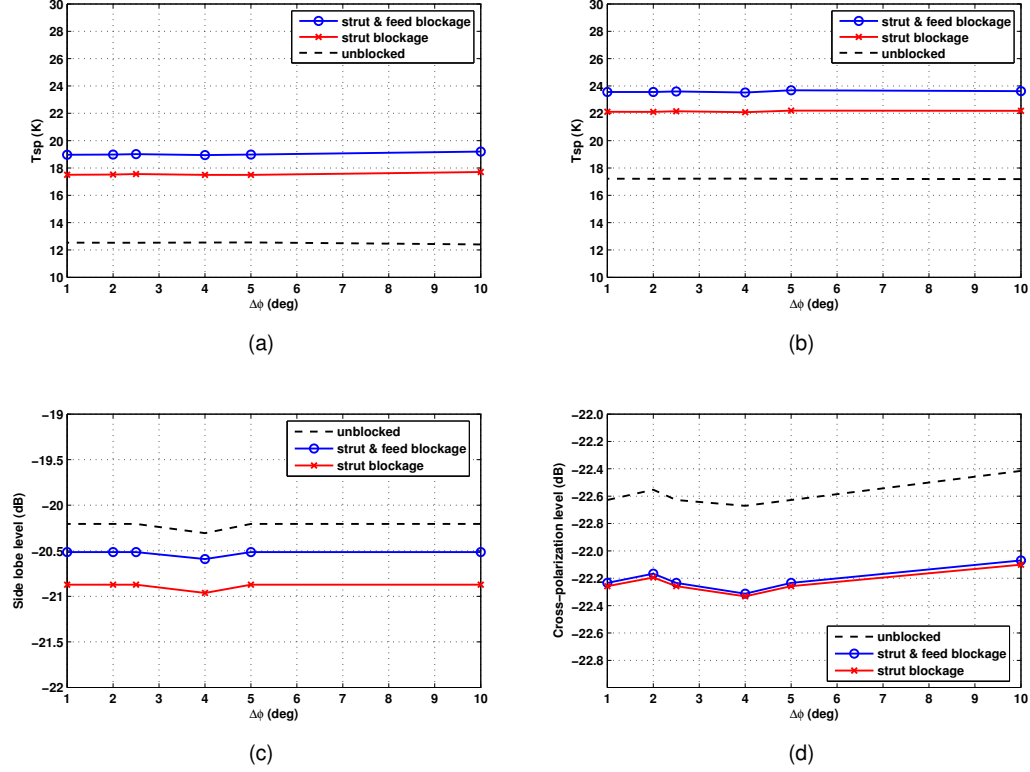
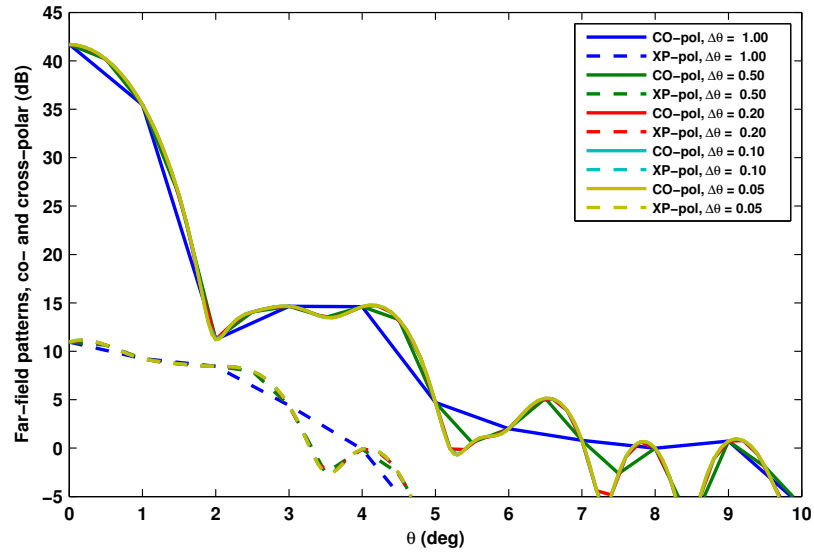


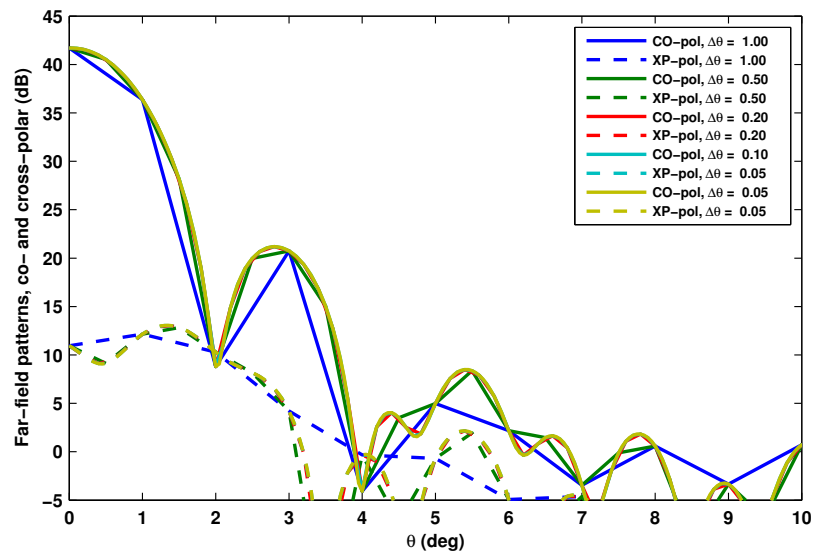
Figure 6.6.: The spillover noise temperature at (a) $El = 45^\circ$ and (b) $El = 90^\circ$, (c) the 1st side-lobe levels, (d) the cross-polarization levels in $\phi = 45^\circ$ plane ($\phi = 45^\circ$) at the HPBW level of the reflector antenna system with the Eleven feed including the effects of struts and central blockage for different discretization steps $\Delta\phi$ as $\Delta\theta = 0.05^\circ$ at 1 GHz.

Table 6.2.: The required discretization step $\Delta\theta$ for the key performance parameters at different frequencies.

	0.5 GHz	1.0 GHz	1.4 GHz	2.0 GHz	4.0 GHz	8.0 GHz
Cross-pol. Level	0.5°	0.1°	0.1°	0.1°	0.05°	0.25°
HPBW of the Main Lobe	1.4°	0.7°	0.5°	0.35°	0.18°	0.09°
Spillover Noise Temp.	0.5°	0.2°	0.2°	0.2°	0.1°	0.05°
Side-lobe Beamwidth	2.6°	1°	1°	0.6°	0.3°	0.1°
Side-lobe Level	0.2°	0.2°	0.5°	0.2°	0.1°	0.05°



(a) E-field



(b) H-field

Figure 6.7.: Far-field patterns of the axi-symmetric reflector fed with the Eleven antenna including the effects of struts and central blockage for different discretization steps $\Delta\theta$ and $\Delta\phi = 2^\circ$ at 1 GHz.

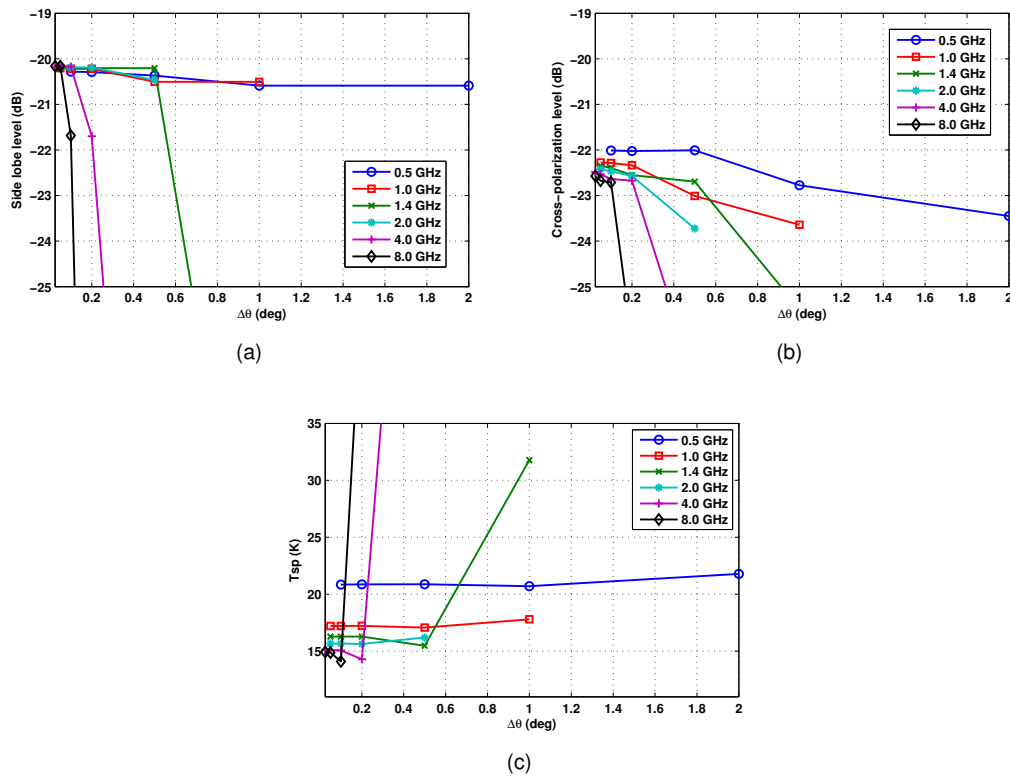


Figure 6.8.: (a) The 1st side-lobe levels, (b) the relative cross-polarization levels in $\phi = 45^\circ$ plane ($\phi = 45^\circ$) at the HPBW level, and (c) the spillover noise temperature ($EI = 45^\circ$) of the reflector antenna system with the Eleven feed including the effects of struts and central blockage at different frequencies, in which the discretization step $\Delta\theta$ varies from 0.025° to 2° and $\Delta\phi = 2^\circ$.

6.3. Determination of the Optimal Placement of Struts

The simulation results for the reflector fed with the Eleven feed and the horn feed are discussed in this subsection in the frequency range of 0.5–8 GHz. The antenna performance parameters are evaluated as a function of parameter D_o , used to define the strut position (see Figure 6.1). In order to understand the effect of the strut width, we evaluated the system performance for two cross-section diameters, 80 mm and 180 mm, for the horn feed as an example.

6.3.1. The Eleven Antenna Feed

The normalized co- and cross-polar far-field patterns for the Eleven feed based on the measurement data at 5.6 GHz are shown in Figure 6.9. The side lobe level, cross-polarization level, blockage efficiency, and aperture efficiency for the reflector antenna fed with the Eleven feed supported by four struts as a function of parameter D_o are presented in Figure 6.10. These results demonstrate that:

- The antenna efficiency is significantly affected by the blockage provided by the feed and struts when the struts are located in the inner region of the reflector's aperture. The overall blockage efficiency for this case can be as low as 84% at 500 MHz, whereas when struts are positioned closer to the reflector's rim, it approaches 95% and becomes less dependent on frequency.
- The relative cross-polarization level can be reduced up to 2.5 dB by controlling the strut placement. The degradation w.r.t the unblocked aperture is < 0.2 dB when the struts are placed at the optimal position $D_o = 6.5$ m. For $D_o = 6.5$ –8.5 m, the cross-polarization level almost remains constant over the frequency band.
- The effects of the strut and feed blockage on side lobes near the main lobe are negligible, but for the far side and back radiation zone these become visible (see Figure 6.17). The latter have an effect on T_{sp} , which is discussed next.

Figure 6.11 presents the antenna noise temperature due to the ground thermal noise pick up and the overall system sensitivity for the assumed constant receiver noise temperature of 20 K. We can observe that:

- The antenna noise contribution is strongly dependent on the position of struts, and there exists a minimum of $T_{sp}(D_o)$ function. This minimum also depends on the antenna pointing direction, i.e. typically within the range of 20° – 170° elevation angles. Since, radio telescopes are pointed most of the observation time at the elevation angle close to $El = 45^\circ$, we use this direction to determine the optimal placement of the struts. At $El = 45^\circ$, at

most frequencies the minimum happens for $D_o \sim 6.5$ m that provides the optimal range of scattering angles for the antenna fields.

- The design of strut positions with minimum $T_{s,p}$ provides the maximum sensitivity since the aperture efficiency is weekly dependent on D_o , as long as the struts are close to the rim of the reflector (see Figure 6.11). This maximum is more pronounced for the low and high elevation angles. The sensitivity is weakly dependent on D_o as long as the strut is positioned close to the rim of the reflector when $El = 90^\circ$.

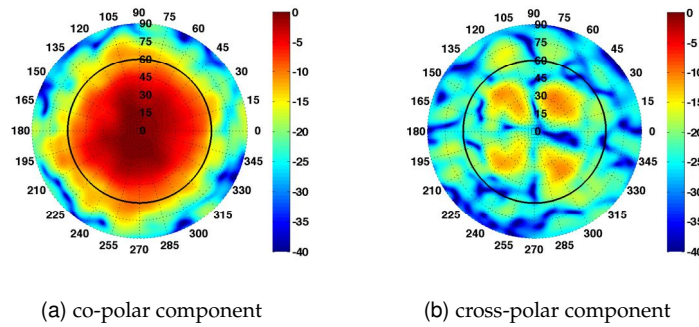


Figure 6.9.: The normalized co- and cross-polarized component patterns of the Eleven antenna based on the measurement data [16] at 5.6 GHz ($\theta = 0-90^\circ$) in logarithmic scale.

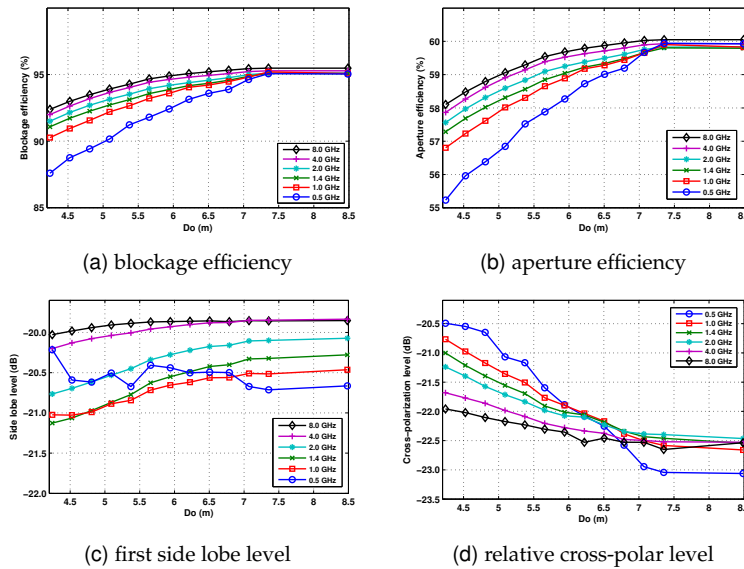


Figure 6.10.: Parameters of the reflector antenna fed with the Eleven feed supported by four struts: (a) the aperture efficiency reduction, (b) the aperture efficiency, (c) the maximum first side lobe level, and (d) the relative cross-polarization level at HPBW level ($\phi = 45^\circ$) at different frequencies versus the strut position parameter D_o .

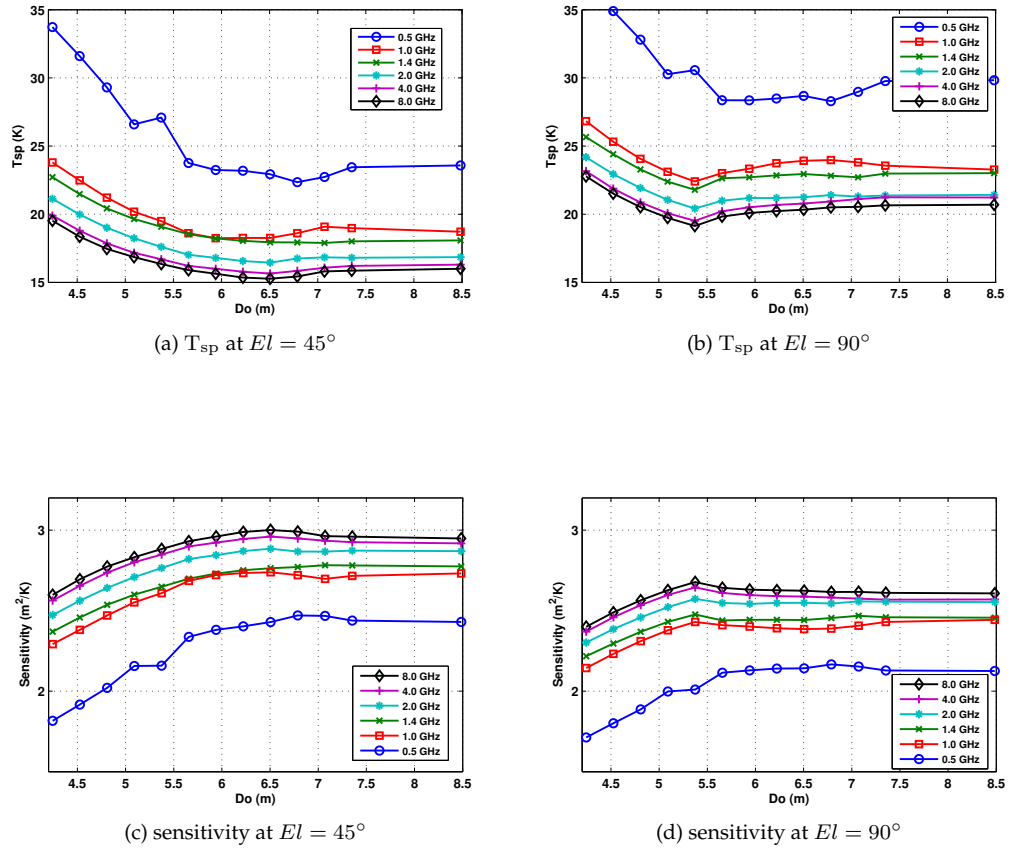


Figure 6.11.: Parameters of the reflector antenna fed with the Eleven feed supported by four struts: (a)–(b) The spillover noise temperature and (c)–(d) the sensitivity as $T_{rec} = 20$ K at $El = 45^\circ$ and $El = 90^\circ$ due to the ground thermal noise ($T_{ground} = 300$ K) as $T_{rec} = 20$ K at different frequencies versus the strut position parameter D_o .

6.3.2. The Horn Feed

We performed a similar analysis of the antenna performance for the reflector system fed with the horn feed. The results are shown for the strut cross-section $w_{st} = 80$ mm as in Section 6.3.1 and also for $w_{st} = 160$ mm. Figure 6.12 shows the normalized co- and cross-polar far-field patterns of the horn feed which was simulated by Oleg Iupikov, using CST Microwave Studio [41] and the design procedure in [42]. The results of the antenna performances are shown in Figure 6.13–6.14. One can observe that

- The struts of $w_{st} = 160$ mm cause lower aperture efficiency and higher T_{sys} than that of the same system with $w_{st} = 80$ mm. In particular, the blockage efficiency drops with 4% when the diameter is twice wider, and T_{sys} relative increase is up to 10 K. This causes the sensitivity reduction of 17%.
- The side-lobe and cross-polarization levels are higher when the struts are wider. These performance parameters become more sensitive to the change of the frequency and strut position; however, the values of the side lobe and cross-polarization levels are still below -29 dB and -37 dB when the struts position is optimal.
- The comparative analysis of the results for the considered feeds and strut geometry shows that the optimal placement of the strut (for minimum T_{sp}) is weakly dependent on the type of feed and the strut width, whereas the shape of reflector (F/D) is the determinant factor. However, when the strut cross-section area increases, the range of the optimal values of D_o becomes narrower (compare Figure 6.13 and 6.14 on the left and right). Therefore, in practice the optimized design of such a reflector systems (reflector + struts) will be likely more sensitive to the manufacturing tolerances, and the reflector/strut deformations due to weather conditions.
- In comparison with the unblocked aperture, the relative increase of T_{sys} and sensitivity are 7–10 K and 20–25% for the optimal strut placement ($D_o = 6.5$ m) and $w_s = 80$ mm.

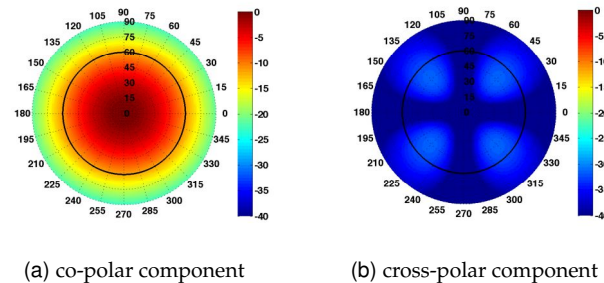


Figure 6.12.: The normalized co- and cross-polarized component patterns of the horn feed, simulated by CST Microwave Studio [41] and using the design procedure in [42]. The patterns are in logarithmic scale.

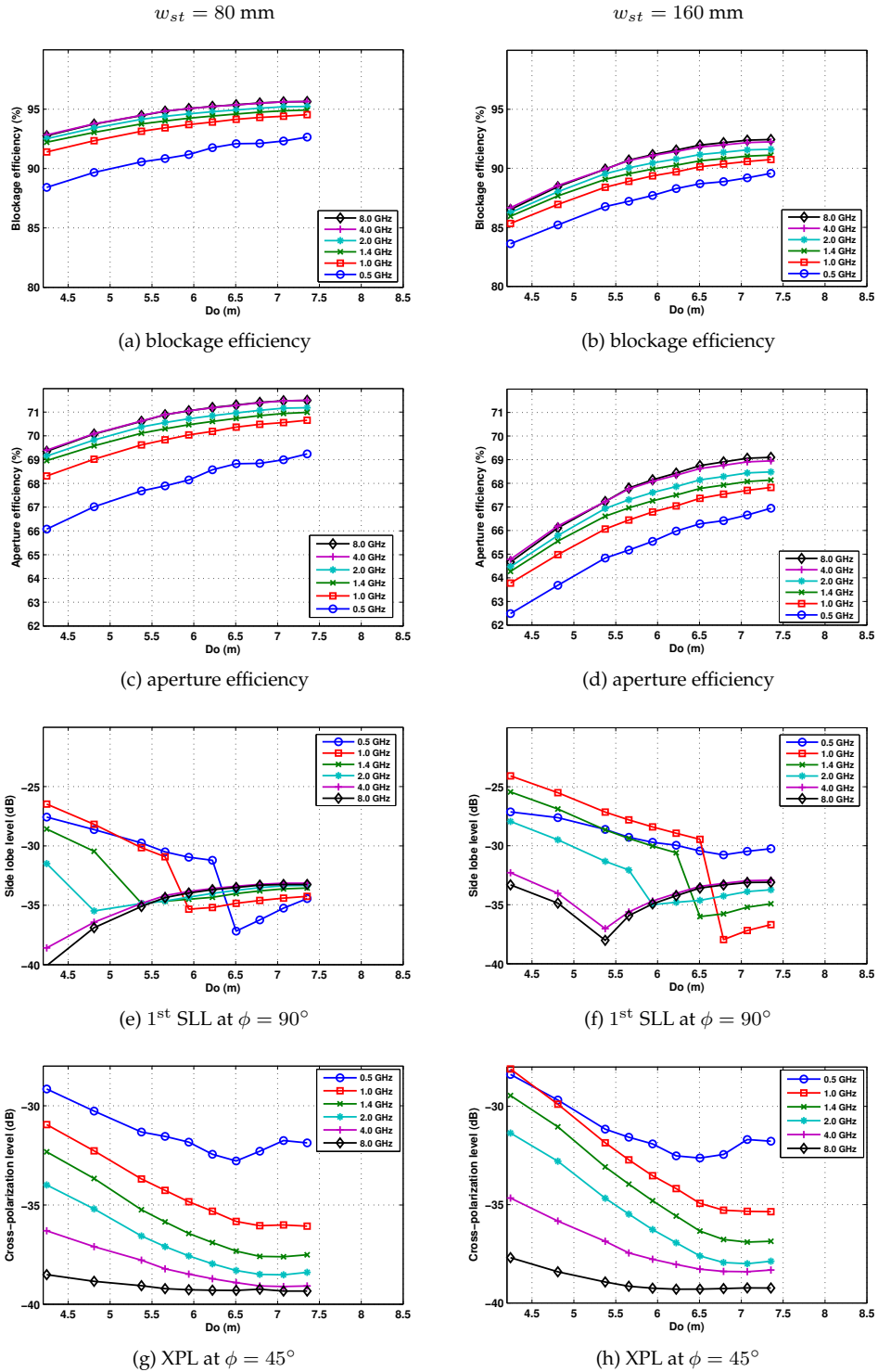


Figure 6.13.: Parameters of the reflector antenna fed with the horn feed supported by four struts: (a)–(b) the blockage efficiency, (c)–(d) the aperture efficiency, (e)–(f) the maximum first side lobe level, and (g)–(h) the relative cross-polarization level at HPBW level ($\phi = 45^\circ$) of $w_{st} = 80 \text{ mm}$ and $w_{st} = 160 \text{ mm}$ at different frequencies versus the strut position parameter D_o .

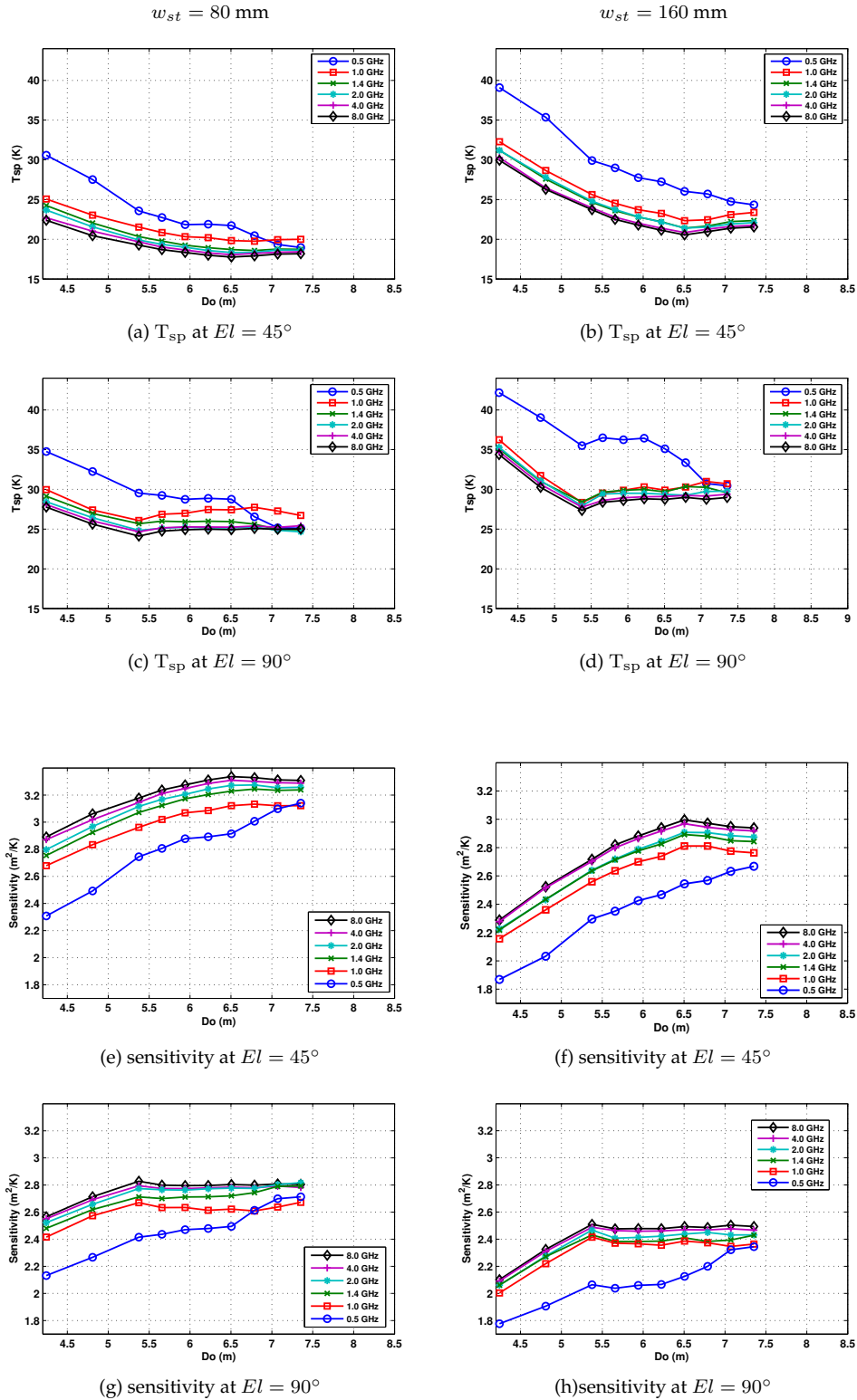


Figure 6.14.: Parameters of the reflector antenna fed with the horn feed supported by four struts: (a)–(d) The spillover noise temperature at $El = 45^\circ$ and $El = 90^\circ$; (e)–(h) the sensitivity at $El = 45^\circ$ and $El = 90^\circ$ due to the ground thermal noise ($T_{\text{ground}} = 300 \text{ K}$) as $T_{\text{rec}} = 20 \text{ K}$ at different frequencies versus the strut position parameter D_o .

6.3.3. Comparison between the Eleven Antenna and Horn Feeds

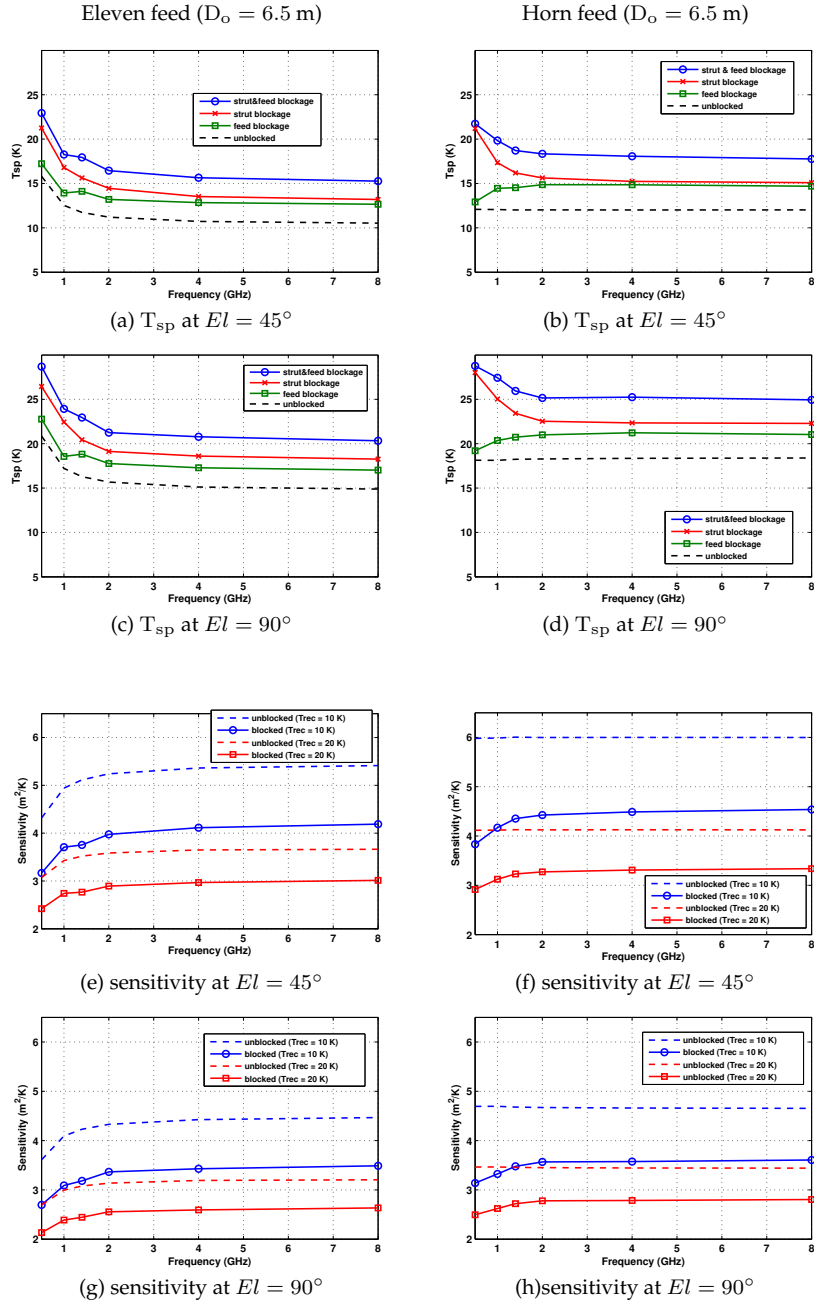


Figure 6.15.: Parameters of the reflector antenna fed with the Eleven feed and the horn feed, supported by four struts: (a)–(d) The spillover noise temperature, (e)–(h) the sensitivity at $El = 45^\circ$ and $El = 90^\circ$ due to the ground thermal noise ($T_{gnd} = 300$ K) as $T_{rec} = 20$ K of optimal D_o over the frequency band.

Figure 6.15 presents the performance comparison between the axi-symmetric reflector systems fed with the Eleven antenna feed and the horn. In this systems, the struts are placed at the optimal position ($D_o = 6.5$ m). Additionally, Figure 6.16 shows far fields from the struts illuminated by these feeds. As one can see, the field levels in the direction of the ground ($\theta = 90\text{--}180^\circ$) are higher for the case of the horn. The relative difference between the spillover noise temperature of the horn and the Eleven feed (due to the direct scattering from the struts) is about 10 K.

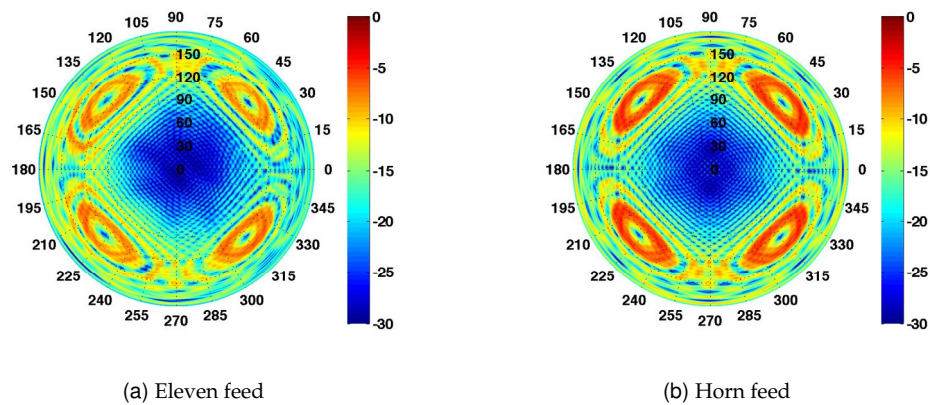


Figure 6.16.: The far field from the four symmetric struts ($w_s = 80$ mm) illuminated by (a) the Eleven antenna and (b) the horn at 500 MHz.

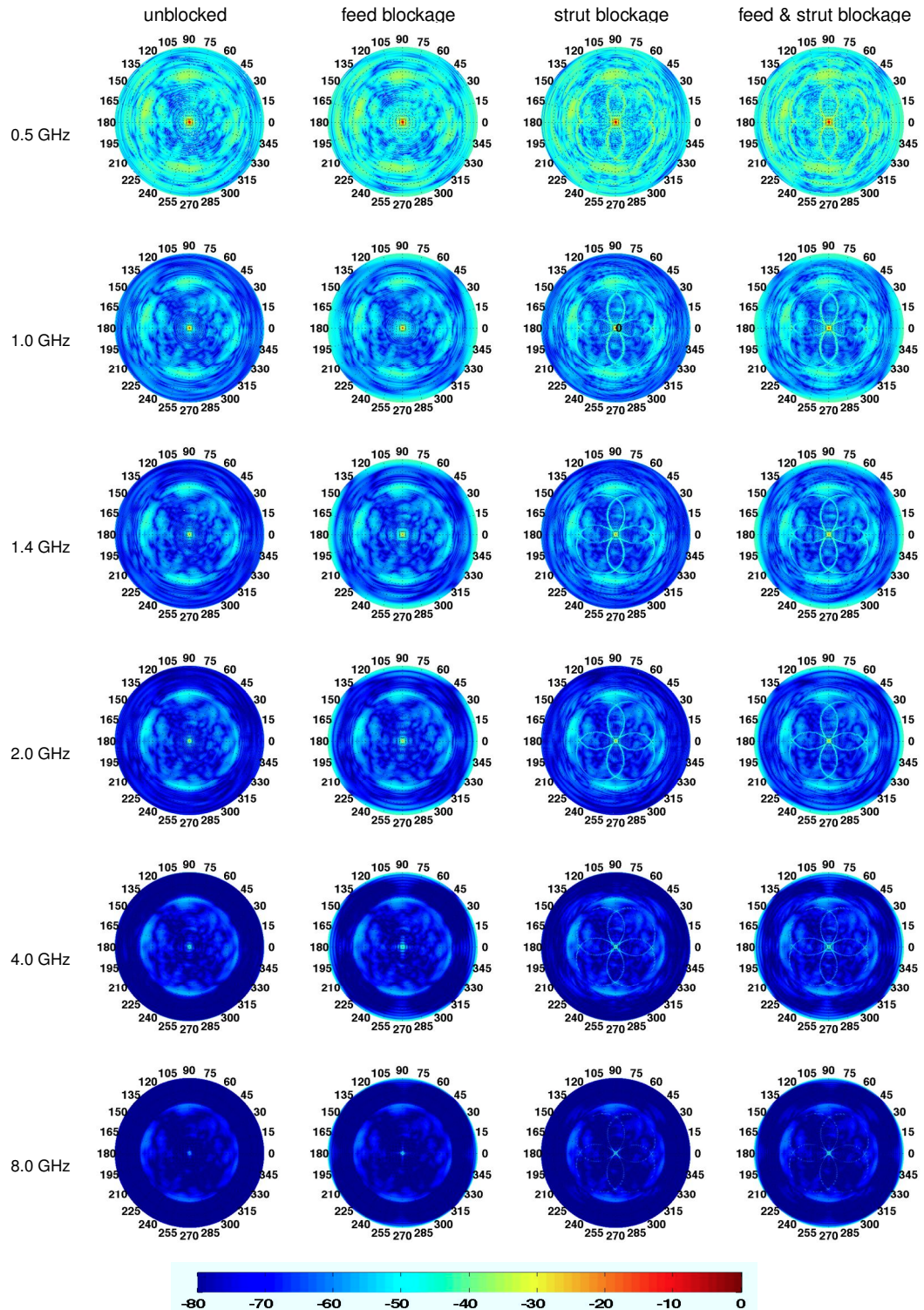


Figure 6.17.: The normalized co-polar far-field patterns of the reflector antenna system with the Eleven feed (for optimal strut placement parameter $D_o = 6.5$ m and $w_{st} = 80$ mm), the range of θ is 0–180° and ϕ is 0–360° for different frequencies. The size of the feed blockage area is 660 mm×660 mm×210 mm.

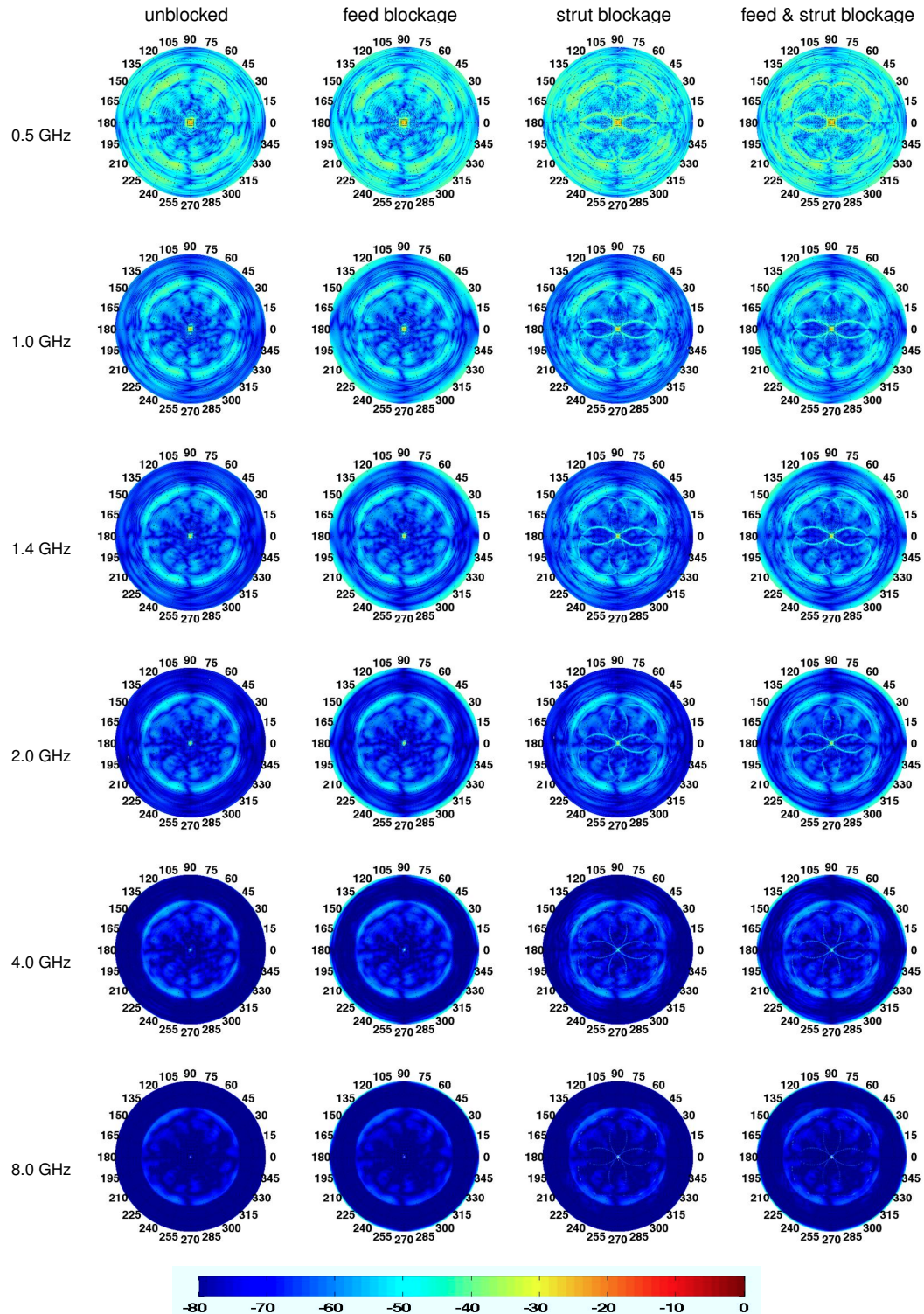


Figure 6.18.: The normalized cross-polar far-field patterns of the reflector antenna system with the Elemen feed (for optimal strut placement parameter $D_o = 6.5$ m and $w_{st} = 80$ mm), the range of θ is 0 – 180° and ϕ is 0 – 360° for different frequencies. The size of the feed blockage area is 660 mm \times 660 mm \times 210 mm.

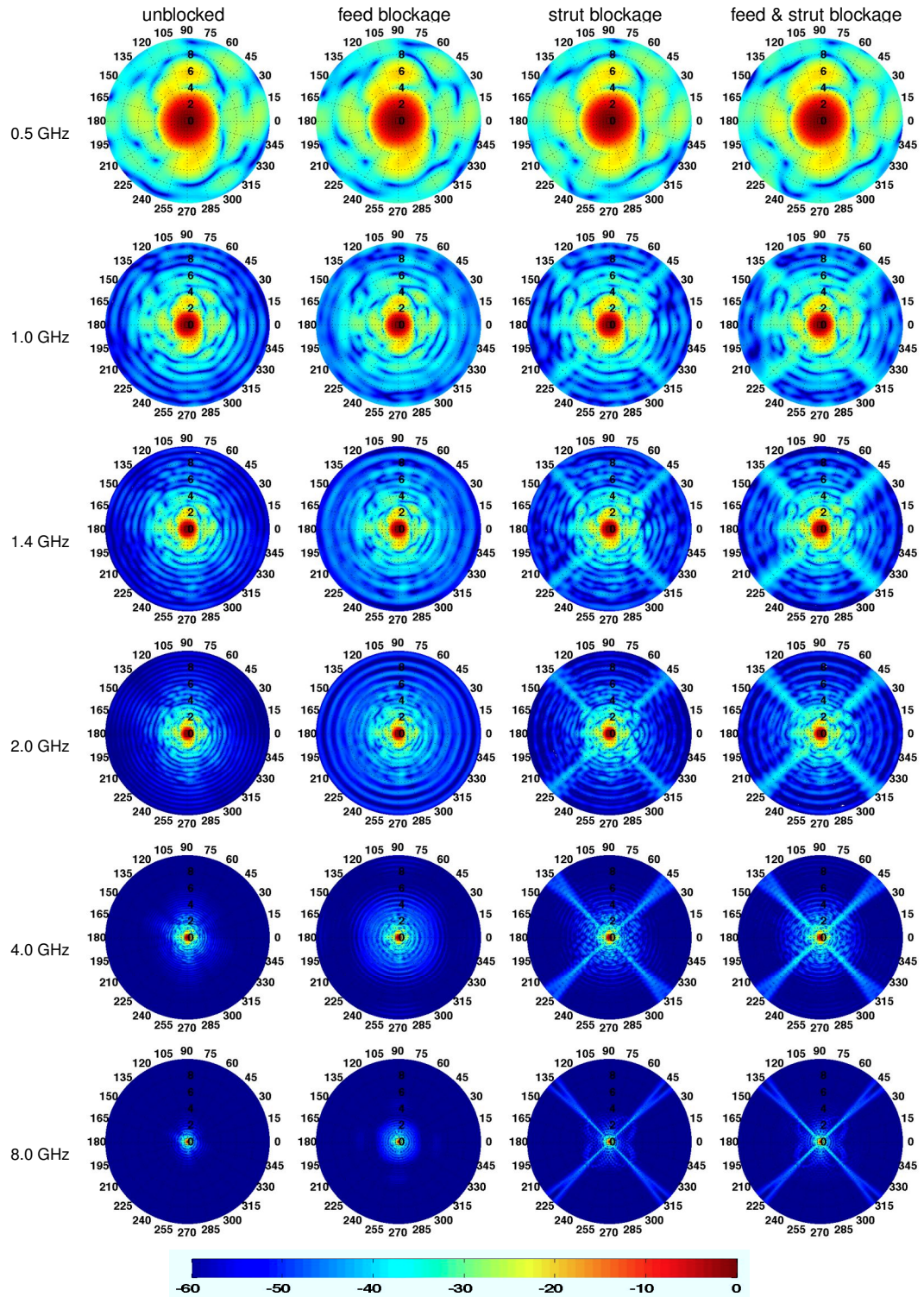


Figure 6.19.: The normalized co-polar far-field patterns of the reflector antenna system with the Eleven feed (for optimal strut placement parameter $D_o = 6.5$ m and $w_{st} = 80$ mm), the range of θ is 0 – 10° and ϕ is 0 – 360° for different frequencies. The size of the feed blockage area is 660 mm \times 660 mm \times 210 mm.

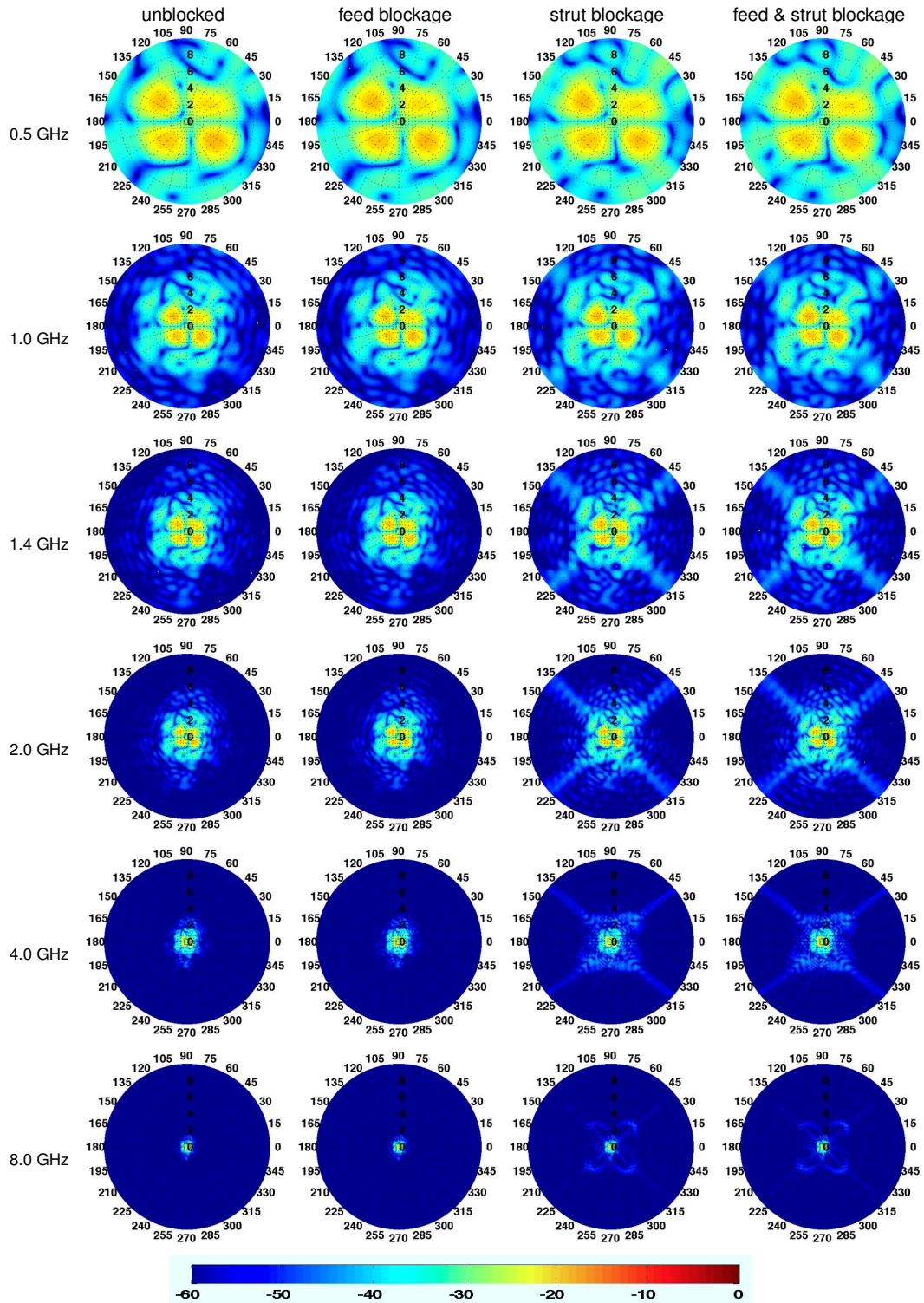


Figure 6.20.: The normalized cross-polar far-field patterns of the reflector antenna system with the Elemen feed (for optimal strut placement parameter $D_o = 6.5$ m and $w_{st} = 80$ mm), the range of θ is $0-10^\circ$ and ϕ is $0-360^\circ$ for different frequencies. The size of the feed blockage area is $660 \text{ mm} \times 660 \text{ mm} \times 210 \text{ mm}$.

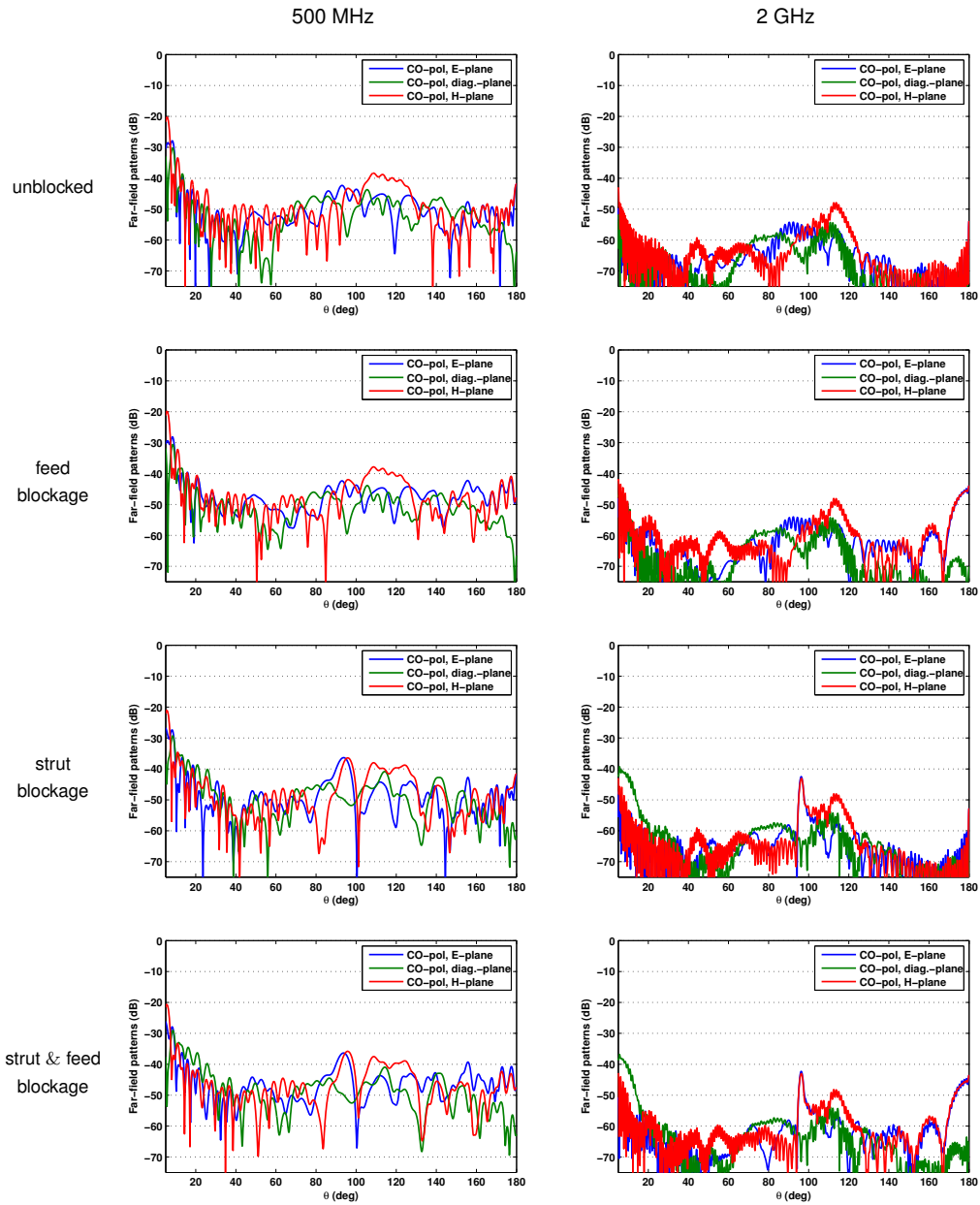


Figure 6.21.: Co-polar far-field patterns of the axi-symmetric reflector antenna system with the Eleven feed (for optimal strut placement parameter $D_o = 6.5$ m and $w_{st} = 80$ mm) calculated by the rigorous solution for different frequencies. The size of the feed blockage area is 660 mm \times 660 mm \times 210 mm.

Table 6.3.: The summary of the performance parameters of the reflector antenna system with the aperture diameter of 15 meters for the optimized optics structure (optimal F/D and D_0). The results are shown for the E-plane antenna and horn feed; and assume the constant receiver noise temperature of 20 K.

FEED PARAMETERS:	E-plane feed ($w_{sf} = 80$ mm)					Horn feed ($w_{sf} = 80$ mm)					Horn feed ($w_{sf} = 160$ mm)							
	0.5	1	1.4	2	4	8	0.5	1	1.4	2	4	8	0.5	1	1.4	2	4	8
Aperture diameter of the feed at the lowest freq. (λ)			1.1						1.9									1.9
10 dB Feed beamwidth			55.09°						54.69°									54.69°
Ref. edge illumination taper			-11.77						-12.56									-12.56
XPLmax (dB)			-26.37						-75.15									-75.15
REFL-FEED PARAMETERS:	Frequency (GHz)					Frequency (GHz)					Frequency (GHz)							
Aperture efficiency (dB)	-2.29	-2.27	-2.27	-2.25	-2.24	-2.23	-1.6	-1.5	-1.48	-1.46	-1.44	-1.44	-1.79	-1.72	-1.69	-1.67	-1.64	-1.63
Blockage efficiency (dB) (due to struts and feed)	-0.29	-0.27	-0.25	-0.24	-0.23	-0.21	-0.37	-0.27	-0.25	-0.23	-0.21	-0.21	-0.52	-0.45	-0.43	-0.4	-0.37	-0.36
1 st SLL (dB)	-20.9	-20.9	-20.8	-20.5	-20.2	-20.2	-37.2	-34.8	-34.0	-33.7	-33.4	-33.5	-30.4	-29.5	-36	-34.6	-33.4	-33.6
max XPL at HPBW (dB)	-22.3	-22.2	-22.2	-22.2	-22.4	-22.5	-32.8	-35.8	-37.3	-38.3	-38.9	-39.3	-32.6	-34.9	-36.3	-37.6	-38.3	-39.3
T _{sp} at $E/l = 90^\circ$ (K)	28.7	23.9	23.0	21.3	20.8	20.3	28.8	27.4	26.0	25.2	24.9	24.9	36.4	30.3	30.0	29.5	29.1	28.8
T _{sp} at $E/l = 45^\circ$ (K)	22.9	18.3	17.9	16.5	15.7	15.3	21.7	19.8	18.7	18.3	18.1	17.8	26.0	22.4	21.4	21.4	20.9	20.6
Sensitivity at $E/l = 90^\circ$ (m ² /K)	2.13	2.39	2.44	2.56	2.6	2.63	2.5	2.62	2.72	2.78	2.79	2.8	2.13	2.39	2.41	2.44	2.47	2.49
Sensitivity at $E/l = 45^\circ$ (m ² /K)	2.42	2.74	2.77	2.89	2.97	3.01	2.92	3.12	3.23	3.27	3.31	3.34	2.54	2.81	2.89	2.91	2.97	3

Conclusions

In conclusion, we summarize the observations made in our numerical study:

- It is important to choose an optimal discretization step for the simulated antenna far-field patterns in order to compute and evaluate the antenna performance efficiently and accurately. Since the side lobe beamwidth depends on the frequency, the required discretization step $\Delta\theta$ should be smaller and smaller as frequency increased. The discretization step must be at least four times smaller than side lobe beamwidth, defined as the distance between the nulls, so as to obtain acceptable accuracy.
- The geometry of the reflector antenna (F/D) and configuration of its aperture blocking structures represent important design parameters of radio telescopes which affect the overall system sensitivity besides the receiver noise temperature. For receivers with the noise temperatures in the order of $T_{\text{rec}} = 20$ K (for the case of the Eleven feed at present), the optimal value of F/D is close to 0.42 that is the result of the interplay between the antenna spillover and T_{rec} noise contributions, and the antenna aperture efficiency.
- Judicious choice of the position of struts can reduce the deterioration on the aperture efficiency, side lobes and cross-polarization, which are comparable to that of the reflector modeled without struts. For the reflector system with $F/D = 0.42$ and the Eleven antenna feed, the optimal strut position parameter D_o equals to 6.5 m, of which T_{sys} increases less than 5 K; the blockage efficiency is about 95%; SLL and XPL are virtually identical to those of the unblocked aperture (about -20 dB and -22 dB). For the case of the horn feed operating in the same reflector system, T_{sys} increases about 7–10 K; the blockage efficiency is around 95% except for the frequency below 1 GHz; SLL and XPL increase but still below -30 dB.
- Wider diameter of struts leads to higher XPL (increase of 3 dB) and antenna noise temperature (increase of 2–5 K), lower aperture efficiency (reduction of 5%), and therefore lower sensitivity (about 20–30% lower than that of the unblocked aperture).
- The optimal position of the strut is weakly dependent on the type of feed and the strut width. However, when the strut cross-section diameter increases, the range of the optimal placement of struts becomes narrower. In practice the design of reflector system (reflector and struts) will be more sensitive to the manufacturing tolerances.

Conclusions

Summary of the work:

- The performance of the wideband Eleven antenna feed in combination with the axisymmetric reflector system for applications in future radio telescopes has been investigated. This numerical study has demonstrated that geometries of the reflector antenna (F/D) and feed supporting structure represent important factors affecting the telescope's parameters, such as the aperture efficiency, SLL and XPL, spillover noise temperature and the overall system sensitivity.
- For the case of the decade bandwidth Eleven feed receiver with $T_{\text{rec}} = 20$ K, the optimal reflector F/D ratio for the maximum sensitivity is close to 0.42 (half illumination angle of 62°), but it becomes smaller for receivers with lower T_{rec} .
- The blockage effects caused by the struts and feed structure reduce the antenna aperture efficiency, and increase the spillover loss due to higher far SLLs and back radiation, as compared to the ideal system with the unblocked aperture.

Problem with conventional MFFEs:

For conventional multi-frequency front ends (which consist of several narrow band horn receivers and hence require large supporting structures), these blockage effects are significant:

- The relative aperture efficiency loss and increase of T_{sp} are typically 10–15% and 10–20 K.
- The corresponding sensitivity loss is about 20–30%. Increase of SLL is a few dB.

Eleven feed performance:

- For the next generation telescopes, the difficulties in supporting multiple receivers will not be as large; if a set of 2–3 wideband feeds is used instead of multiple single-octave horns.
- Our numerical study has shown that it is possible to minimize the blockage effects by choosing a set of two wideband Eleven feeds, each operating with the 4:1 bandwidth, and optimizing the strut position for the maximum receiving sensitivity:
 - The resultant aperture efficiency loss and increase of T_{sp} have been found to be in the order of 5% and 5 K with respect to the ideal system with the unblocked aperture.
 - The corresponding sensitivity is only 10–15% lower over the frequency band from 0.5 to 8 GHz, which is relatively small given the large difference between the bandwidth of the horn and Eleven antenna.
 - The cross-polarization and side lobe levels are comparable to the ideal system.
- The above results were obtained for the optimized system with $F/D = 0.42$ and the struts positioned closely to the rim of the reflector ($D_o = 6.5$ m, where the radius of the reflector is 7.5 meters).

Strut optimization strategy:

- The optimal position of the strut is weakly dependent on the type of feed and the strut width. It is mainly the reflector shape (F/D) that plays the determinant role. However, when the strut width increases, the range of the optimal placement of struts becomes narrower.
- The optimization of strut positions for the minimum T_{sp} also provides the maximum sensitivity, since the aperture blockage efficiency is a slowly varying function of the strut position D_o , (as long as the struts are close to the rim of the reflector.) The T_{sp} contribution is strongly dependent on D_o , and there exists a minimum of this function. This minimum also depends on the antenna pointing direction, so it should be accounted for in the optimization.

Appendices

Appendix A

Matlab Code—Simpson’s Rule for Calculating of the Aperture Efficiency

We employ numerical method—Simpson’s rule to calculate aperture efficiency (Eq. 2.2.2) and put it into practice via MATLAB. Simpson’s rule is a Newton-Cotes formula for approximating the integral of a function f using quadratic polynomials (i.e., parabolic arcs instead of the straight line segments used in the trapezoidal rule). Simpson’s rule can be derived by integrating a third-order Lagrange interpolating polynomial fit to the function at three equally spaced points. In particular, let the function f be tabulated at points x_0 , x_1 , and x_2 equally spaced by distance h , and denote $f_n = f(x_n)$. Then Simpson’s rule states that [43]

$$\int_{x_0}^{x_2} f(x) dx = \int_{x_0}^{x_0+2h} f(x) dx \quad (\text{A.0.1})$$

$$\approx \frac{1}{3} h(f_0 + 4f_1 + f_2). \quad (\text{A.0.2})$$

Since it uses quadratic polynomials to approximate functions, Simpson’s rule actually gives exact results when approximating integrals of polynomials up to cubic degree. A MATLAB function performing Simpson’s rule to calculate aperture efficiency is listed below. Moreover, equation 2.2.2 is only for calculating one single ϕ -plane. In our numerical calculation, we calculated all the ϕ -plane from 0–360° and average it.

```
Calculate Aperture Efficiency by applying Simpson’s rule

for iphi = 1:360 % phi = 0-360 deg
    inx = 1:60; % subtended angle =60 deg, F/D = 0.433
        %Simpson’s rule
```

*APPENDIX A. MATLAB CODE—SIMPSON'S RULE FOR CALCULATING OF THE
APERTURE EFFICIENCY*

```

int_su = int_su + (dt/6) * ( tand((inx-1)/2)*CO(inx, iphi) +...
    4*((tand((inx-1)/2)+tand(inx/2))/2*(CO(inx, iphi)+CO(inx+1, iphi))/2) +...
    tand((inx)/2)*CO(inx+1, iphi) );

inx = 1:180; % theta =0-180 deg
%Simpson's rule
int_sd = int_sd+ (dt/6)*( sind(inx-1)*(abs(CO(inx, iphi)).^2+abs(XP(inx, iphi)).^2)...
    + 4*((sind(inx-1)+sind(inx))/2)*(abs((CO(inx, iphi)+CO(inx+1, iphi))/2).^2 + ...
    abs((XP(inx, iphi)+XP(inx+1, iphi))/2).^2))...
    + sind(inx)*(abs(CO(inx+1, iphi)).^2+abs(XP(inx+1, iphi)).^2) );
end

the aperture efficiency: calculate the value in each phi plane, sum up and average it
eta_fns(ifq) = 2*cotd(60/2)^2*abs(sum(int_su)/360)^2/(sum(int_sd)/360);

```

Appendix **B**

Command List in GRASP 9 for the Analysis of Reflector Antennas

No blockage:

```
1: Refl_po<Get Currents < {Command attributes}
2: main_tot_range < Get Field < Refl_po
3: main_tot_range < Add Field < Eleven_Feed
```

Account for central blockage:

```
4: main_tot_range_CB < Get Pattern < {Command attributes}
5: Refl_po < Get currents < {Command attributes}
6: feedbox_po < Get Currents < {Command attributes}
7: main_tot_range_CB < Add Field < feedbox_po
```

Account for strut effects:

```
8: All_Struts_po_Feed < Get Currents < {Command attributes}
9: Refl_po_all < Get Currents < {Command attributes}
10: All_Struts_cut_swpw < Get Field < Refl_po_all
11: All_Struts_po < Get Currents < {Command attributes}
12: All_Struts_cut_swpw < Add Field < All_Struts_po
13: All_Struts_cut_swpw < Add Field < Eleven_Feed
```

Account for both central blockage and strut effects:

```
14: All_Struts_cut_swpw_CB < Get Pattern < {Command attributes}
15: Refl_po < Get Currents < {Command attributes}
16: feedbox_po_all < Get Currents < {Command attributes}
17: All_Struts_cut_swpw_CB < Add Field < feedbox_po_all
```


Appendix **C**

Additional Figures

Start from next page.

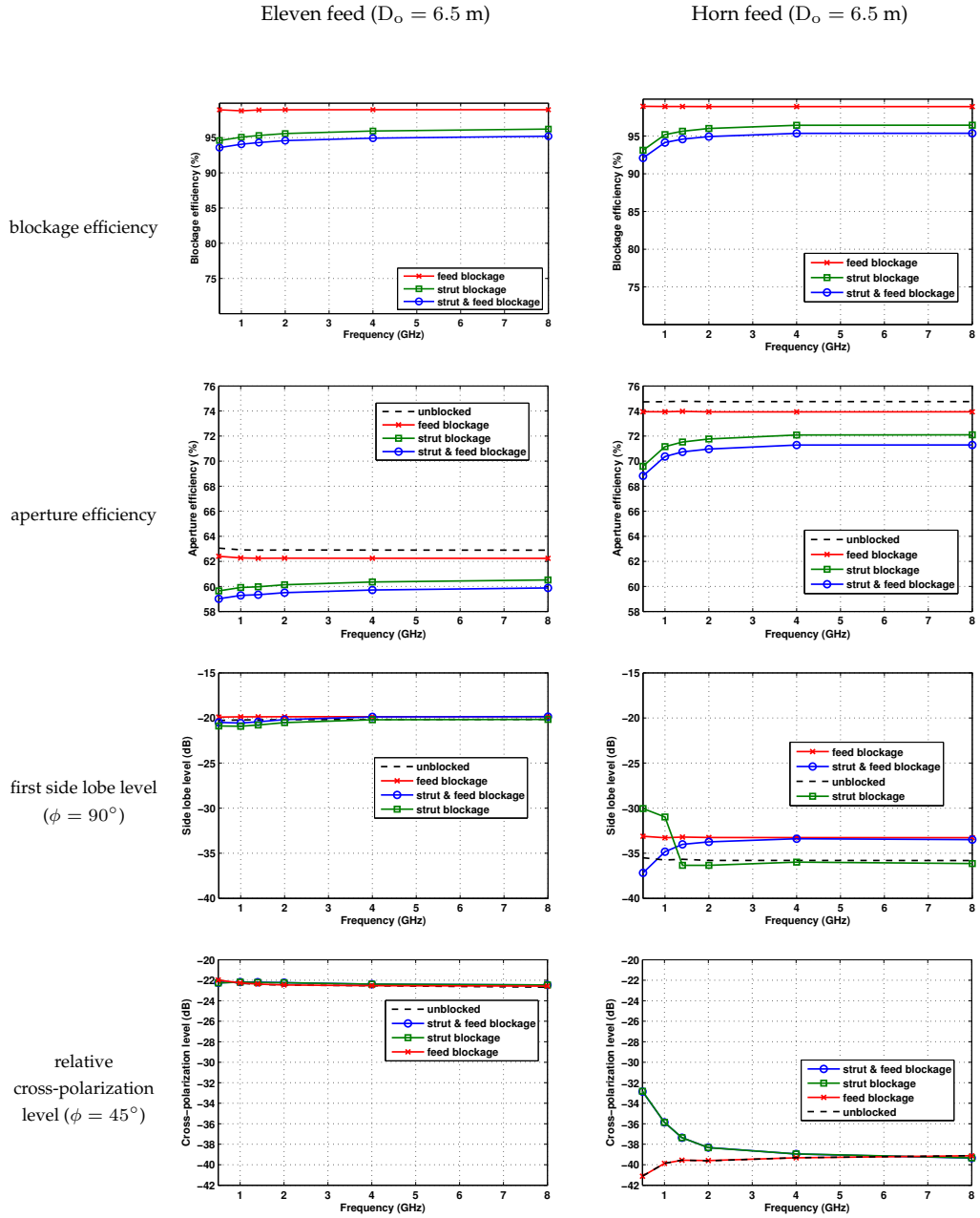
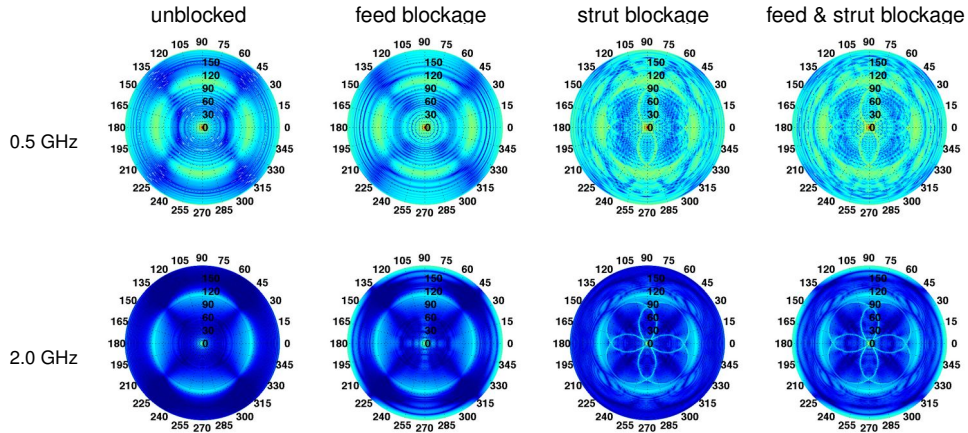
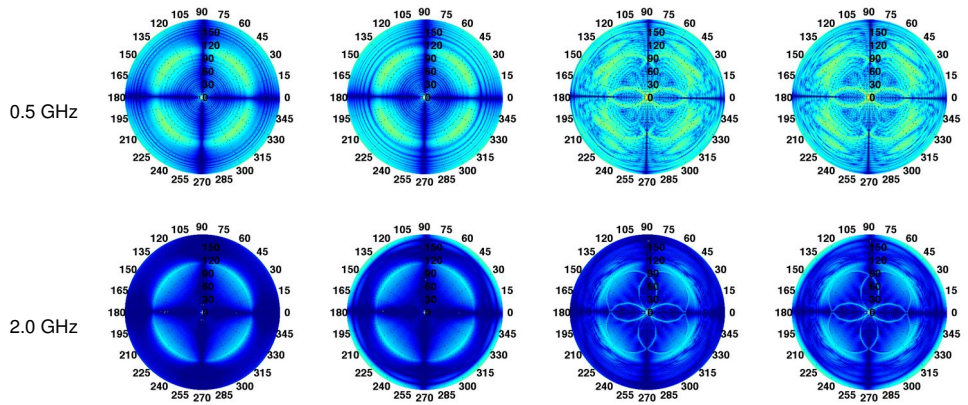


Figure C.1.: The key parameters of the reflector antenna fed with the Eleven feed and the horn feed, which supported by four struts: the aperture efficiency reduction, the aperture efficiency, the maximum first side lobe level, and the relative cross-polarization level at the half-power beamwidth direction ($\phi = 45^\circ$) at optimal D_o as a function of frequency.



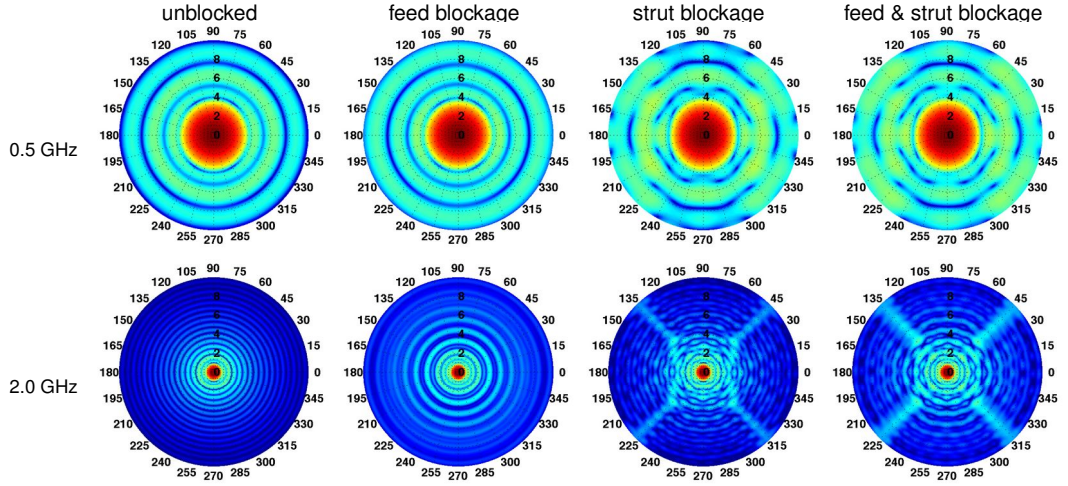
(a) co-polar far-field patterns



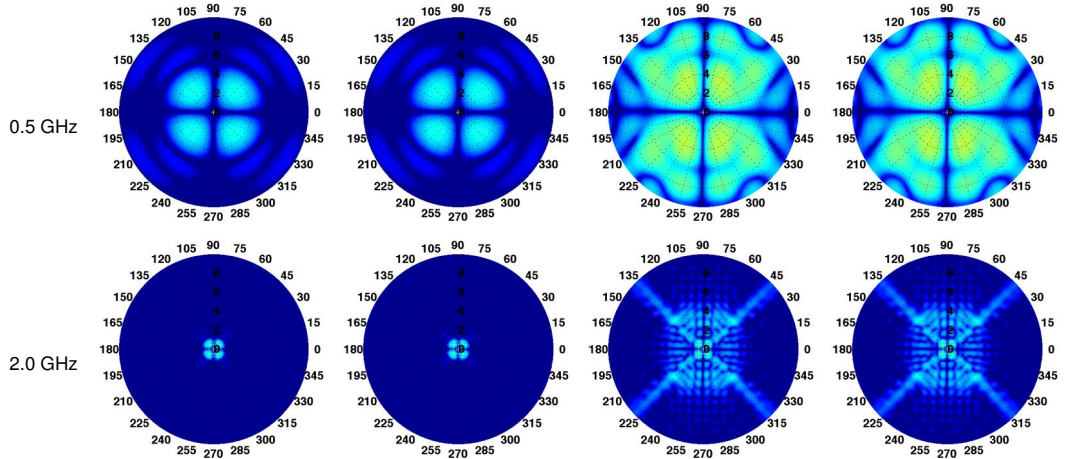
(b) cross-polar far-field patterns



Figure C.2.: The normalized (a) co-polar and (b) cross-polar far-field patterns of the reflector antenna system with the **horn feed** (for optimal strut placement parameter $D_o = 6.5$ m and $w_{st} = 80$ mm), the range of θ is $0-180^\circ$ and ϕ is $0-360^\circ$ for different frequencies. The size of the feed blockage area is $660\text{ mm} \times 660\text{ mm} \times 210\text{ mm}$.



(a) co-polar far-field patterns



(b) cross-polar far-field patterns

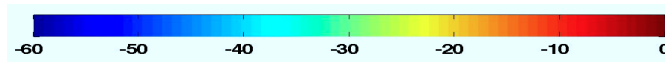


Figure C.3.: The normalized (a) co-polar and (b) cross-polar far-field patterns of the reflector antenna system with the **horn feed** (for optimal strut placement parameter $D_o = 6.5$ m and $w_{st} = 80$ mm), the range of θ is $0-10^\circ$ and ϕ is $0-360^\circ$ for different frequencies. The size of the feed blockage area is $660\text{ mm} \times 660\text{ mm} \times 210\text{ mm}$.

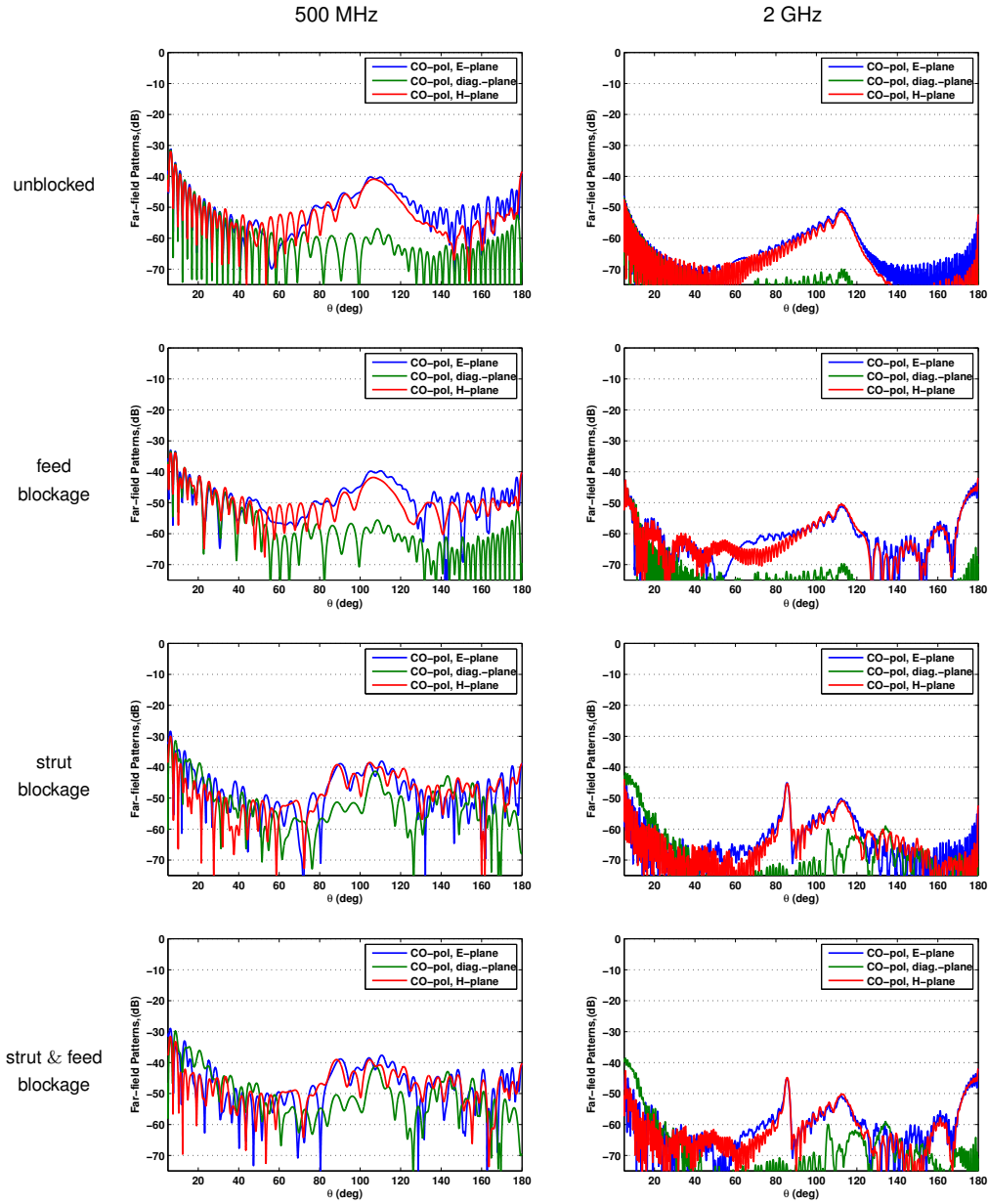
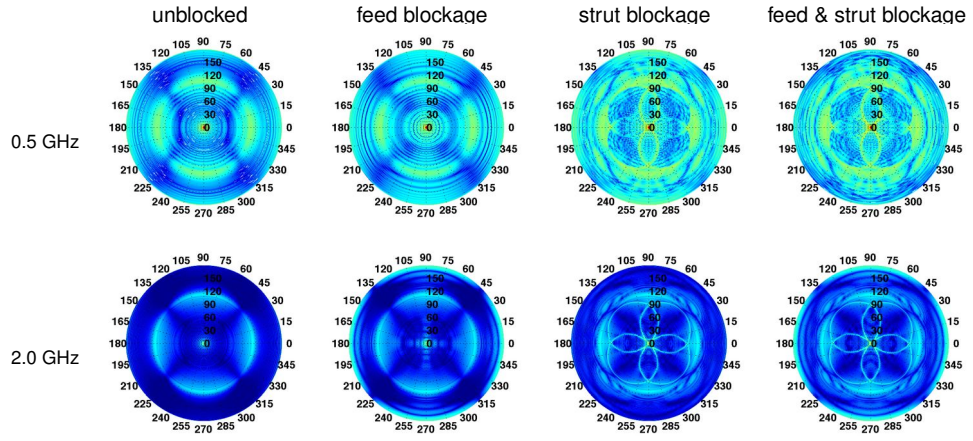
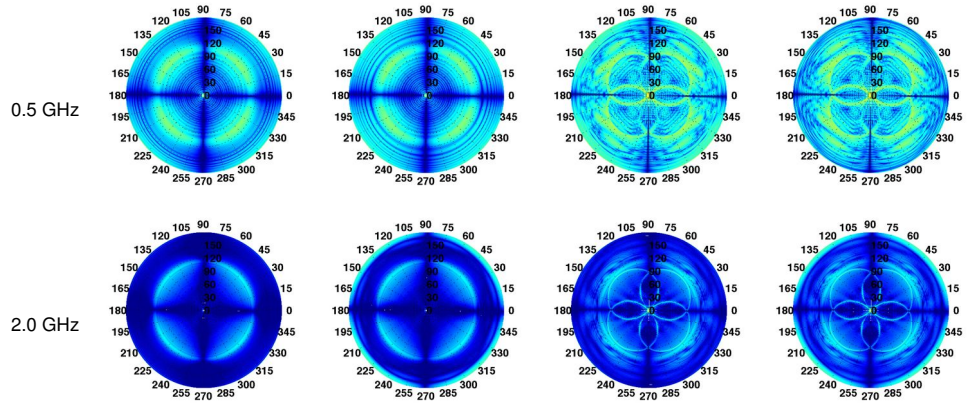


Figure C.4.: Co-polar far-field patterns of the axi-symmetric reflector antenna system with the horn feed (for optimal strut placement parameter $D_o = 6.5$ m and $w_{st} = 80$ mm) calculated by the rigorous solution for different frequencies. The size of the feed blockage area is $660 \text{ mm} \times 660 \text{ mm} \times 210 \text{ mm}$.



(a) co-polar far-field patterns



(b) cross-polar far-field patterns

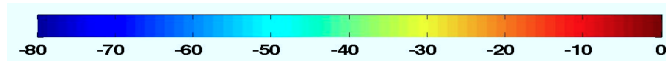


Figure C.5.: The normalized (a) co-polar and (b) cross-polar far-field patterns of the reflector antenna system with the **horn feed** (for optimal strut placement parameter $D_o = 6.5$ m and $w_{st} = 160$ mm), the range of θ is $0-180^\circ$ and ϕ is $0-360^\circ$ for different frequencies. The size of the feed blockage area is $660 \text{ mm} \times 660 \text{ mm} \times 210 \text{ mm}$.

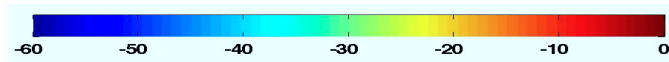
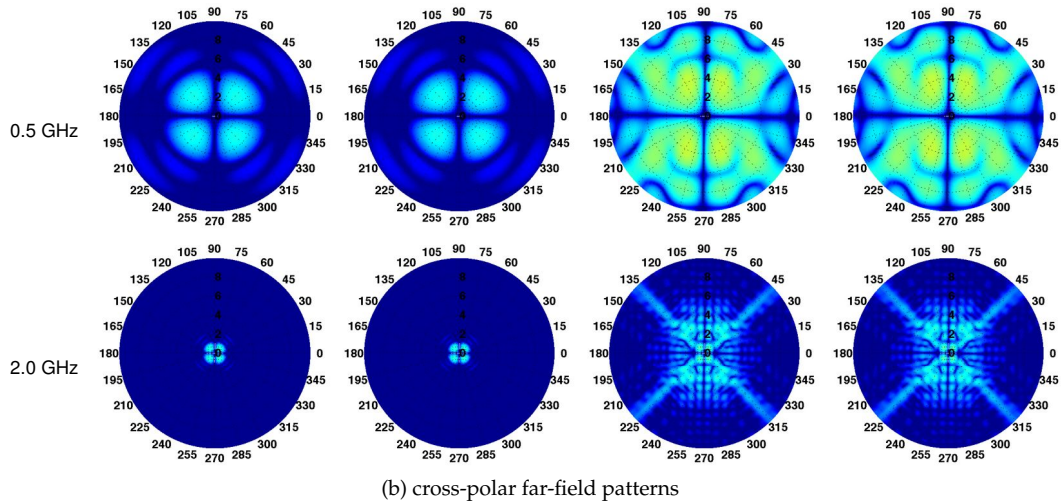
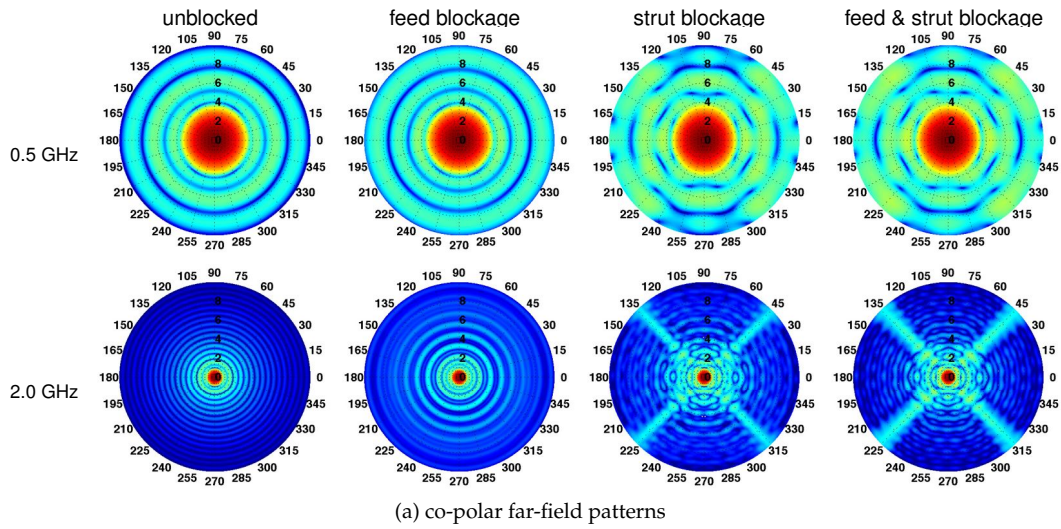


Figure C.6.: The normalized (a) co-polar and (b) cross-polar far-field patterns of the reflector antenna system with the **horn feed** (for optimal strut placement parameter $D_o = 6.5$ m and $w_{st} = 160$ mm), the range of θ is $0-10^\circ$ and ϕ is $0-360^\circ$ for different frequencies. The size of the feed blockage area is $660\text{ mm} \times 660\text{ mm} \times 210\text{ mm}$.

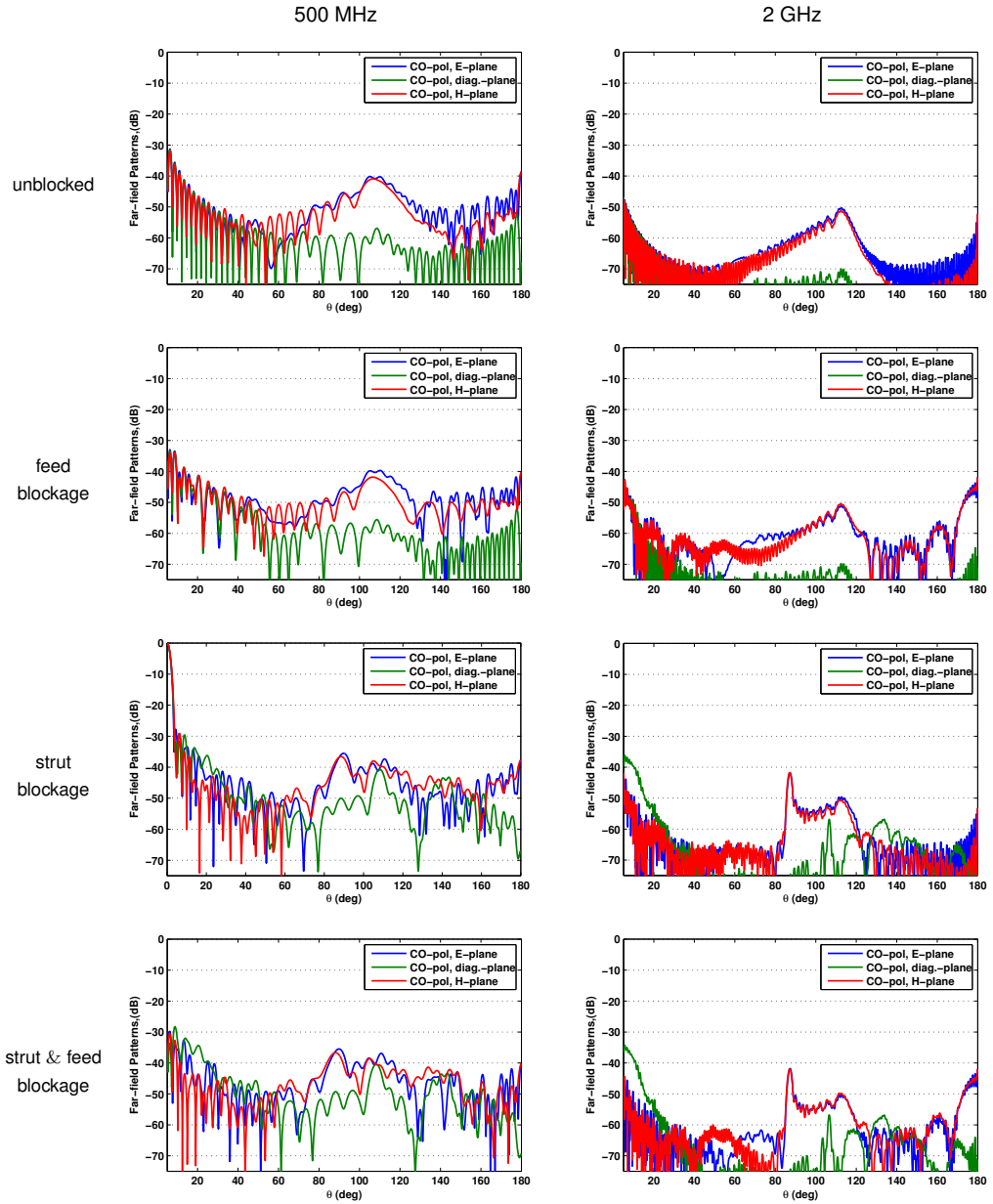


Figure C.7.: Co-polar far-field patterns of the axi-symmetric reflector antenna system with the horn feed (for optimal strut placement parameter $D_o = 6.5$ m and $w_{st} = 160$ mm) calculated by the rigorous solution for different frequencies. The size of the feed blockage area is $660 \text{ mm} \times 660 \text{ mm} \times 210 \text{ mm}$.

References

- [1] W.-C. Liao, M.V. Ivashina, P.-S. Kildal, and A. van Ardenne. Analysis of the strut and feed blockage effects in radio telescopes with compact UWB feeds. *Proceedings of the 6th European Conference on Antennas and Propagation (EUCAP)*, 2012.
- [2] Wikipedia, . URL http://www.en.wikipedia.org/wiki/Radio_waves.
- [3] Wikipedia, . URL http://www.en.wikipedia.org/wiki/Westerbork_Synthesis_Radio_Telescope.
- [4] Square Kilometer Array (SKA). URL <http://www.skatelescope.org>.
- [5] John. D. Bunton, T. Joseph, and W. Lazio. The Square Kilometre Array: An engineering perspective, 2005. Cylinder–Small Dish Hybrid for the SKA.
- [6] W. Imbriale, G. Cortes-Medellin, and L. Baker. Considerations for the SKA offset optics design. *National Radio Sci. Meeting*, 2010.
- [7] M.V. Ivashina, R. Bakker, J.G. Bij de Vaate, O.A. Iupikov, M. Arts, J. Dekker, and A. van Ardenne. An axi-symmetric segmented composite SKA dish design: Performance and production analysis. *Asia Pacific MW Conf. (APMC2011)*, Melbourne, Dec 2011.
- [8] O. M. Smirnov. Revisiting the radio interferometer measurement equation I. A full-sky Jones formalism. *Astronomy and Astrophysics Supplement Series*, 527:11, March 2011.
- [9] W.A. Imbriale, G. Cortes-Medellin, and L. Baker. Update on the SKA offset optics design for the U.S. technology development project. *IEEE Aerospace Conference*, pages 1–10, March 2011.
- [10] Projects: TC-SKAR Airborne. URL <http://www.airborne.nl/projects/tc-skar>.
- [11] H. Tanaka and M. Mizusawa. Elimination of cross-polarization in offset dual-reflector antennas. *Trans. Inst. Electron. Commun. Eng. Japan*, 58-B(12):643–650, December 1975.
- [12] Per-Simon. Kildal. *Foundations of Antennas - A Unified Approach*, page 71. Studentlitteratur AB, January 2000.
- [13] Per-Simon. Kildal. Factorization of the feed efficiency of paraboloids and Cassegrain antennas. *IEEE Transactions on Antennas and Propagation*, 33(8):903–908, August 1985.

- [14] R. E. Collin. Aperture efficiency of paraboloidal reflectors. *IEEE Transactions on Antennas and Propagation*, 32(9): 997–1000, September 1984.
- [15] M. Ivashina, R. Maaskant, and B. Woestenburg. Equivalent system representation to model the beam sensitivity of receiving antenna arrays. *IEEE Antennas and wireless Propagation Letters*, 7:733–737, October 2008.
- [16] Jian Yang, M. Panteleev, P.-S. Kildal, B. Klein, Y. Karandikar, L. Helldner, N. Wadefalk, and C. Beaudoin. Cryogenic 2–13 GHz Eleven feed for reflector antennas in future wideband radio telescope. *IEEE Transactions on Antennas and Propagation*, 59(6):1918–1934, June 2011.
- [17] G. Engargiola. Non-planar log-periodic antenna feed for integration with a cryogenic microwave amplifier. *IEEE Antennas and Propagation Society International Symposium*, 4:140–143, 2002.
- [18] Allen Telescope Array (ATA). URL <http://www.seti.org/ata>.
- [19] V. Rodriguez. An open-boundary quad-ridged guide horn antenna for use as a source in antenna pattern measurement anechoic chambers. *IEEE Transactions on Antennas and Propagation*, 48(2):157–160, April 2006.
- [20] G. Cortes-Medellin. Non-planar quasi-self-complementary ultra-wideband feed antenna. *IEEE Transactions on Antennas and Propagation*, 59(6):1935–1944, June 2011.
- [21] W.A. Imbriale and A. Akgiray. Performance of a quad-ridged feed in a wideband radio telescope. Proceedings of the 5th European Conference on Antennas and Propagation (EUCAP), Rome, Italy, April 2011.
- [22] N. Wadefalk and S. Weinreb. Noise testing for the active and passive baluns for the ATA. ATA memo #67, 2004.
- [23] J. Welch and D. Backer. The Allen Telescope Array: The first widefield, panchromatic, snapshot radio camera for radio astronomy and SETI. 0117-SIP-2008-PIEEE, 2008.
- [24] D. Ericsson, P.-S. Kildal, and S. Weinreb. Study of efficiencies and phase centers of broadband log-periodic feeds for large offset dual-reflector antennas using formulas for bodies of revolution (BOR₁ extraction). *IEEE Antennas Propagat. Int. Symposium*, 1:241–244, August 2003.
- [25] Per-Simon Kildal and Z. Sipus. Classification of rotationally symmetric antennas as types BOR₀ and BOR₁. *IEEE Transactions on Antennas and Propagation*, 37(6):114, January 2010.
- [26] Jian Yang, Sergey Pivnenko, and Per-Simon Kildal. Comparison of two decade-bandwidth feeds for reflector antennas: The Eleven antenna and quadridge horn. *Proceedings of the Fourth European Conference on Antennas and Propagation (EuCAP)*, pages 1–5, April 2010.
- [27] G. Cortes-Medellin. Novel non planar ultra wide band quasi self-complementary antenna. *IEEE Antennas and Propagation Society International Symposium*, pages 5733 – 5736, June 2007. Honolulu, Hawaii.
- [28] S. Christiansen. *Radiotelescopes*. Cambridge, U.K.: Cambridge Univ. Press, 1969.
- [29] R. Olsson, P.-S. Kildal, and S. Weinreb. The Eleven antenna: a compact low-profile decade bandwidth dual polarized feed for reflector antennas. *IEEE Transactions on Antennas and Propagation*, 54(2):368–375, February 2006.
- [30] Jian Yang, Xiaoming Chen, N. Wadefalk, and P.-S. Kildal. Design and realization of a linearly polarized Eleven feed for 1–10 GHz. *IEEE Antennas and Wireless Propagation Letters*, 8:64–68, 2009.
- [31] GRASP 9, antenna systems simulation software, TICRA. URL <http://www.ticra.com>.
- [32] *GRASP 9 Technical Description*.

-
- [33] Wikipedia-Riemann Sum. URL http://en.wikipedia.org/wiki/Riemann_sum#Left_sum.
- [34] Wikipedia-Midpoint Method. URL http://en.wikipedia.org/wiki/Midpoint_method.
- [35] Personal communication with Jian Yang. Dept. of Signals and Systems, Chalmers University of Technology, S-41296, Gothenburg, Sweden. E-mail: jian.yang@chalmers.se.
- [36] B. Klein, M.V. Ivashina, R. Maaskant, A.R Clark, and M. Panteleev. Development of a detailed system model of the Eleven feed receiver using the CAESAR software. *Proceedings of the 6th European Conference on Antennas and Propagation (EUCAP)*, 2012.
- [37] O.M. Smirnov and M.V. Ivashina. Element gain drifts as an imaging dynamic range limitation in PAF-based interferometers. *General Assembly and Scientific Symposium*, pages 1–4, August 2011.
- [38] W.A. van Cappellen and M.V. Ivashina. Temporal beam pattern stability of a radio astronomy phased array feed. *Proceedings of the 5th European Conference on Antennas and Propagation (EUCAP)*, pages 926–929, April 2011.
- [39] P.-S. Kildal, E. Olsen, and J.A. Aas. Losses, sidelobes, and cross polarization caused by feed-support struts in reflector antennas: Design curves. *IEEE Trans. on Antennas and Propag.*, 36:182–190, February 1988.
- [40] Personal communication with Raynond van den Brink, ASTRON, September 2010.
- [41] CST Microwave Studio, 3D EM simulation software. URL <http://www.cst.com>.
- [42] Z. Ying, A.A. Kishk, and P.-S. Kildal. Broadband compact horn feed from prime-focus reflectors. *Electronic Letters* 6th, 31(14), July 1995.
- [43] Wolfram Mathworld-Simpson's rule. URL <http://mathworld.wolfram.com/SimpsonsRule.html>.